



MONASH University

**PORE ANALYSIS OF POROUS
CONSTRUCTION MATERIALS BY METAL
INTRUSION – EXTENDING THE LIMITS OF
WASHBURN’S EQUATION**

Chengke Ruan

Research Master

A thesis submitted for the degree of Master at
Monash University in 2019

Department of Civil Engineering,
Monash University,
Melbourne, Australia

COPYRIGHT NOTICE

© Chengke Ruan (2019).

I certify that I have made all reasonable efforts to secure copyright permissions for third-party content included in this thesis and have not knowingly added copyright content to my work without the owner's permission.

ABSTRACT

Pore analysis of construction materials has attracted extensive attention from the construction industry since pore structure influences the properties and behaviors of construction materials. The most commonly used pore analysis technique, mercury intrusion porosimetry (MIP), suffers from limitations in analyzing pores. The assumptions and principle of Washburn's equation used in MIP lead to a biased measurement of pore size and difficulties in investigating spatial information of pores and analyzing nanopores. Also, the highly toxic mercury limits its applications in the construction industry. The metal intrusion technique (MI), on the other hand, provides the possibility of addressing the limitations of MIP.

This study aims to extend the limits of Washburn's equation through a more comprehensive investigation of pore analysis derived from MI, which incorporate pore shape analysis, spatial distribution analysis of pores, and nanopore analysis. To achieve this aim, three tasks are defined: (1) investigating the noncylindrical pore shape to modify biased pore size measurement in MIP, (2) developing an analytical model to study the spatial distribution of pores, and (3) evaluating the feasibility of analyzing nanopores smaller than 3nm by MI.

Experimental, theoretical, and numerical approaches are used to accomplish these tasks. Experimental techniques such as scanning electron microscopy and MI are employed to analyze pore shape. An analytical model with supporting strength test is developed to investigate the spatial distribution of pores and its relationship with strength. Molecular dynamics simulation is conducted to study nanopore analysis by MI.

Regarding task (1), pore shape analysis by MI suggests that the cylindrical pore shape assumption used in Washburn's equation leads to biased pore size measurement. Using the area-perimeter relationship presented by a pore shape descriptor, the apparent pore shape assumption of MIP is modified to give a more accurate measurement of pore size by MIP. As an extension of pore shape analysis, studies of pore shape and microstructure transformation of construction materials are presented.

In task (2), an analytical model is developed to investigate the spatial distribution of pores, which cannot be captured by MIP. The proposed model is based on the radial distribution function (RDF) and can quantify the spatial inhomogeneity of pores in construction materials. On the basis of the proposed analytical model and supporting strength test, graphene oxide is first shown to be able to reduce the spatial inhomogeneity of pores, leading to strength enhancement of cement paste. The analytical models presented in this task provide the possibility for the development of novel and predictive structure-property relationships by machine learning.

In task (3), molecular dynamics simulation is conducted to evaluate nanopore analysis by MI and compare it with Washburn's equation. The result shows that Washburn's equation begins to deviate from simulation prediction when the nanogap is less than 3nm. An equation is proposed to predict the pressure–size relationship of metal intrusion at nanoscale, which provides the foundation for the future nanopore analysis by MI.

This Master thesis extends the limits of Washburn's equation in pore analysis and demonstrates applications of MI in the study of porous construction materials.

DECLARATION

This thesis describes my research carried out in the Department of Civil Engineering at Monash University in Australia during the candidature period from March 2017 to March 2019. The thesis is submitted to Monash University in total fulfilment of the requirements for the research Master's degree.

The thesis contains no material which has been accepted for the award of any other degree or diploma in any university or institution and no material which has been previously written or published by another person except where due reference is made in the text of the thesis.

Print Name: Chengke Ruan

March 2019

PUBLICATIONS DURING ENROLMENT

- Chen, S. J., Li, W. G., **Ruan, C. K.**, Sagoe-Crentsil, K., & Duan, W. H. "Pore shape analysis using centrifuge driven metal intrusion: Indication on porosimetry equations, hydration and packing." Construction and building materials 154 (2017): 95-104.
- Hu, Y., Li, Y. A., **Ruan, C. K.**, Lin, J. L., Chen, S. J., Tang, H. M., & Duan, W. H. (2018). "Transformation of pore structure in consolidated silty clay: New insights from quantitative pore profile analysis." Construction and building materials 186 (2018): 615-625.
- Hu, Y., Li, Y. A., Lin, J. L., **Ruan, C. K.**, Chen, S. J., Tang, H. M., & Duan, W. H (under review). "Quantification of the effect of image quality and processing on pore connectivity of silty clay through virtual 2D flow simulation."

ACKNOWLEDGEMENTS

The sequence of acknowledgements is not based on the importance of those acknowledged.

Writing this thesis has been fascinating and extremely rewarding. I would like to thank a number of people and institutions that have contributed to the final result in many different ways:

To commence with, I express my deep gratitude to my main supervisor, Professor Wenhui Duan, for his guidance and support of my research and Master study, for his constant encouragement, affectionate attitude, patience, motivation, and enthusiasm. Without his continual support, it would have not been possible for me to complete this study.

Next, I express my very profound gratitude to my parents for their spiritual support throughout my life. Without their support, I would not have been able to afford the tuition and living allowance for my undergraduate studies and the start of this Master study at Monash University. I also express gratitude to my girlfriend, Tira, for accompanying and caring about me during my writing of this thesis.

I owe my thanks to the support and guidance of my co-supervisors, Dr Kwesi Sagoe-Crentsil and Dr Shujian Chen. Also, I appreciate Associate Professor Yong Hu for his valuable advice and collaboration in this cross-disciplinary research. I would not have been able to accomplish this research project without their encouragement and constructive suggestions.

Moreover, I appreciate the assistance and collaboration as well as the valuable advice offered by my colleagues, Dr. Shujian Chen, Dr. Sherry Zhang, Dr. Ezzat Shamsaei, Dr. Tao Gu, Dr. Mingrui Du, Dr. Sheng Huang, Mr. Yanming Liu, Mr. Wei Wang, Mr. Guanzhong Xu, Mr. Xupei Yao, Mr. Felipe Basquiroto de Souza, Mr. Junlin Lin, and Ms. Jia Zie Lai.

Furthermore, I take this opportunity to express my sincere gratitude to the hard-working Monash laboratory staff for their assistance and efforts in my experiments, especially to Mr Long Kim Goh, Mr Michael Leach, Mr Zoltan Csaki, Mr Jeffrey Doddrell, and Mr Sarvan Mani in the Civil Engineering Laboratory. I am grateful to Mrs Irene Sgouras, Ms Min Major, and Ms Noi Souvandy

from the Civil Engineering Department office for their sincere assistance during my study at Monash University.

Finally, I gratefully acknowledge Monash University for providing me with Monash Graduate Scholarships and the Monash Centre for Atomically Thin Materials for providing me with the top-up scholarship that covered my living allowance. I acknowledge financial aid from the Australian Research Council and the use of facilities in the Monash Centre for Electron Microscopy.

CONTENTS

COPYRIGHT NOTICE	I
ABSTRACT	II
DECLARATION.....	IV
PUBLICATIONS DURING ENROLMENT.....	V
ACKNOWLEDGEMENTS	VI
LIST OF FIGURES	X
LIST OF TABLES	XIII
LIST OF ABBREVIATIONS AND SYMBOLS	XIV
CHAPTER 1. INTRODUCTION	1
1.1. Background	1
1.2. Research objectives	3
1.3. Thesis structure	5
CHAPTER 2. LITERATURE REVIEW.....	7
2.1. Pore structure parameters and their influence on properties	7
2.2. Commonly used pore analysis techniques	11
2.3. Research Gaps	21
CHAPTER 3. ANALYSIS OF NONCYLINDRICAL PORES AND MODIFICATION ON WASHBURN’S EQUATION.....	22
3.1. Introduction	22
3.2. Experimental program.....	23
3.3. Performance of metal intrusion technique	29
3.4. Non-cylindrical pores and its correlation with Washburn’s equation.....	35
3.5. Pore shape analysis and its link with microstructure transformation.....	41
3.6. Conclusion.....	50
CHAPTER 4. DEVIATION FROM WASHBURN’S EQUATION – SPATIAL DISTRIBUTION ANALYSIS OF PORES	52
4.1. Introduction	52
4.2. Experimental program.....	54
4.3. Radial distribution of pores in cementitious materials	58
4.4. Effect of GO on the spatial distribution of pores in cementitious materials	62
4.5. Effect of GO on the porosity of cementitious materials	68

4.6. Comparison between spatial distribution of pores and Washburn's equation	70
4.7. Conclusion.....	71
CHAPTER 5. NANOPORE ANALYSIS VIA METAL INTRUSION USING MOLECULAR DYNAMICS SIMULATION – BEYOND THE LIMITS OF WASHBURN'S EQUATION.....	73
5.1. Introduction	73
5.2. Molecular dynamics simulation of nanoporosity	74
5.3. Results and discussion – Nanopores in relation to Washburn's equation.....	77
5.4. Conclusion.....	83
CHAPTER 6. CONCLUSIONS AND RECOMMENDATIONS.....	84
6.1. Key research findings	84
6.2. Recommendation for pore analysis of construction materials by MI	86
6.3. Recommendation for future studies	86
REFERENCES.....	88

LIST OF FIGURES

Figure 1-1 Structure and contribution of the thesis	6
Figure 2-1 (a) Backscatter electron image showing representative area of a 28-day w/c 0.40 cement paste. (b) Fig. 2 (a) after undergoing binary segmentation to show the pore space pixels as black and solid material pixels as fully white [43].	8
Figure 2-2 (a) Photomicrograph of fracture surface of ceramic shows the nonhomogeneous distribution of pores, and (b) SEM images of porous titania prepared from emulsion fraction shows the ordered distribution of pores.....	9
Figure 3-1 Pore space of (a) cement paste, and (b) clay.	22
Figure 3-2 Schematic of CLMI instrumentation for sample preparation. Only one set of devices is demonstrated here; 2 or 4 sets had to be placed symmetrically on the rotor in centrifugation.	24
Figure 3-3 Schematic of apparatus used for metal intrusion	25
Figure 3-4 (a), (b) Typical BSE images of calibration samples prepared by metal intrusion and epoxy impregnation, the top right region show the images obtained by normalizing BSE intensity; (c), (d) normalized BSE intensity distribution for different phases in samples prepared by metal intrusion and epoxy impregnation; (e), (f) colored images of samples prepared by metal intrusion and epoxy impregnation based on the Gaussian distribution of phases (red-pore, green-clay/silt, yellow-sand).	30
Figure 3-5 Typical binary images of pores (black) for (a) sample W3, w/c=0.4, 10cycles, 15.2 MPa and (b) sample W5, w/c=0.8, 4cycles, 15.2 MPa.	33
Figure 3-6 Equivalent pore diameter based coloured image of metal intruded sample (C-0).....	34
Figure 3-7 Circularity (C) of pores with different sizes (equivalent diameter, d_p) for 7-day cement paste sample with $c/w = 0.4$ (C1) and 28-day cement paste sample with $w/c = 0.8$ (C2). The overall C- d_p is fitted with an inverse power function $C=0.32d_p^{-0.52}$	35
Figure 3-8 Schematic for the effect of circularity on metal intrusion into an irregular pore (a) and (b) a circular pore. F : intrusion force. R : resistant force. p : perimeter of pore. $\gamma \cos \theta$: surface tension (per unit length of pore perimeter) parallel to the direction of intrusion.	37

Figure 3-9 BSE images of metal intruded samples with $w/c=0.8$, 4 cycles and under different centrifuge pressures: (a) 0.03MPa (200 RPM) and magnification of unfilled shallow pore; (b) 0.77MPa (1100RPM) and unfilled deep pore; (c) 3.10MPa (2200 RPM); (d) 12.4MPa (4400RPM).....	39
Figure 3-10 F distribution of samples under different centrifuge speeds obtained by metal intrusion technique, Washburn's equation and modified equation [Eq. (3-9)]......	39
Figure 3-11 F distributions of samples obtained by image analysis, Washburn's equation and modified equation [Eq. (3-9)]for (a) C-0 sample and (b) C-600 sample.	41
Figure 3-12 (a) Pore volume fraction of soil samples in relation to equivalent pore diameter, (b) PSD of soil samples. The numbers in (a), indicates the corresponding total pore volume of each curve.	42
Figure 3-13 (a) Pore volume fraction of cement paste samples in relation to equivalent pore diameter; and (b) PSD of cement paste samples.	44
Figure 3-14 Figure 4 (a), (b) Typical pressure-induced transformation on Solidity of undisturbed silty clay from 0kPa (a) to 3200kPa (b). Scale bar: 50 μ m. Blue: void in pore. Red: features on the wall of a pore. (c) Solidity- d_p relationship.	45
Figure 3-15 (a) ~ (b) Change of solidity due to hydration. Black: void in pore. Yellow: features on the wall of a pore. Green: newly grown hydration products. Blue: convex hull of a pore profile. (c Average solidity of pores with different pore equivalent diameter	46
Figure 3-16 (a) Examples of fitted ellipses of pores, average aspect ratio (b) of pores with different pore diameter (d_p), and c) distribution of aspect ratio and comparison with the probability distribution of A of observed 2D cross sections for d) an oblate ellipsoid (with three radii equal to 2, 2, and 1), and e) a prolate ellipsoid (with three radii equal to 2, 0.8, and 0.8). HDM: high-density material with minimal pores (likely to be unhydrated grains and high-density C-S-H). FE: fitted ellipses.....	47
Figure 3-17 A- d_p relationship of soil samples	48
Figure 3-18 Schematics of transform process of pore structure in silty clay under increased consolidation pressure: (a) C-0; (b) C-600; (c) C-3200.....	49
Figure 4-1 Ideal forms of different patterns of $g(r)$: (a) random distribution, (b) substantial order, and (c) clustering distribution.	58
Figure 4-2 RDF of pores with the equivalent diameter of (a) 0.205 μ m, (b) 0.815 μ m, and (c) 3.246 μ m.....	59

Figure 4-3 Plot of the radial distribution of pores (GO-Cement-1day) and the fitted distribution by the proposed expression with the characteristic diameter of (a) 0.815 μm and (b) 8.155 μm	62
Figure 4-4 Transformation on RDF of pore ($d_p=0.515\mu\text{m}$) with the addition of GO	63
Figure 4-5 Relation of pore diameter and degree of clustering of pores at the curing age of (a) 1 day, (b) 7 days, and (c) 28 days.	64
Figure 4-6 Mean degree of clustering of pores with the pore diameter range of (a) 0.1 μm - 1 μm , and (b) 1 μm - 10 μm	65
Figure 4-7 (a) Compressive strength and (b) tensile strength of plain cement and GO/cement composites....	66
Figure 4-8 Relation between normalized δ and normalized tensile strength (derived from data presented by Yu. et al. [232]).....	67
Figure 4-9 PSD for GO-Cement sample cured for (a) 1 day, (b) 7 days, and (c) 28 days.	69
Figure 5-1 (a) Snapshot of the box for intrusion simulation, (b) lattice used for Morse potential parameter calculation of Hg-Hg interaction, (c) system used for Morse potential parameter calculation of Hg-C interaction.	75
Figure 5-2 Relationship between energy and lattice dimension for: (a) Hg-Hg interaction, (b) Hg-C interaction.	77
Figure 5-3 Snapshot of metal intrusion at the pressure of: (a) 513.5 MPa, (b) 1776.7 MPa, (c) 6765.8 MPa and (d) Pressure higher than 6765.8 MPa.	79
Figure 5-4 Comparison of simulation and Washburn's equation.....	81

LIST OF TABLES

Table 2-1 Summary of commonly used pore analysis techniques	18
Table 2-2 Summary of limitations of the MIP and Washburn's equation	20
Table 3-1 Properties of low-melting-point metals used in this study	24
Table 3-2 Sample information of soil samples	27
Table 3-3 Volume fraction of phases obtained by Gaussian fitting	32
Table 3-4 Fitted parameters for C-0 and C-600 samples	40
Table 4-1 Elemental analysis of GO	54
Table 4-2 Mix design	55
Table 4-3 Porosity calculated from Gaussian fitting	57
Table 4-4 Parameters of the RDF equation of pores for GO-Cement (1 day) determined by nonlinear least square fitting	61
Table 4-5 Effect of GO on porosity in terms of curing age	68
Table 5-1 Morse potential parameters	78
Table 5-2 Relationship between pressure and intrusion size	79

LIST OF ABBREVIATIONS AND SYMBOLS

A	Aspect ratio
a	Reciprocal distance
BSE	Backscattered electron
C	Circularity
CLMI	Centrifugation-based low-melting-point metal intrusion
D	Intruded gap width
D_0	Dimensions of energy
d_p	Equivalent pore diameter
GO	Graphene oxide
MD	Molecular dynamics
MI	Mercury intrusion
MIP	Mercury intrusion porosimetry
P	Pressure
PSD	Pore size distribution
R_0	Equilibrium bond distance of the two atoms
RDF	Radial distribution function
rpm	Revolutions per minute
S	Solidity
w/c	Water to cement ratio
δ	Degree of clustering
ρ	Density
ω	Angular velocity
γ	Surface tension
θ	Contact angle

CHAPTER 1. INTRODUCTION

1.1. Background

Porous construction materials have received considerable attention in recent years because of their specific physical properties and unique functional properties, such as high strength–density ratio [1], absorption of impact energy [2], and flame [3] and heat resistance [4]. Pore structure is the key components of porous construction and can significantly influence their engineering properties [5, 6] and functionality [7-9].

One of the most important challenges in the construction industry, and an area of considerable research activity, is understanding the pore structure of porous construction materials and how it affects the properties and behaviors of porous construction materials. Various pore analysis techniques have been developed and used in the pore structure study of porous construction materials. Among all these techniques, MIP is the most widely used in the construction industry, due to its ability to measure pores over a wide size range in a comparatively easy and quick test [10]. However, the principle and assumptions of Washburn's equation used in MIP limit its performance in providing reliable pore size measurement and comprehensive pore structure information, including the spatial distribution of pores and information about nanopores. Moreover, extreme care and safety protocols are needed for MIP due to the high toxicity of mercury. The metal intrusion technique (MI), which is a pore analysis technique based on direct measurement, provides the possibility of addressing these limitations.

The purpose of this study is to extend the limits of Washburn's equation in pore analysis by MI. Pore analysis methods associated with MI are developed to address the limitations of Washburn's equation from three aspects: correction of the biased pore size measurement of MIP through correlating the noncylindrical pore shape with Washburn's equation; supplementation of MIP in analysis of the spatial distribution of pores; and extension of the limit of MIP in nanopore analysis

using metal intrusion.

Investigation of pores using MI dates to 1996 [11] and has shown great capacity and potential in pore analysis. MI incorporating microscopy enables the direct observation of pores in construction materials over a wide size range of pores, which cannot be achieved by traditional indirect techniques such as MIP. On the other hand, research using MI has focused mainly on the qualitative analysis of pore structure or discerning the pore size [12, 13], which suggests that there is a need to improve the analytical methods associated with this technique to enhance its pore analysis capacity. Also, the safety issue resulting from the use of toxic Wood's metal [12, 14-16] in past works needs to be addressed.

The direct measurement of pores by MI enables the analysis of pore shape, which cannot be achieved by MIP [17, 18]. Pore shape can exert an influence on the permeability of construction materials via its direct correlation with the hydraulic radius [19]. The identification of pore shape information by MI and study of its correlation with the biased pore shape assumption [20] in Washburn's equation is research work worth developing.

The indirect measurement of MIP makes it impossible to analyze the spatial distribution of pores in construction materials. Pores in construction materials are rarely uniformly distributed [21, 22], which can create fatigue issues and significantly restrict strength via stress concentration [23]. Materials with the same total porosity and pore size can exhibit entirely different properties, depending on whether the spatial distribution of pores is homogeneous or not. Analyzing the spatial distribution of pores is important for understanding the nature of porous construction materials and for the development of the materials with improved performance.

The potential of analyzing nanopores is beneficial to the study of shrinkage and creep in construction materials from the fundamental perspective [24, 25]. However, Washburn's equation cannot detect nanopores because its capillary flow model [26] is not applicable to describe the movement of substance at the nanoscale. Once a non-wetting metal is intruded into nanopores by extremely high pressure, it is possible to detect and study nanopores by MI. However, understanding

of the performance of metal intrusion in nanopore analysis is still limited by insufficient data.

In this study, the pore analysis methods associated with MI are investigated by the development of analytical models, numerical simulation, and experimentation. Non-toxic Field's metal [27] is first used in MI as a substitute for the toxic Wood's metal used in past work.

Based on the clear pore shape information obtained by MI, the cylindrical pore assumption used in Washburn's equation is modified to provide more accurate measurement of pore size distribution by MIP. An analytical model, acting as a supplementary pore analysis to MIP, is developed to analyze the spatial distribution of pores in cement paste. The results show good correlation between the spatial inhomogeneity of pores and the strength of cement paste, thereby indicating the effectiveness of the proposed model in analyzing the spatial information of pores. MD simulation of metal intrusion at the nanoscale is conducted to evaluate the feasibility of using metal intrusion to analyze nanopores, exceeding the limits of Washburn's equation in nanopore analysis. The result indicates that Washburn's equation at the nanoscale begins to deviate from simulation predictions. An equation is used to predict the pressure of metal intrusion at the nanoscale to support future nanopore analysis by MI. The pore analysis method and comprehensive pore information presented in this thesis can be used to develop novel and predictive structure-property relationships by machine learning.

1.2. Research objectives

This study focuses on developing analytical methods associated with MI to address some of the limitations of Washburn's equation, allowing more comprehensive pore analysis from the perspective of pore shape and the spatial distribution of pores. A study of metal intrusion at the nanoscale is also conducted to provide a foundation for future nanopore analysis by MI, which exceeds the detectable pore size limit of Washburn's equation.

This research can be divided into three objectives: (1) investigating the pore shape and modifying the biased pore size measurement of Washburn's equation due to the cylindrical assumption; (2) developing an analytical model to analyze the spatial distribution of pores in porous construction

materials; (3) evaluating the nanopore analysis by MI and its difference from Washburn's equation.

(1) Investigating the pore shape and modifying biased pore size measurement of MIP due to the cylindrical assumption

Washburn's equation models the pores as cylinders, which grossly departs from the reality of pore shapes in construction materials. Past studies have pointed out that the use of a noncylindrical pore shape in pore shape assumption can shift the pore size distribution (PSD) measured by MIP [28-30]. Investigating true pore shapes and using that information to correct the biased cylindrical pore shape assumption of Washburn's equation is the main research focus of this task.

(2) Developing an analytical model to analyze the spatial distribution of pores in porous construction materials.

In addition to the strong correlation between porosity and material properties, the spatial distribution of pores is also a critical factor that influences the properties and behaviors of porous construction materials such as rock and concrete [31]. However, the commonly used MIP method cannot detect the spatial distribution of pores due to its indirect measurement. To address this gap, an analytical model is needed to investigate the spatial information of pores and its correlation with the mechanical properties of materials.

(3) Evaluating the nanopore analysis by MI and its difference from Washburn's equation.

The use of Washburn's equation in pore analysis is based on fluid dynamics, which is not applicable for analyzing nanopores. To verify the feasibility of using MI to analyze nanopores by direct observation, numerical simulation is needed to study the metal intrusion behavior at the nanoscale structure. By predicting the pressure-pore size relationship of metal intrusion in the nanopores, this study can provide the foundation for future nanopore characterization by MI.

1.3. Thesis structure

The thesis is organized into six chapters, three of which are the main chapters with the major contributions, as shown in Figure 1-1. Chapters 1, 2, and 6 present the introduction, literature review, and the conclusions and recommendations, respectively. The present chapter introduces the background, objectives, and structure of the thesis. The contents of Chapters 2 to 6 are listed below.

Chapter 2, the literature review, covers the following fields:

- Pore structure parameters and their links with material properties
- Commonly used pore analysis techniques for porous construction materials

The review provides a broad picture of the research and engineering concerns related to pore structure information and commonly used pore analysis techniques. Specific attention is paid to the limitations of Washburn's equation used in MIP. Research gaps are identified based on the review.

Chapter 3 focuses on the analysis of noncylindrical pore shape and its correlation with pore shape assumption in MIP. The chapter is organized based on published papers [32, 33]. In this chapter, the MI is proved to cause minimal alteration of the pore structure of samples while providing clear pore profile images. Washburn's equation is modified on the basis of the area-perimeter relationship presented by pore shape to give a more accurate measurement of pore size by MIP. Pore shape from 2D observation and pore shape in 3D space are correlated using probability theory. Also, two shape descriptors and PSD are used to study the microstructure transformation in cement hydration and consolidation of soil.

Chapter 4 presents an analytical model with supporting experiments to study the spatial distribution of pores in porous construction materials, which act as a supplement to MIP. The spatial distribution of pores in cement paste is characterized using a proposed expression of the RDF. A descriptor called 'degree of clustering' is defined to quantify the spatial inhomogeneity of pores. Moreover, by using the proposed analytical model, graphene oxide (GO) is first shown to be able to homogenize the spatial distribution of pores in cement paste, thereby improving its strength.

In Chapter 5, the process of intrusion of a non-wetting liquid into a nanogap structure is studied using molecular dynamics simulation to investigate the feasibility of using metal intrusion to analyze nanopores. The result indicates that the pressure–size relationship predicted by the simulation begins to deviate from Washburn’s equation. A modified equation is presented to predict the pressure–size relationship in the nanopore analysis of metal intrusion. The numerical study presented here can be used as a starting point for future nanopore analysis by MI.

Chapter 6 presents the summary of the studies in the thesis. It also recommends some analytical models and methods based on MI to provide enhanced pore analysis compared with MIP. Possible topics for future study are also suggested.

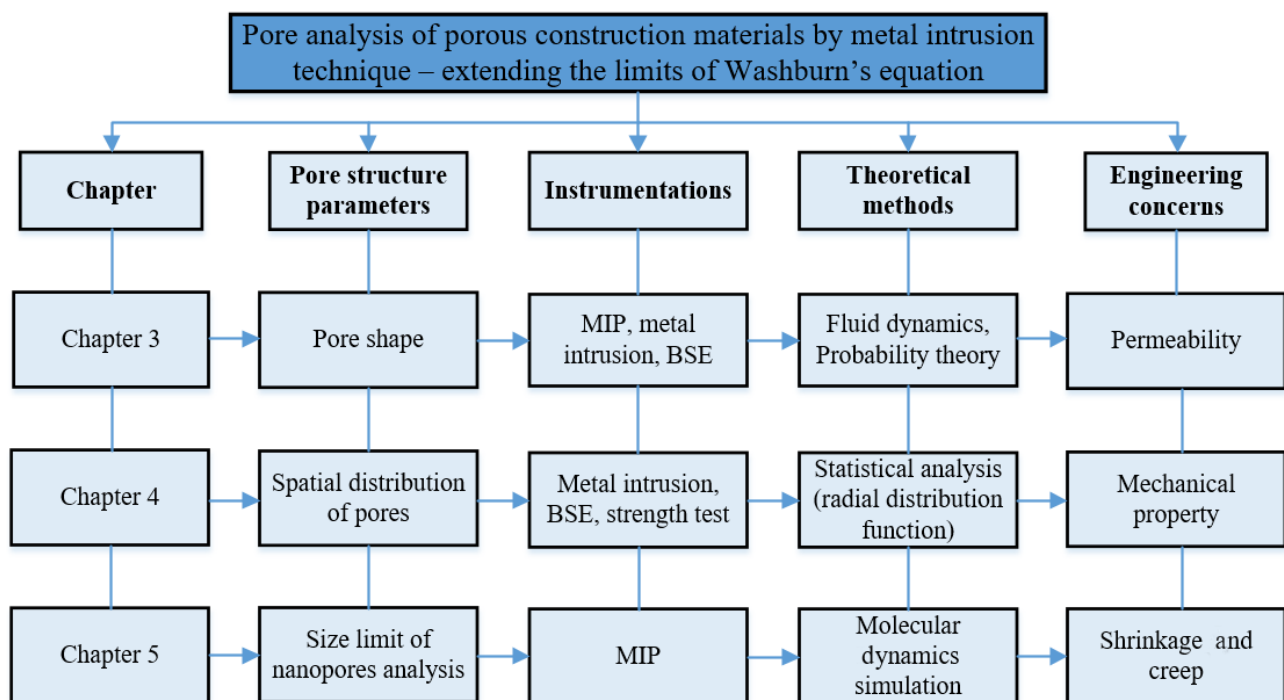


Figure 1-1 Structure and contribution of the thesis

CHAPTER 2. LITERATURE REVIEW

2.1. Pore structure parameters and their influence on properties

Porous construction material is composed of a rigid solid matrix and a pore network. Pore structure parameters such as PSD are the key components of porous construction materials. These pore structure parameters can affect the engineering properties and behaviors of construction materials such as strength [34], permeability [35], and long-term behaviors [36]. Characterization and analysis of pore structure parameters such as total porosity, PSD, pore shape, and spatial distribution of pores is important to the study of porous construction materials [35, 37-39].

To reliably describe the properties and performance of porous construction materials, more than one pore structure parameter needs to be determined. Even a detailed description of a single pore structure parameter is unlikely to be sufficient to predict the properties and performance of such materials [10]. For example, total porosity is the main parameter required to determine the mechanical properties of a construction material, but the total porosity, pore connectivity, and PSD are needed to determine the permeability of construction materials [35]

In general, it is necessary to characterize and analyze most of these pore structure parameters to study the properties of porous construction materials [40]. From this viewpoint, two key pore structure parameters are necessary for a comprehensive description of pore structure: (1) pore shape and (2) spatial distribution of pores.

Pore shape describes the geometrical characteristics of the cross-section of a pore. The cylindrical shape is most commonly assumed in the absence of specific knowledge of pore shape, and has been used in many traditional pore analysis techniques such as MIP [41] and gas adsorption [42]. However, the shape of pores in most porous construction materials is rarely cylindrical. For example, experimental observation of pore shapes in hydrated cement and rock shows that the shapes are irregular and quite different from the perfect circle [43-45]. The study presented by Diamond [43] had shown that the pore shapes in hydrated cements are quite different from cylindrical pores assumed

by the Washburn equation model, as shown in Figure 2-1 [43].

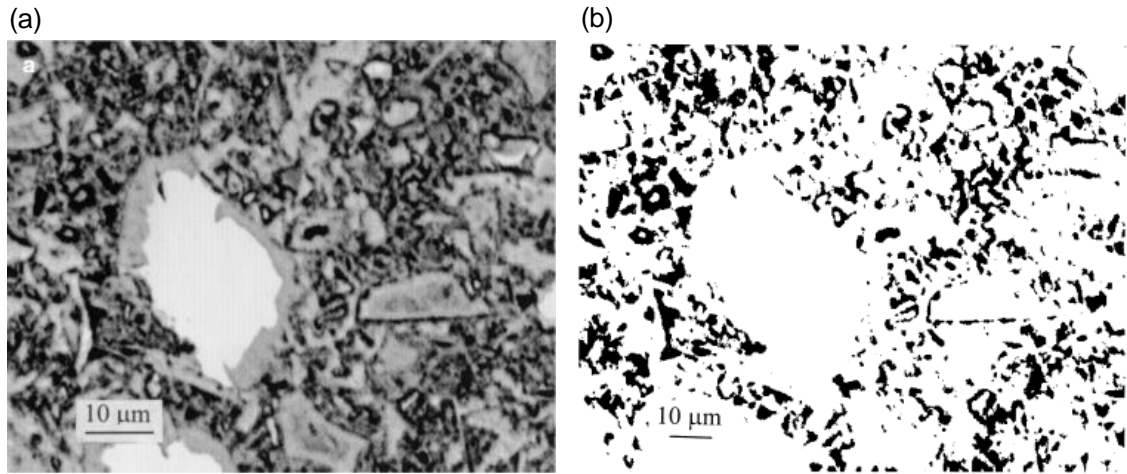


Figure 2-1 (a) Backscatter electron image showing representative area of a 28-day w/c 0.40 cement paste. (b) Fig. 2 (a) after undergoing binary segmentation to show the pore space pixels as black and solid material pixels as fully white [43].

Pore shape can influence the properties and behaviors of porous construction materials. An early experimental study by Brace demonstrated the influence of pore shape on the permeability of rock [46]. Stress concentrations of pores with various shapes have been extensively studied [47, 48]. In addition, pore shape is an important factor influencing the interpretation of traditional pore analysis techniques and their test results [43].

The pore shape descriptor is a parameter inherent in the assumed model in pore analysis technique rather than a parameter determined during experiment [10]. The biased pore shape assumption in traditional pore analysis techniques can lead to errors in pore measurement. Past studies have qualitatively proposed limitation of the cylindrical pore assumption in MIP [43, 49], but the link between the pore shape and the pore size measurement by MIP has not been addressed. To address the problem, pore shape descriptors can be used to account for noncylindrical pores.

Spatial distribution of pores describes the arrangement of pores in the 3D-space of materials [50]. The spatial distribution of pores is essential to the properties of materials because it describes the overall heterogeneity of pore structure in materials. It is known that materials with the same total porosity and PSD but different spatial pore distributions would have different properties [51]. The

spatial distribution of pores in materials can be categorized into three forms: ordered distribution [52], uniform distribution [53], and nonhomogeneous distribution [54]. Figure show the nonhomogeneous distribution [55] and ordered distribution [56] of pores in different materials.

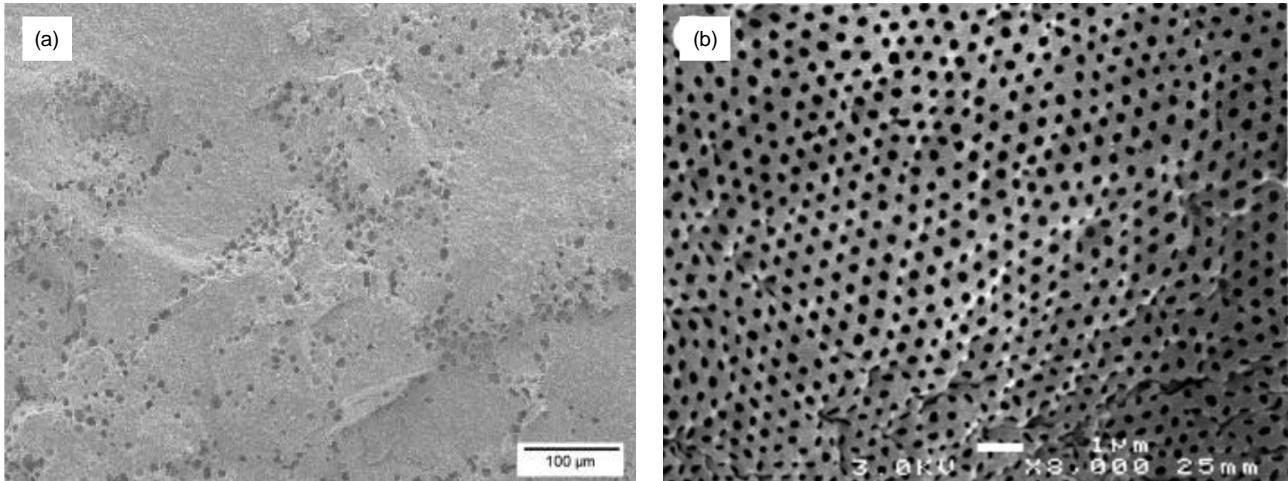


Figure 2-2 (a) Photomicrograph of fracture surface of ceramic shows the nonhomogeneous distribution of pores, and (b) SEM images of porous titania prepared from emulsion fraction shows the ordered distribution of pores.

Ordered distribution and uniform distribution of pores can be observed in syntactic materials through templating [56], 3D printing [57], and proper treatments [58]. However, the spatial distribution of pores in most porous construction materials is nonhomogeneous [21, 55, 59-62]. The presence of spatial inhomogeneity of pores or pore clustering can significantly influence the engineering properties of porous construction materials [63, 64]. Pore clustering, which is the nonhomogeneous distribution of pores with high spatial density in a local region, reduces the loadbearing area of solid material, leading to a reduction in both Young's modulus and strength [55]. Pore clustering acts as a stress concentration site for the initiation of fatigue cracks in construction materials [65, 66]. Spatial inhomogeneity of pores can also affect the hydraulic conductivity of porous construction materials [21]. In most cases, superior engineering properties can be achieved if the spatial distribution of pores in the materials used becomes more homogeneous. Proper analysis of the spatial distribution of pores is essential to the study of porous construction materials and the optimization of material properties.

Despite recognition of this problem, few studies have reported on the development of quantitative description of the complex spatial distribution of pores in porous construction materials. To author's best knowledge, the fractal dimension is the only parameter used to describe the overall complexity of pore structure in porous materials, but that is still far from description of the spatial distribution of pores. Fractal dimension, which characterizes multiscale and self-similar geometric structure within materials [64], has been used to describe the pore phase of porous materials [67-69]. However, the fractal theory is only applicable to homogeneous porosity [70].

Current pore analysis methods for describing the spatial distribution of pores are still far from a quantitative description. A considerable amount of future research is still required to describe the spatial distribution of pores in porous construction materials with a wide size range.

In addition to the pore structure parameters, the analysis of pores with wide size ranges is also important to the pore structure study of porous construction materials. Pore size is usually defined as the diameter of a cylindrical pore or the distance between the side of a slit-shaped pore. Typical pore size ranges in porous construction materials can vary over several orders of magnitude [10]. Pores of different size can exert different influences on the properties of porous construction materials. For example, macropores (>50 nm) [71] are essential to the permeability of materials, whereas micropores (<2 nm) [71] do not contribute much to permeability because their small size is only about one order of magnitude greater than the water molecule [72]. On the other hand, micropores mainly affect the shrinkage [73, 74] and creep [75] of porous construction materials.

A wide variety of techniques has been used to analyze the pore structure of porous construction materials. Each of the available techniques is most suitable for a specific pore size range. The commonly used techniques can analysis pore size down to 2 nm [76], but analysis of micropores of a smaller size is still limited, especially by direct measurement. Micropores are the basic structural component in some porous construction materials, an example being gel pores [77] in cementitious materials with sizes down to 0.5 nm. The capability of characterizing micropores provides the

possibility of understanding and optimizing the engineering performance of porous construction materials from a fundamental level [78]. Therefore, there is a need to develop a proper pore analysis technique to decrease the minimum detectable pore size.

2.2. Commonly used pore analysis techniques

As the understanding that pores have a direct effect on properties became well known, researchers began to develop methods to characterize the pore structure of porous construction materials. This section provides a comprehensive literature review of commonly used pore analysis techniques and their capabilities and limitations.

The techniques used to experimentally measure the pore structure information in porous construction materials can be categorized into direct and indirect methods [79]. Direct methods, such as the MI, produce a direct physical image of the pore structure examined, revealing the size, shape, and spatial arrangement of the pores. In indirect methods such as MIP, an external stimulus is applied to a material and the material's response is measured using a detector. The pore structure parameters are determined indirectly from properties such as the intrusion volume of mercury. The direct method is preferable [80] because the pore structure is directly observed without any arbitrary hypothesis.

2.2.1. MERCURY INTRUSION POROSIMETRY

Mercury intrusion porosimetry has proven over decades to be a useful method for analyzing the pores of porous materials. In MIP, pressure is applied to non-wetting mercury in order to force the mercury into the empty pores of porous materials [81]. MIP obtains the pore structure information using the Washburn's equation, which is a well-known equation of fluid dynamics presents the inverse proportional relationship between the intruded pore diameter and the pressure, by assuming that the pore is cylindrical [82].

MIP has become the most widely used technique to study the pore structure of porous

construction materials [83]. This technique has been developed and improved to the extent that it is now possible to determine a wide variety of pore parameters [84-86] such as total pore volume, PSD, and specific surface area of pores. MIP can typically measure a pore size range with several orders of magnitude in a single test, typically from tens of micrometers to 3.6 nm, corresponding to the maximum pressure of 400 MPa, which cannot be achieved by any other technique [51]. The method is comparatively easy and quickly performed.

Despite the widespread application of MIP in characterizing porous materials, the accuracy and reliability of pore information data thus obtained may be biased and is questionable. The main limitation of MIP is that the PSD is biased due to the “ink-bottle” effect [43, 49]. One of the assumptions of MIP is that all pores are connected to the sample surface directly or through larger pores. However, the high complexity and heterogeneity of pore features in most porous materials result in pores that do not meet this assumption [87], known as “ink-bottle pores”. The intrusion of mercury into the wide inner body of ink-bottle pores does not occur until the pressure corresponding to the threshold diameter of narrow pores is reached. As a consequence, part of the volume of large pores in porous materials is assigned to a size smaller than that of the threshold diameter, regardless of their actual size, leading to a biased interpretation of the PSD [43]. Due to the ink-bottle effect, no indication of large pores in materials is presented in many published MIP results [43], and pore sizes greater than 100 μm in diameter detected by MIP are rarely reported in the literature [88-90]. These large pores, present in construction materials such as concrete, soil, and rock, form a substantial portion of the total pore volume, which may connect to the specimen’s surface by small pores at the surface of materials. These large pores are not intruded until the threshold pressure is reached in MIPs, and they are recorded as fine pores [18]. Thus, MIP results will always show smaller pore sizes than observed with microscopy or microCT.

The shapes of pores are misrepresented by the cylindrical pore assumption. The Washburn equation was derived based on the assumption that the cross-section of intruded pores is cylindrical

[91], which is far from the irregular shape of the pores in most porous materials. The pore shape information is related to the properties of the materials [46, 92-94].

Selection of an appropriate contact angle in MIP may also cause deviation in the results [10]. An error of 1° in the contact angle assumption in MIP can lead to an error of 2% in pore size detection. The contact angle depends on several parameters including the composition of the specimen [95], pore size [96], drying techniques [97], surface roughness [98], and the purity of mercury [99]. These effects can scarcely be considered and controlled in the MIP test, all of which can cause a biased interpretation of results such as the PSD. MIP also requires extreme care and safety protocols during experiments because mercury is a highly toxic substance that can be absorbed through the skin and mucous membranes [100].

2.2.2. GAS ADSORPTION

Physical gas adsorption is extensively used in the determination of micro- and mesoporous materials. This technique accurately determines the number of gas molecules adsorbed on solid materials, which is a measurement for pore structure. Adsorption isotherm measurements provide information about surface area, pore volume, and PSD [101-103]. Gas adsorption allows the detection of pore size distributed over a narrow range (the detectable pore diameter is usually limited from 2 nm to about 100 nm [42]). Of all the frequently used adsorptives including Ar, H₂O, and CO₂, N₂ has remained universally pre-eminent since N₂ adsorption at 77 K and sub-atmospheric pressure can be used for routine quality control and investigation of new materials.

Physical gas adsorption is a method that involves determination of the amount of gas adsorbed at different relative pressures, before and after adsorption in an adsorption isotherm. To obtain the specific surface area of porous materials, a simplified model of physisorption based on Brunauer–Emmett–Teller theory, is applied to describe the adsorption process [101]. It is assumed that the completed monolayer gas molecules on the solid surface are in a close-packed state, with no lateral interactions between the adsorbed molecules. The molecules in the first layer act as sites for the

molecules of the second layer; these molecules, in turn, are sites for molecules in the higher layers. The PSD model in gas adsorption is developed based on the Kelvin equation [104] and correlated for multilayer thickness on the pore wall.

Due to the artificial nature of the BET theory, the range of applicability of the BET equation is always limited to a part of the gas isotherm, where the linear relationship of the BET equation is maintained only in the range of $0 < P/P_0 < 0.35$ [105]. Therefore, the maximum diameter of pores detectable by the gas adsorption technique is limited to around 100 nm. The narrow range of pore size detectable by gas adsorption makes it insufficient for obtaining the pore structure information of porous materials in which the pore sizes are distributed over a wide range, such as concrete [51], soil [106], and rock [39]. Hence, gas adsorption is usually used in combination with other pore analysis techniques to study porous materials [107, 108]. Also, the nature of BET theory makes it impossible to detect the spatial distribution of pores.

Although gas adsorption techniques and the analysis of adsorption data appear to be well established, the accuracy and reliability of evaluation of these data and information is still a problem. This is mostly attributed to the inherent strong surface heterogeneity and structural heterogeneity of many porous materials. Most of the models in data analysis developed so far are based on ideal cylindrical pore geometry [109], which is different from the actual shape of pores. On the other hand, the effects of structural and surface heterogeneity on the adsorption properties of porous materials are often difficult to distinguish, which makes it difficult to develop theoretical models of gas adsorption in heterogeneous porous media and to apply the methods for characterization of porous solids [110, 111].

2.2.3. MICROCT

MicroCT is an imaging technique that provides the 3-dimensional internal structure of porous materials [112, 113]. MicroCT relies on measurement of the attenuation of X-rays passing through a

specimen. By applying appropriate reconstruction algorithms, a number of different angular projection images produced by the rotational movement of specimens relative to the X-ray source and detector are used to visualize 3-D pore networks of porous materials. Extensive research using MicroCT has been undertaken to study the complex porosity and pore geometry of concrete [114], soil [115], rock [116], wood [117], and other porous construction materials.

MicroCT is a preferred candidate for pore analysis of porous media because there is no need to use any arbitrary hypotheses in pore profiling or data that is essential for other techniques (e.g. MIP) [114]. MicroCT can produce information about the physical features and spatial arrangement of pores that cannot be obtained from MIP and gas adsorption. Another advantage of MicroCT is its ability to perform pore structure determination of specimens in a non-destructive way, making it possible to study the pore structure of specimens without introducing substantial disturbances [118], such as the compression of highly porous samples [41] and the influence of drying [119] in MIP. This advantage allows monitoring of the time-dependent evolution of the internal structure of materials [115, 120, 121].

In practice, this 3D structure characterization technique is an excellent tool for visual inspection and quantitative analysis. It is essential, however, that the limitations of microCT should be considered when characterizing pore structure. The main limitation of MicroCT is its low spatial resolution [122]. Spatial resolution describes the level at which details in an image can be resolved. A small cross-section of a sample will absorb fewer photons and therefore will require a longer exposure time to assure acceptable counting statistics. Increasing the spatial resolution for detecting the features of a small sample requires larger incident photon intensity or longer integration time. Due to the technical limitation of fabricating radiation sources with high photon flux and high energy [122], the ability to examine small features in samples is limited to approximately 1 μ m [115, 123]. The limited detectable spatial resolution of MicroCT makes it impossible to characterize the large number of nanopores existing in many porous materials, such as nanopores in clay and concrete.

Another critical limitation of MicroCT is the contradictory feature regarding voxel size (the size of the volume elements in a 3D matrix of reconstructed samples) and sample size [115]. In the rotational movements of the imaged samples, the reconstructed voxel size is controlled by the source-to-detector distance, the source-to-sample distance, and the distance between the center of two neighbouring pixels [124]. Due to technological and computational reasons, the number of detector pixels is usually limited to several thousands of pixels, a feature that limits the detectable voxel size as a function of the sample size [115]. This limitation can result in limited detectable pore features and a narrow detectable pore size that may not allow capture of the entire pore structure information of samples. For example, the analysis of micropores in coarser rock samples by MicroCT will miss large pores and may not produce representative pore structure information due to the larger-scale heterogeneity of samples [116, 125].

2.2.4. METAL INTRUSION TECHNIQUE

Metal intrusion technique is a branch of image analysis techniques that can analyze pores through direct observation using an electron microscope. MI involves the intrusion [12] of a non-wetting metal at high pressure into interconnected pores of samples. The imaging process is performed on the flat cross-section [126] of samples that is commonly obtained by grinding and polishing. The thresholding method [127] is then applied to the cross-section images of the samples to separate the pores and the solid matrix of samples. Due to the enhanced difference of the backscattered electron intensity between pore space filled with metal and the solid matrix of porous materials in backscattered electron (BSE) imaging, the pore images obtained by MI are much clearer than those obtained from traditional polymer impregnation [128]. This enhancement in the imaging process is beneficial to pore profile detection and analysis.

The MI technique can produce detailed pore structure information including porosity [129], PSD [130], specific surface area [131], and fractal dimension of pores [67, 132]. Direct observation of

pores also provides the potential to measure the spatial distribution of pores [131, 133] by this technique. MI is a preferred method because it is one of the most direct ways to analyze complex pore features and porosity [134]. It can also detect pores in materials over a wide range of sizes, from tens of nanometers [14] to millimeter scale [11].

Despite the considerable capacity of MI for pore analysis, its limitation in presenting the 3D pore structure is well recognized [135]. An experimental study by Kurumisawaa et al. [136] presented the possibility of using stacking of 2D pore images to achieve 3D reconstruction of pore structure by MI. Other extensive studies involving image-based 3D modeling have demonstrated the possibility of presenting 3D pore structure based on the 2D observation of pores [137, 138] by MI. On the other hand, past work using MI has mainly used toxic Wood's metal [14, 15, 139, 140] as intrusion material, leading to safety concerns in experimentation.

2.2.5. SUMMARY OF TECHNIQUES FOR PORE ANALYSIS

A summary of commonly used pore analysis techniques is given in Table 2-1.

Table 2-1 Summary of commonly used pore analysis techniques

Technique	Detection limits	Capacity	Limitations
MIP	3.6 nm-100 μm	Indirect method Porosity, PSD, specific surface area.	Biased PSD measurement [43, 49].and inability to present large pores [18, 43]. (>100 μm) due to 'ink-bottle' effect Toxicity of mercury [141] Accuracy influenced by contact angle [10].
Gas Adsorption	2 nm-100 nm	Indirect method Porosity, PSD, specific surface area.	Narrow detectable pore size range [142] Alteration of PSD and porosity due to altering the surface of the sample [143].
MicroCT	>1 μm	Direct method Porosity, PSD, specific surface area, spatial information.	Limited resolution (~1 μm) [115, 123] Difficulty in presenting features of the sample due to contradictory voxel size and sample size [115, 144, 145]
MI	Down to nanometer level (>10 nm in reported studies)	Direct method Porosity, PSD, specific surface area, spatial information.	Toxicity of intrusion metal in past work [13, 16, 146] Limited pore structure information from 2D observation (compared with MicroCT) [135]

Based on the review and the summary in Table 2-1, the comparative advantages and limitations of commonly used pore analysis techniques were studied. Of all the techniques described, MIP is the most widely used method in pore analysis of porous construction materials [147, 148]. Although the appropriateness of MIP for pore analysis has been questioned by researchers [43, 149-151], the MIP will continue to be used in the construction industry in the foreseeable future [152]. This is because MIP is experimentally faster, conceptually simple, and can analyze a much wider pore size range than other techniques currently used in practice [10].

Despite the broad application of MIP in the construction industry and material science, some of the issues result from the principle and assumptions of MIP that impose restrictions on the method. Washburn's equation models the pores as cylinders [153], an assumption that departs grossly from

the reality of the pore system in porous construction materials [154]. The biased pore shape information from MIP can affect permeability study [46] of construction materials. The effect of considering noncylindrical pore shapes rather than assuming cylindrical pores tends to shift the PSD measured by MIP. This effect has been pointed out by several researchers [28-30]. However, the problem has not been addressed on the basis of pore shapes directly observed in construction materials.

On the other hand, the pore analysis of MIP is performed based on indirect measurement [155]. On the basis of Washburn's equation, which presents the relationship between intruded pore and pressure, the PSD is calculated via determining the intrusion volume of mercury at different pressures [156]. This procedure does not capture the detailed spatial arrangement of individual pores [157, 158]. Therefore, MIP cannot be used to analyze important spatial information of pores, which is highly correlated with the mechanical properties of construction materials.

Furthermore, the fluid dynamics model of Washburn's equation, which describes the capillary flow [26] of mercury in the pore system, is inapplicable for the study of nanopores. Despite the fact that a theoretically minimum pore size of 3.6 nm [159] can be measured by MIP, its performance in analyzing nanopores is questionable. Comparison studies between MIP and gas adsorption have shown that MIP is not reliable for measuring porosity around 5 nm [160, 161]. The reason that MIP is inapplicable for nanopore analysis is that the movement of mercury atoms in the nanopores is dominating by diffusion [162, 163] rather than capillary flow. This restricts the application of MIP to the study of nanopores that influence the shrinkage and creep behavior of construction materials. The limitations of MIP resulting from its principles and assumption is summarized in Table 2-2.

Table 2-2 Summary of limitations of the MIP and Washburn's equation

Assumption or principle of MIP	Limitation in pore analysis	Related material properties and performance
Cylindrical pore shape assumption	Lacks pore shape information [41], biased PSD [28-30]	Permeability
Indirect measurement of pores based on Washburn's equation	Does not provide spatial information of pores [157, 158]	Strength
Capillary flow described by Washburn's equation at the nanoscale	Inapplicable for nanopore analysis [161, 162]	Shrinkage and creep

These inappropriate principles and assumptions restrict the application of MIP in pore analysis of porous construction materials. MI, on the other hand, provides the possibility of solving these limitations. In combination with an electron microscope, MI can directly observe pores in physical space over a wide size range. All other commonly used techniques entail some issues that are critical in address these limitations, such as the indirect measurement of gas adsorption and the low resolution of MicroCT. To address the limitations of MIP presented in this section, this study aims to (i) modify the theoretical model of the MIP, and (ii) develop and evaluate analytical models for MI.

2.3. Research Gaps

From the literature review in this section, the following research gaps have been identified:

1. The inappropriate cylindrical pore shape assumption of Washburn's equation leads to the biased pore size analysis of MIP.
2. The indirect method based on Washburn's equation cannot capture the spatial distribution of pores.
3. The feasibility of using a MI to analyze nanopores, which cannot be measured using Washburn's equation, is still unclear.
4. The ink-bottle effect due to the pore structure of materials leads to the biased measurement of pore size distribution in MIP.
5. The constant contact angle used in MIP may produce significant distortions in pore size distribution.

The research gaps 1, 2, and 3 are addressed in the following chapters.

CHAPTER 3. ANALYSIS OF NONCYLINDRICAL PORES AND MODIFICATION ON WASHBURN'S EQUATION

3.1. Introduction

The pore structure provides essential information for studying the properties and behaviour of porous construction materials. Pore structure parameters such as porosity, PSD and pore shape can exert their influences on the properties of porous construction materials. Among all these pore structure parameters, the study of pore shape is rarely observed. Pore shape describes the geometry characteristic of the cross-section of pores, the permeability of porous construction materials is highly correlated with the pore shape [164] since the hydraulic radius [165, 166] in the capillary flow is directly linked with the pore shape.

Due to the absence of specific knowledge of pore shape, cylindrical pore shape assumption has been used in many traditional pore analysis techniques such as the Washburn's equation of mercury MIP [167]. However, the pore shape in most porous construction materials is rarely cylindrical. For example, the pore shapes observed in concrete and soil are irregular and quite different from cylindrical shape [168, 169], as shown in Figure 3-1 (a) [170], and (b) [171], respectively.

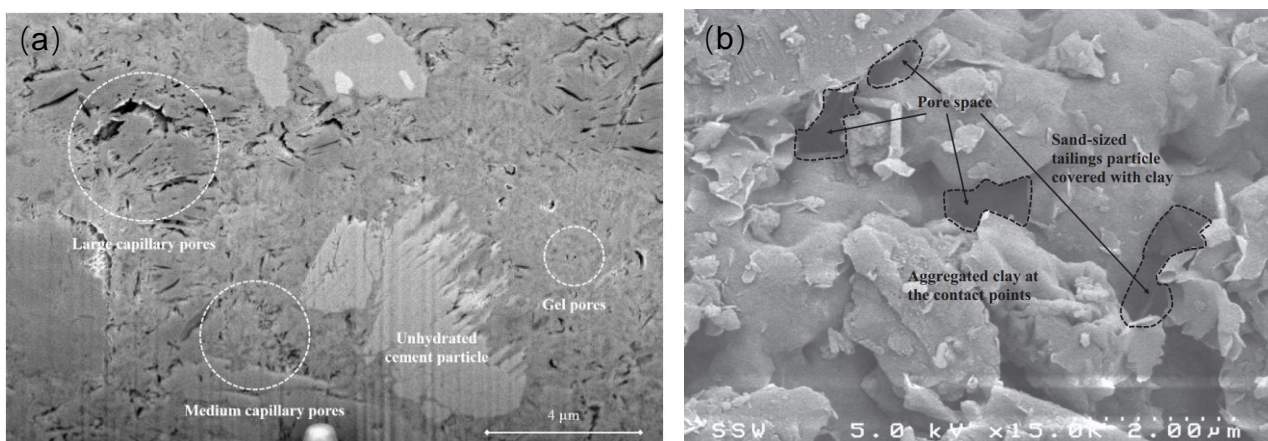


Figure 3-1 Pore shape of (a) cement paste, and (b) clay.

Despite the wide application of MIP in the construction industry, the numerous assumptions of

MIP can lead to a biased measurement of pore size [49], especially the cylindrical pore shape assumption. Past studies have pointed out the limitation and potential deviation of pore size measurement result from the cylindrical pore assumption in MIP [43, 49], but the correlation between the irregular pore shape and the cylindrical pore shape assumption in MIP is not addressed quantitatively. Metal intrusion technique, on the other hand, provides the possibility of study the pore shape information through direct observation of the shape of the pores.

In this Chapter, the pore shape parameters obtained from MI is used to correct the pore size measurement of MIP by modifying the biased pore shape assumption in Washburn's equation. Non-toxic field's metal is firstly used in metal intrusion technique to solve the safety issue. Comparison between the MI and traditional polymer impregnation illustrates the MI can greatly increase the contrast and reduce the imaging noise in pore images while retaining the sample integrity of silty clay samples. Based on the area-perimeter relationship reflected by the pore shape descriptor namely circularity, the biased pore shape assumption of Washburn's equation is modified to provide a more accurate estimation of the pore size by MIP. The two new pore shape descriptors, namely solidity and aspect ratio, are combined with PSD to interpret the transformation of pore features and pore shape in the cement hydration and consolidation of silty clay. The pore shape data from 2D observations is shown to have a statistical correlation with pore shape in 3D space. The pore shape analysis scheme presented in this Chapter is beneficial to the interpretation of the test results of MIP and future pore shape analysis of the construction materials.

3.2. Experimental program

3.2.1. MATERIALS AND INSTRUMENTATION

Type GP Ordinary Portland Cement, conforming to the requirements of Australian Standard AS 3972, was used to fabricate the cement paste sample. The soil investigated in this study is undisturbed silty clay samples obtained from Wuhan, China using drilling thin-walled. The soil samples were packed

in airtight containers to avoid evaporation loss after sampling. Two types of low-melting-point metal, whose properties are shown in Table 3-1, were purchased from Rotometals, Inc.

Table 3-1 Properties of low-melting-point metals used in this study

	Composition by weight	Melting point	Contact angle	Density
Wood's metal	50% Bi, 26.7% Pb, 13.3% Sn, 10% Cd	70°C [172]	130° [131]	9.38g/cm ³ [172]
Field's metal	32.5% Bi, 51% In, 16.5% Sn	62°C [132]	130° [131]	8.00g/cm ³

Two types of apparatus are applied to conduct the metal intrusion. The metal intrusion process of cement paste sample is conducted using centrifugation-based low-melting-point metal intrusion (CLMI) technique. The CLMI technique was conducted using an Eppendorf Centrifuge 5702 with the swing bucket rotor. The assembly of the intrusion device is shown in Figure 3-2. A set of aluminium containers was used to hold the sample and the melted metal in the swing bucket and plastic foam was used to reduce heat loss of the container. Centrifugal force was generated by the spinning rotor and the pressure increased with the depth of the melted metal as shown in Figure 3-2.

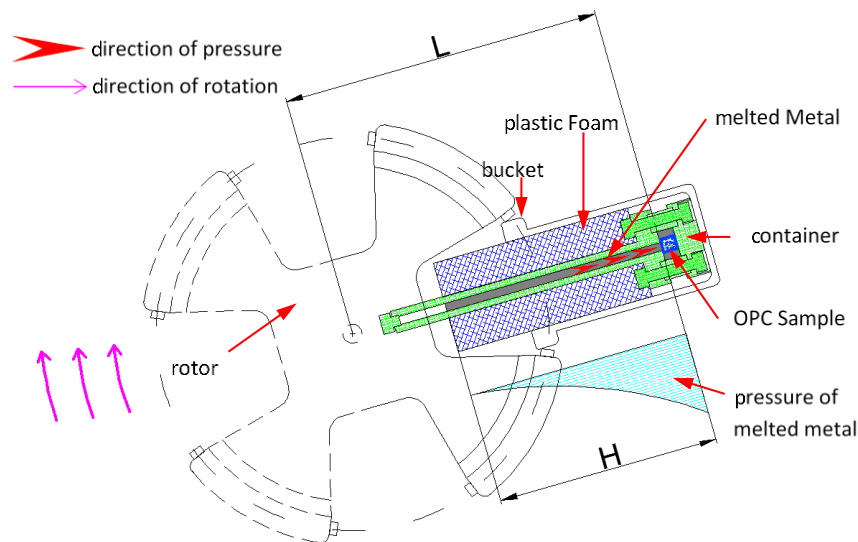


Figure 3-2 Schematic of CLMI instrumentation for sample preparation. Only one set of devices is demonstrated here; 2 or 4 sets had to be placed symmetrically on the rotor in centrifugation.

As for the soil sample, a custom-designed piston-cylinder apparatus [173] was used for the metal

intrusion process. A Shimadzu AG-X test machine was used for pressurizing. The principle of the instrument is pressurizing the molten low-melting-point metal in the pressure vessel by compression. As shown in Figure 3-3. An AutoPore IV 9505 mercury porosimeter was used to conduct MIP testing. The porosimeter could achieve a maximum pressure of 182 MPa and the corresponding minimum accessible pore diameter was about 8 nm. A Nova 450 SEM was used to conduct BSE imaging of both the cement paste and soil samples.

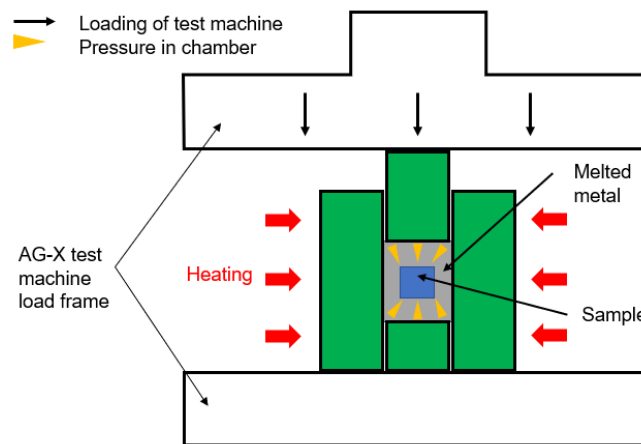


Figure 3-3 Schematic of apparatus used for metal intrusion

3.2.2. SAMPLE PREPARATION AND EXPERIMENTAL PROCEDURE

A high-speed shear mixer (CTE Model 7000) was employed to mix the cement paste samples following the mixing procedure of ASTM C1738-11. Two different w/c ratio of 0.4 and 0.8 were adopted for the mix design. For the cement paste with w/c of 0.4 and 0.8, one cubic cement sample approximately 5 mm×5 mm×5 mm for each mix design was taken from the cores of 20 mm cement paste cubes after being cured in saturated calcium hydroxide solution for 28 days and 7 days, respectively. Ethanol exchanging last for 28 days was used to stop hydration after sampling. The cement samples were reserved in vacuum for one week to remove liquids from the capillary pores. It should be noted that the number of samples for each mix design is determined by the number of BSE images, which is stated in section 3.2.3.

In the metal intrusion process of cement paste sample, samples were placed in the container as

shown in Figure 3-2. The container was heated to 95 ± 2 °C and filled with melted metal. Foam plastic insulator was used to reduce heat loss from the container. The centrifuge ran for 10 minutes to allow cooling-down of the container so that the intruded metal would solidify under pressure. The depth of the metal H was controlled to 82 ± 2 mm for all the samples.

The CLMI technique used for the metal intrusion of cement paste sample can generate maximum intrusion pressure around 15MPa. Based on Figure 3-2, the intrusion pressure P in the CLMI technique is calculated as:

$$P = \frac{1}{2} \rho \omega^2 (2L_1 H + H^2) / 10^9 \quad (3-1)$$

where ρ is the density of the melted metal, ω is the angular velocity (rad/s) of centrifuge, $L_1 = 48$ mm, is the distance from the center of the centrifuge to the surface of liquid metal in the tube, $H = 82$ mm, is the depth of liquid metal to the upside of the cement paste sample.

Ten cement paste samples were prepared using CLMI as shown in Table 3-2. C1 and C2 are calibration samples, where Wood's metal with higher density was used to generate higher pressure (15.2 ± 0.34 MPa based on Eq. (3-1)) at 4400 revolutions per minute (rpm) in order to obtain baseline information of the pores. The baseline information was used to develop relationships between pore shapes and the Washburn's equation. The non-toxic Fields' metal was used to prepare the other 8 verification samples V1-V8 with different intrusion pressure, which were prepared at speeds (pressure) of 200 rpm (0.03 ± 0.0005 MPa), 1100rpm (0.77 ± 0.0173 MPa), 2200rpm (3.10 ± 0.069 MPa), and 4400rpm (12.4 ± 0.28 MPa). These verification samples were used to verify the modified Washburn's equation of cement paste developed in this study.

Table 3-2 Sample information of soil samples

Sample Name	w/c	Age (days)	Centrifuge Speed (rpm)	Intrusion Pressure (MPa)
C1	0.4	28	4400	15.2 ± 0.34
C2	0.8	7	4400	15.2 ± 0.34
V1	0.4	28	200	0.03 ± 0.0005
V2	0.4	28	1100	0.77 ± 0.0173
V3	0.4	28	2200	3.10 ± 0.069
V4	0.4	28	4400	12.40 ± 0.28
V5	0.8	7	200	0.03 ± 0.0005
V6	0.8	7	1100	0.77 ± 0.0173
V7	0.8	7	2200	3.10 ± 0.069
V8	0.8	7	4400	12.40 ± 0.28

For the soil samples, uniaxial consolidated silty clay samples with consolidation pressures of 0 kPa (C-0), 600 kPa (C-600), and 3200 kPa (C-3200) were prepared in accordance with soil test method standards GB_T50123-1999 [174]. The soil samples were then dried in ventilated ovens at $105 \pm 1^\circ\text{C}$ for 24 hours. MIP was performed for C-0 and C-600 sample to verify the modified Washburn's equation of soil developed in this study.

After the drying process, cubic soil samples approximately $5\text{mm} \times 5\text{mm} \times 5\text{mm}$ in size were taken from the cores of undisturbed silty clay cylinders to do the metal intrusion. In the metal intrusion, the dried samples and molten metal were placed in the pressure vessel of the piston cylinder apparatus. Controlled temperature ($90 \pm 2^\circ\text{C}$) was generated by the furnace and monitored by a thermocouple during the metal intrusion process. The intrusion pressure increased evenly to the peak pressure of 400 MPa at the rate of 12.5 MPa/min. The peak pressure was then held for 20 minutes to guarantee the intrusion of the metal. After the pressure holding stage, the pressure vessel was cooled to room temperature to ensure the solidification of intrude metal.

Epoxy impregnation [175] was conducted to prepare the calibration soil sample (C-3200) to verify the influence of metal intrusion on the sample integrity of soil samples.

All the samples prepared by the metal intrusion and epoxy impregnation were ground and polished to retain their plane surface. The first grinding stage was performed with sandpaper of four

grades (125 μm , 58.5 μm , 25,8 μm , and 15.3 μm). The polishing stage was performed using polishing cloths with four grades of ethanol/diamond grit polishing suspensions (6 μm , 1 μm , 0.25 μm , and 0.1 μm). After each particle/grit size, the samples were cleaned ultrasonically in ethanol to remove grit.

3.2.3. BSE IMAGES AND IMAGE ANALYSIS

To prevent charging before imaging, each sample's surface was coated with a thin layer ($\sim 10\text{nm}$) of carbon. For each cement paste sample, five backscattered electron images were taken randomly at the centre of the sample at the magnification of $1000\times$ using low energy electron (5 keV), more than 50000 pore profiles were obtained for each cement paste sample. For each soil sample include the sample prepared by metal intrusion and epoxy impregnation, an area of $5.461\times 10^6\mu\text{m}^2$ was scanned with BSE imaging using a low-energy electron (5keV) at the magnification of $100\times$. More than 110,000 pore profiles were observed for each soil sample.

Are five images enough to achieve acceptable sampling confidence for cement paste sample? A statistical method at 95% degree of confidence proposed by Zhao and Darwin [176] was used to determine the number of images required to achieve given confidence levels. It was determined that the 5-image sets for cement pastes provide a value for pore fraction that is within 17% of the true value, a margin of error that is reasonably small.

In our study, intruded pores were identified by thresholding the grey levels of the pores to produce binary images. For the cement paste sample used here, ISODATA thresholding method [177] was used to obtain binary images of the pores. As for the soil samples, the threshold grey levels used to segregate porosity and solid phases were selected by a technique based on the grey-level histogram of each sample. The different phases, namely sand, clay, silt, and pore in the BSE images were first distinguished by fitting the grey-level histograms with multiple Gaussian distributions. The volume fraction of each phase was then computed by integration of the corresponding Gaussian distributions over the grey-level domain. An iterative process was then used to obtain the threshold value that

produced a consistent volume fraction as the pore phase. The detailed process of this process is shown in Section 3.3.1.

The binary image images obtained by thresholding were analyzed using the software package, ImageJ, which is a widely used image processing program. This algorithm finds the connected regions of white pixels (white represents pores) on the binary image with an eight-directional connection setup. The characteristic descriptors for each pore profile were analyzed using the inbuilt ImageJ algorithm.

3.3. Performance of metal intrusion technique

Figure 3-4a-b show the BSE images of calibration soil samples (C-3200) prepared by metal intrusion and epoxy impregnation, respectively. Low-energy electron and long electron beam dwell time were adopted to acquire these images. A clear difference of pore profile can be seen between BSE images using the two methods. For sample prepared by metal intrusion, the pores filled with metal appear as very bright signal in the images, whereas in the epoxy impregnated sample the pores appear as darker regions.

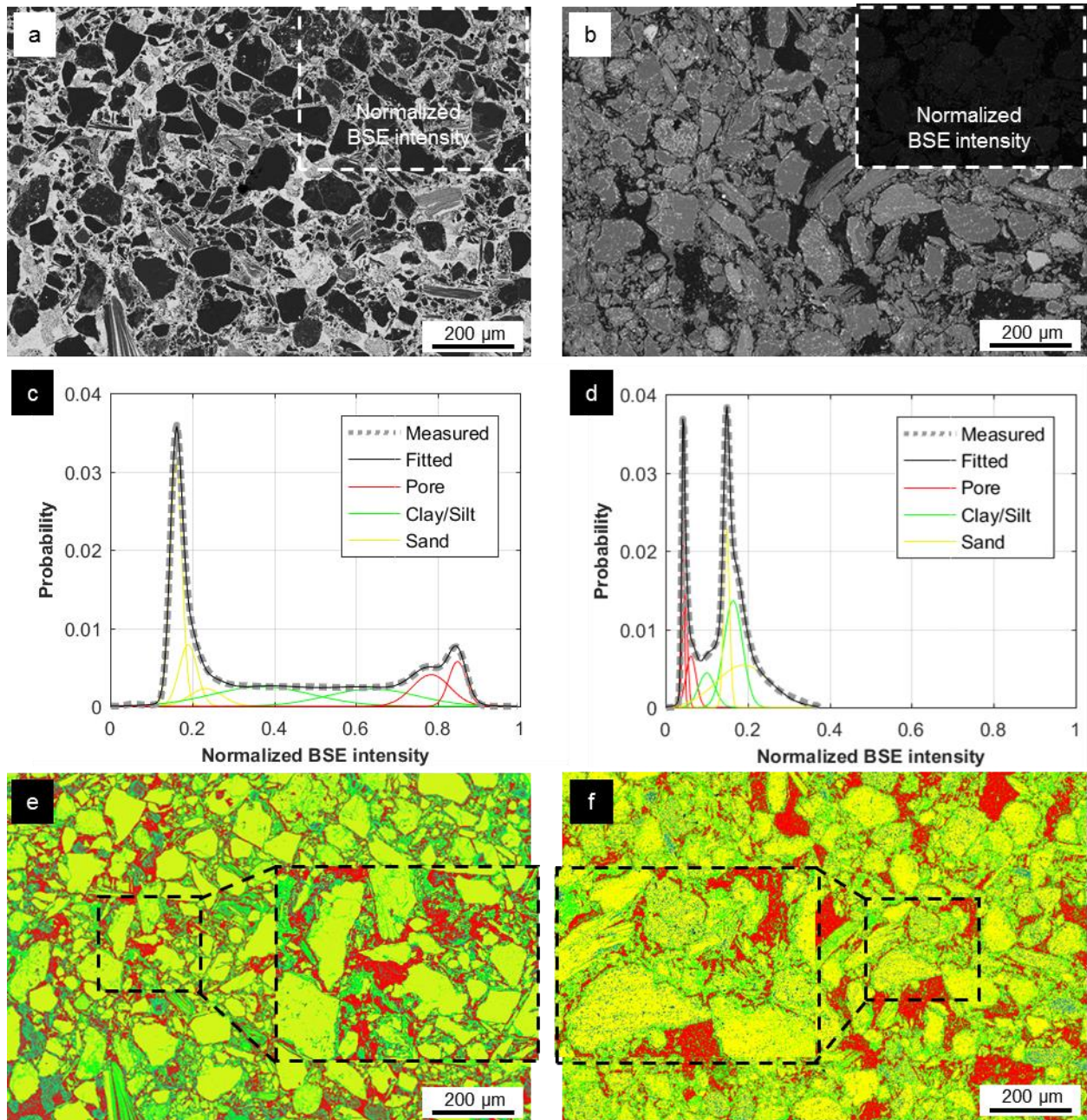


Figure 3-4 (a), (b) Typical BSE images of calibration samples prepared by metal intrusion and epoxy impregnation, the top right region show the images obtained by normalizing BSE intensity; (c), (d) normalized BSE intensity distribution for different phases in samples prepared by metal intrusion and epoxy impregnation; (e), (f) colored images of samples prepared by metal intrusion and epoxy impregnation based on the Gaussian distribution of phases (red-pore, green-clay/silt, yellow-sand).

It should be noted that different scaling of the BSE intensity signals was applied in Figure 3-4a and b in order to produce visible contrasts in the BSE images. When the same scaling of the BSE intensity signals is adopted, in other words, when the BSE image is plotted based on normalized BSE intensity, the two samples prepared by different methods appear as the top right regions of Figure 3-4a and b (in the rectangular boxes). Comparison of the images with normalized BSE intensity shows

that the signal intensity of pores from the epoxy impregnated sample is lower, as the images appear darker (the top right regions in Figure 3-4b).

This difference is also illustrated in Figure 3-4c and d in a qualitative way, where the BSE intensity of different phases [178, 179] was fitted by multiple Gaussian distributions. The mean and standard deviation of the fitted Gaussian distributions are obtained by an iteration process until the R-squared for these fittings is larger than 0.999. By replacing the epoxy resin with metal, the normalized BSE intensity of pores is shifted from 0.051 to 0.809.

Figure 3-4e and f show coloured images (based on Figure 3-4a and b) that demonstrate the effect of the grey level of the image on the pore profiles identification. Coloured images are obtained by assigning two grey-level thresholds based on corresponding Gaussian distributions for pore, silt/clay, and sand, and colouring the pixels in the three phases as red, green, and yellow respectively. Thresholding is a commonly used method to identify profiles of different phases from image data [180]. Comparison between Figure 3-4e and f show that the number of identifiable features and imaging noise in the sample prepared by the two methods are different. In Figure 3-4e, a sharp boundary between pores with other phases and features smaller than $10\mu\text{m}$ can be clearly observed, whereas a large amount of imaging noise in Figure 3-4f blurs the pore boundary, making it impractical to properly trace the pore profiles by software.

The advantage of sharp contrast and low imaging noise in the sample prepared by metal intrusion due to that the metal filled in the pores can strongly reflect electrons in SE imaging. Imaging noise result from the overlapping of BSE intensity of different phases is reduced due to the high contrast in chemical composition between pore filled with metal (In, Bi, Sn) and soil matrix (Si, C, H, O, etc.).

For samples exposed to high intrusion pressure in the metal intrusion process, pore structural stability and sample integrity need to be considered. Because polymer impregnation can preserve the microstructural integrity of soil [181], the influence of high-pressure metal intrusion on pore structure was investigated by comparing the pore volume fraction of sample (C-3200) prepared by epoxy

impregnation and metal intrusion.

Table 3-3 summarizes the volume fraction of different phases in calibration soil samples quantified from the Gaussian distribution fitting. The volume fraction of each phase is obtained through integration of the summed area of the corresponding Gaussian distributions [182, 183]. It can be seen that the difference between the volume fraction of pore obtained from the sample prepared by the metal intrusion and the epoxy impregnation is less than 1.8%. And the difference in the volume fraction of sand and clay/silt both less than 1.5%. Since the damage and collapse of pores in metal intrusion process can alter the pore volume fraction, the small difference in volume fraction of each phase indicates that minimal change in the pore structure is caused by the metal intrusion. This observation is consistent with the effect of MIP on pore structure and sample integrity reported in the literature.

Table 3-3 Volume fraction of phases obtained by Gaussian fitting

		Pore			Clay/silt		Sand	
Epoxy Impregnation	Peak BSE intensity	0.043	0.047	0.062	0.100	0.164	0.148	0.190
	Percentage	6.96%	7.49%	7.02%	7.49%	26.80%	13.88%	30.36%
Metal intrusion	Peak BSE intensity	0.784	0.847		0.380	0.639	0.161	0.188
	Percentage	11.94%	7.80%		19.41%	15.41%	28.76%	11.14%
		Volume Fraction						
Method		Sand			Clay/Silt		Pore	
Metal intrusion		45.67%			34.82%		19.74%	
Epoxy impregnation		44.24%			34.29%		21.47%	

In traditional MIP, high intrusion pressure up to 400 MPa is also necessary to force the mercury into the fine pores of samples. Extensive studies of soil microstructure integrity in MIP have been conducted to investigate the effect of high pressure in MIP, demonstrating that MIP does not cause microstructure change or alteration of the PSD of soil samples. Sridharan et al. [184] conducted the MIP of weak clay samples and showed that MIP did not change the topographic outline samples. The experimental study of Lawrence reported that a multi-intrusion run presented similar PSD, which indicated MIP did not cause microstructural deformation of soil samples [185]. Sills et al used gas

sorption and MIP to analyze the pore structure of soil, the results showed that MIP did not alter the PSD of micropores [186]. Thus, the minimal effect on sample stability and integrity in MIP reported in existed research, along with the result presented in this section, indicate that high-pressure metal intrusion is unlikely to affect the pore structure of the soil samples.

Figure 3-5 shows the typical binary images of pores for cement paste sample obtained by thresholding method. As shown in Figure 3-5, the analysis could successfully distinguish the pores (black pixels) from the cement (white pixels) based on the thresholding method. As demonstrated in Figure 3-5c and d, the thresholding method can capture profiles of the pores, allowing accurate measurement of the pore perimeter and shape information.

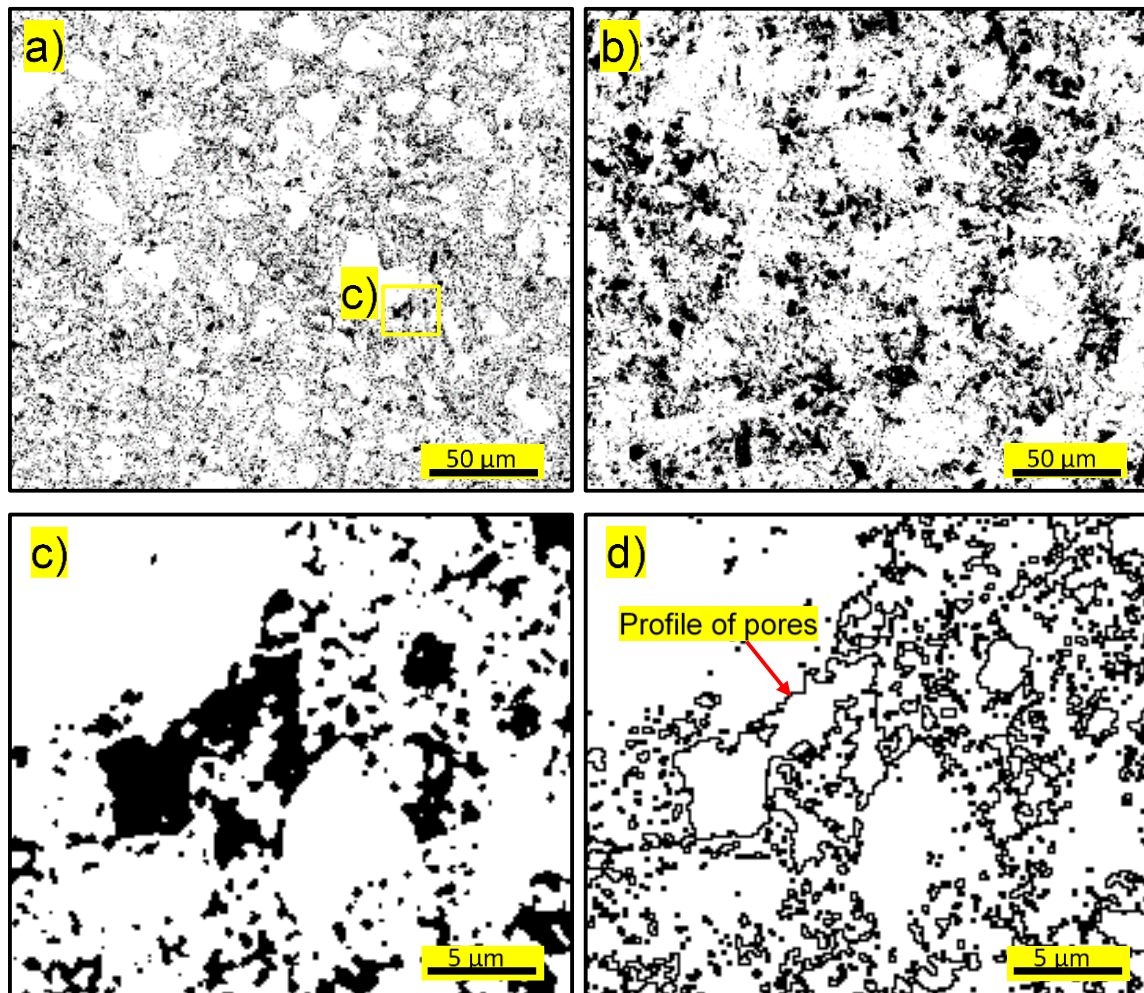


Figure 3-5 Typical binary images of pores (black) for (a) sample W3, w/c=0.4, 10cycles, 15.2 MPa and (b) sample W5, w/c=0.8, 4cycles, 15.2 MPa.

In terms of pores size, the definition and representation of pore size needed to be considered. Current conventions often based on cylindrical pore shape assumption and use pore diameter to represent the size of a pore [187-189]. However, as shown in Figure 3-5d, the shape of the pores was hardly circular, and most of the pores lacked the diameter. To be coherent with the conventions where pore size is often expressed as diameter, the equivalent pore diameter (d_p) was applied to describe the pore size and subsequent pore analysis. The d_p of an irregular pore with the given area was calculated as:

$$d_p = \sqrt{\frac{4area}{\pi}} \quad (3-2)$$

under the current magnification, the smallest identifiable pore (which represented by a single pixel in binary images) of cement paste sample and silty clay sample are 20nm and 200nm, respectively.

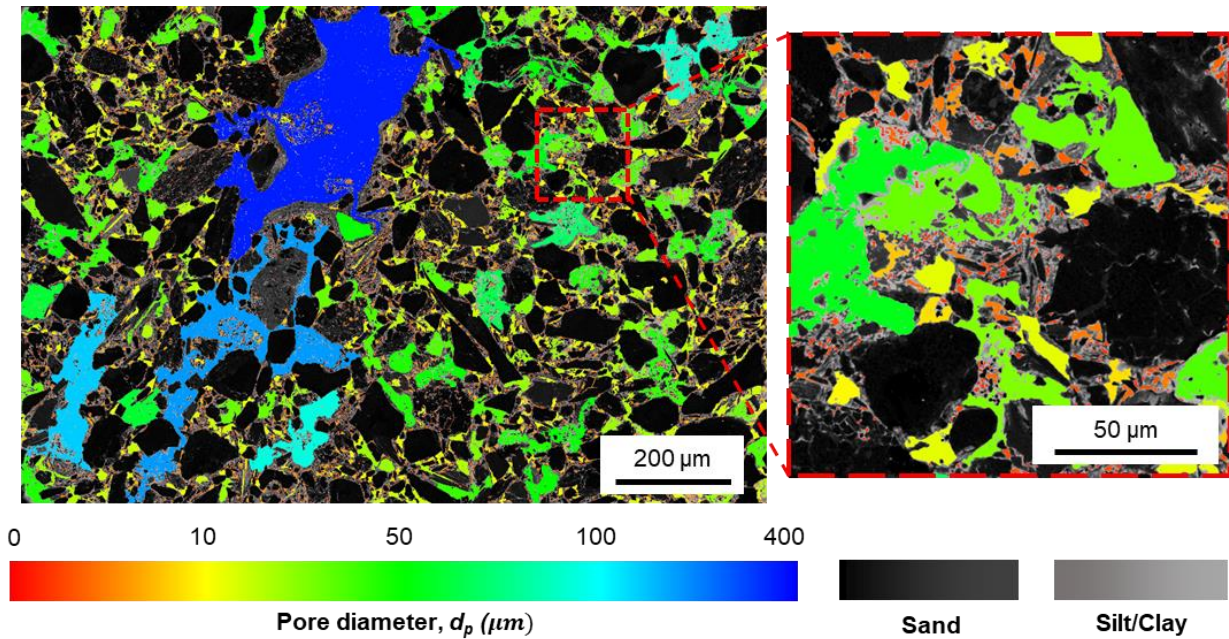


Figure 3-6 Equivalent pore diameter based coloured image of metal intruded sample (C-0)

Figure 3-6 shows coloured images of silty clay sample in which pores are coloured based on the d_p . It can be seen that pores smaller than few hundred nanometers are mainly embedded in the clay/silt particles, which larger pores with d_p range from several microns to around 400 μm mainly packed

between the sand and clay/silt particles.

3.4. Non-cylindrical pores and its correlation with Washburn's equation

The previous section demonstrated that metal intrusion can effectively enhance the identification of pore profiles in BSE images while maintaining the pore structure integrity of samples. In this section, a shape descriptor called circularity (C) is used to describe the area-perimeter relationship of pores and correlated with Washburn's equation to correct the biased pore size measurement of MIP.

The Circularity measures how closely the shape of a pore appear as a perfectly circular shape.

The circularity of a noncircular pore is calculated as:

$$C = 4\pi \frac{\text{area}}{\text{perimeter}^2} \quad (3-3)$$

C equals to 1 when the pore is mathematically perfectly circular. C decreases when the pore has curving features or large elongation.

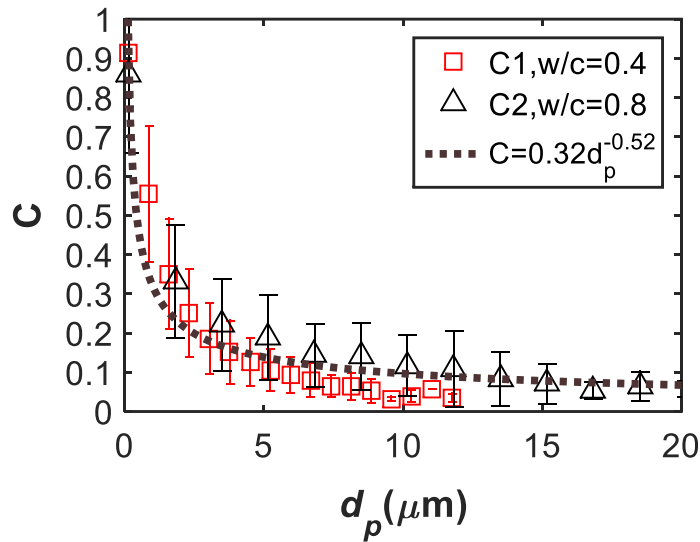


Figure 3-7 Circularity (C) of pores with different sizes (equivalent diameter, d_p) for 7-day cement paste sample with $c/w = 0.4$ (C1) and 28-day cement paste sample with $w/c = 0.8$ (C2). The overall C- d_p is fitted with an inverse power function $C=0.32d_p^{-0.52}$.

Figure 3-7 shows the circularity- d_p distribution of the 7-day and 28-days cement paste samples. It can be seen that C increases as d_p decreases. The difference between circularity- d_p distribution of 7-day

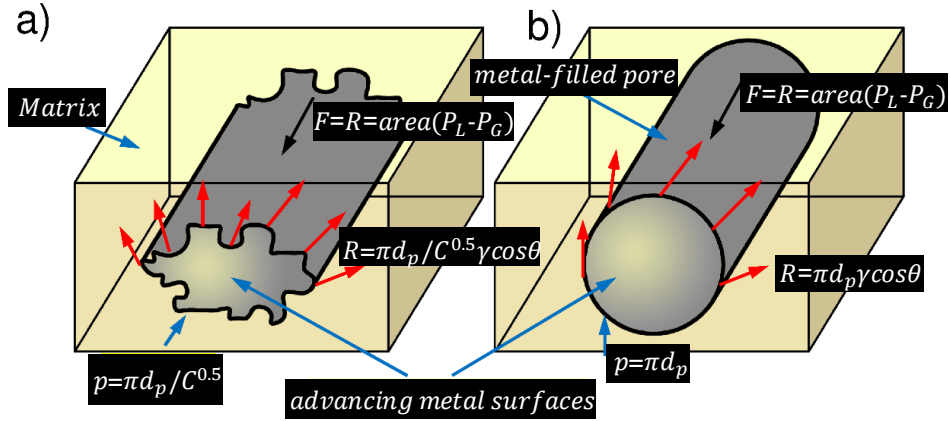
and 28-day cement paste samples is small, indicating a universal $C-d_p$ relationship exists for pore of cement paste, which is independent to the w/c ratio. The circularity- d_p distribution is found to follow an inverse power correlation given as:

$$C = a \cdot d_p^{-b} \quad (3-4)$$

The fitted equation used to describe the $C-d_p$ relation of pores of cement paste is found to be $C=0.32d_p^{0.52}$. This equation yields a good general fit for both the 7-day and 28-day cement paste samples.

The $C-d_p$ relation describes the relationship between the pore area and the perimeter, which is essential for MIP. In the MIP, the pore diameter can be derived based on the applied pressure that forces the mercury into the interconnected pore of the specimen using Washburn's equation [87]. This equation is based on the area-perimeter relationship of cylindrical pores by assuming that the pores have a perfect circular shape.

Figure 3-8 shows the intrusion process of the non-wetting liquid (mercury in MIP) into an irregular pore (Figure 3-8a) and a circular pore (Figure 3-8b). In Washburn's equation, it is assumed that there is only one advancing liquid metal surface and the cross-section of the pore is constant. In Figure 3-8a and b, the driving force F of the two pores are the same, being the product of the pore area and the applied intrusion pressure. It should be noted that d_p is an equivalent measure of pore size and therefore area equals $\pi d_p^2/4$ for both pores. The driving force F is balanced by the sum (R) of the surface tension ($\gamma \cos \theta$ indicated by red arrows in Figure 3-8) that acts at the edge of the advancing liquid surface. R is proportional to the length of the pore perimeter. The perimeter of an irregular pore with $C < 1$ (Figure 3-8a) is larger than that of a circular pore (Figure 3-8b).



0

Figure 3-8 Schematic for the effect of circularity on metal intrusion into an irregular pore (a) and (b) a circular pore. F : intrusion force. R : resistant force. p : perimeter of pore. $\gamma\cos\theta$: surface tension (per unit length of pore perimeter) parallel to the direction of intrusion.

Using Eq. (3-1), Washburn's equation can be corrected to consider the true area-perimeter relation in pore analysis. The force equilibrium between applied pressure and surface tension can be expressed as:

$$P \times area = -\gamma\cos\theta \times perimeter \quad (3-5)$$

$$area = \frac{\pi}{4}d_p^2 \quad (3-6)$$

$$perimeter = \sqrt{\frac{4\pi \times area}{C}} \quad (3-7)$$

where P is the pressure applied on non-wetting liquid, γ is the surface tension of the mercury, θ is the contact angle between mercury and pore wall. The cylindrical pore assumption applied the circularity of 1 and the Washburn's equation can be obtained by substituting Eq.(3-6), (3-7) into Eq. (3-5):

$$P = -\frac{4\gamma\cos\theta}{d_p} \quad (3-8)$$

Given the C - d_p relation obtained in Figure 3-7, the force equilibrium in Washburn's equation can

be modified based on the area–perimeter relation of different samples by substituting equations (3-4), (3-6) and (3-7), into equation (3-5), so that the pressure-equivalent pore diameter relation is shown as:

$$P = -\frac{4\gamma\cos\theta}{d_p \times \sqrt{C}} = -\frac{4\gamma\cos\theta}{\sqrt{a} \cdot d_p^{1-\frac{b}{2}}} \quad (3-9)$$

The effectiveness of this modified Washburn's equation was verified experimentally for both cement paste samples and soil samples. For the cement paste sample, the intrusion pressure in CLMI can be accurately controlled by altering the spinning speed of the centrifuge. Figure 3-9 shows the BSE images of cement paste sample obtained at different intrusion pressures. At very low intrusion pressure (Figure 3-9a), large ($>10\ \mu\text{m}$) and shallow pores are visible at the surface. As the intrusion pressure increases (Figure 3-9b), a few large pores are unfilled, and some deep pores are still visible. The visual differences between the sample prepared with 3.10MPa (2200 RPM) and 12.4MPa (4400RPM) are small (Figure 3-9c and d). It appears that pressure of 3.10MPa allows the penetration and filling of most of the large pores.

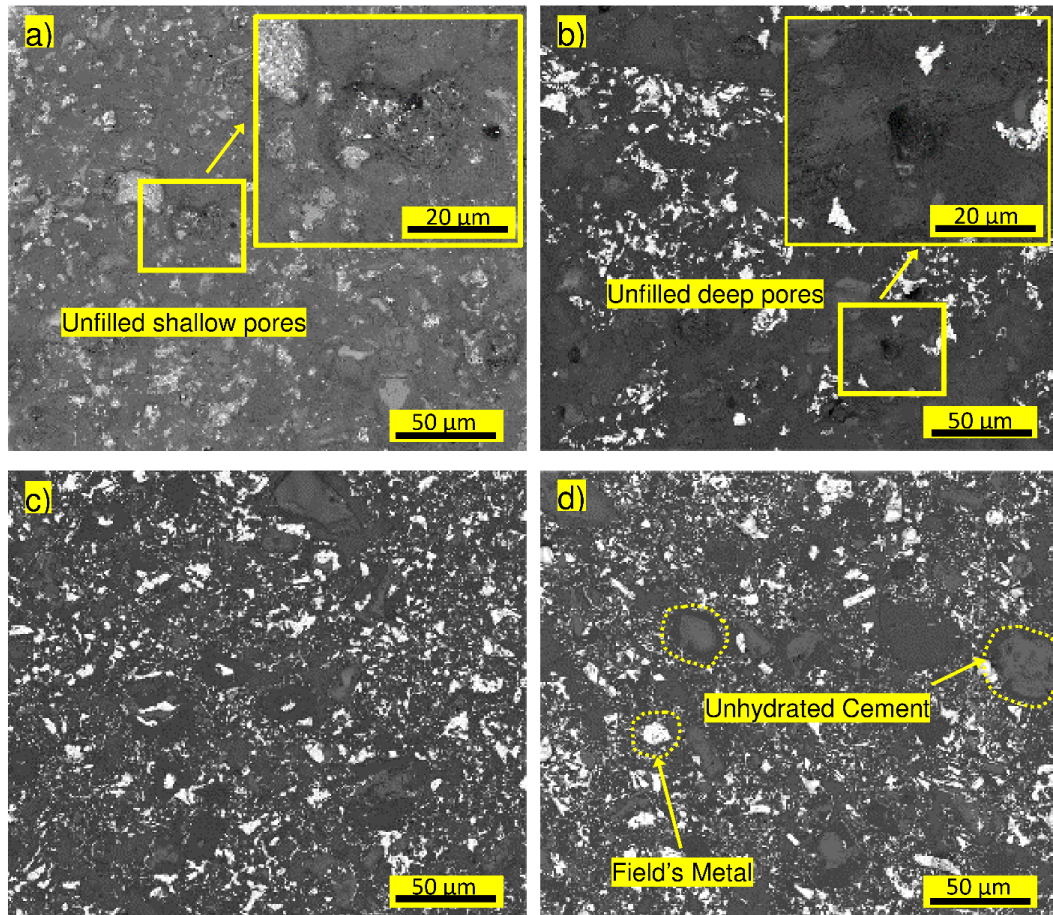


Figure 3-9 BSE images of metal intruded samples with $w/c=0.8$, 4 cycles and under different centrifuge pressures: (a) 0.03MPa (200 RPM) and magnification of unfilled shallow pore; (b) 0.77MPa (1100RPM) and unfilled deep pore; (c) 3.10MPa (2200 RPM); (d) 12.4MPa (4400RPM).

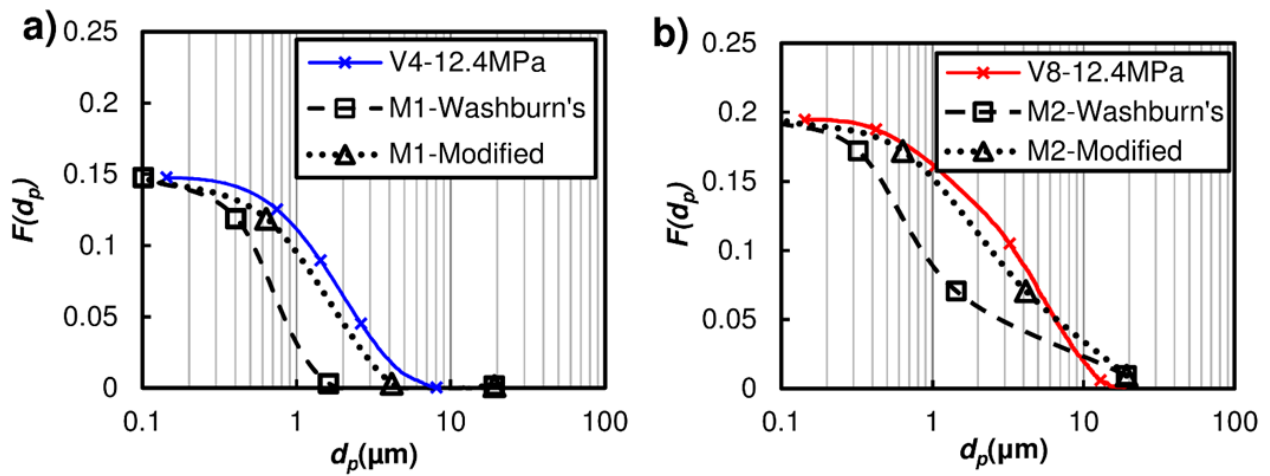


Figure 3-10 F distribution of samples under different centrifuge speeds obtained by metal intrusion technique, Washburn's equation and modified equation [Eq. (3-9)].

Figure 3-10 shows the cumulative porosity as a function of d_p (F distribution) of cement paste sample increase with increased intrusion pressure. It is suggested here that the effect of pore perimeter can be indicated by comparing the F distribution (at 12.4 MPa) observed from MI and the calculated F distribution based on the porosimetry method. The porosimetry method used here obtains the total observed pore volume fracture from image analysis of V1-V8 and calculates the corresponding pore diameter based on intrusion pressure by using Eq. (3-2) and (3-9), in which parameter a and b equal to 0.32 and 0.52, respectively. The corresponding pore size that can be intruded at each pressure is calculated based on Eq. (3-2) and plotted in Figure 3-10. It can be seen that for the 28-day 0.4 sample (Figure 3-10a), the F distribution obtained from metal intrusion is very different from the F distribution obtained from porosimetry measurement. We deduce, therefore, that porosimetry measurement using Washburn's equation can be modified with C - d_p relationship to produce F distribution results that are much closer to the direct measurement. The same situation is evident for the 7 days 0.8 w/c sample. The F distribution obtained by modified Washburn's equation is much closer to the observed F distribution by MI.

The modified Washburn's equation based on the area-perimeter relationship of pores is also found to be effective in studying the pores of soil. The fitted parameters of the C - d_p distribution at the 99% confidence level for the C-0 and C-600 samples are listed in Table 3-4.

Table 3-4 Fitted parameters for C-0 and C-600 samples

		a	b
C-0	Upper limit	0.9891	0.8496
	Lower limit	1.1004	0.7876
C-600	Upper limit	0.5043	0.6891
	Lower limit	0.5710	0.5956

Figure 3-11 compares the F distribution of C-0 and C-600 samples obtained from metal intrusion, MIP, and the F distribution based on modified Washburn's equation. The shaded area represents the range of modified F distribution based on parameters of the corresponding sample with the confidence

level of 99%. For the C-0 sample (Figure 3-11a), it can be seen that the difference between the total porosity calculated by the metal intrusion and MIP is less than 5%. However, the F distribution obtained from MIP is very different from that of the result of metal intrusion, and MIP does not measure the pore with $d_p > 90\mu\text{m}$. As shown in Figure 3-11(a), the accuracy of MIP measurement can be significantly improved by modified Washburn's equation. The modified F distribution becomes closer to the results of MI, especially for pores larger than $90\mu\text{m}$. These large pores play a key role in determining permeability and bearing capacity. The situation is the same for the C-600 sample, where the modified F distribution of MIP is closer to that of the direct visualized F distribution from MI. Based on the effective modification on F distribution of cement paste and soil sample presented above, we suggest here that MIP test results can be improved by using the modified Washburn's equation based on $C-d_p$ relationship to provide a more accurate reflection of the true pores sizes.

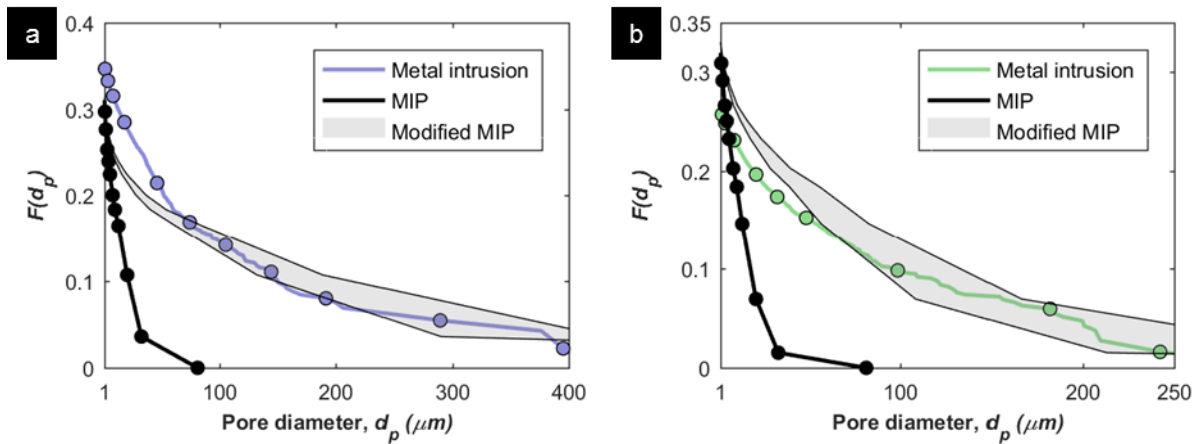


Figure 3-11 F distributions of samples obtained by image analysis, Washburn's equation and modified equation [Eq. (3-9)] for (a) C-0 sample and (b) C-600 sample.

3.5. Pore shape analysis and its link with microstructure transformation

In this section, the PSD and pore shape descriptors (Solidity, aspect ratio) are used to describe the transformation of pore structure in the hydration procedure of cement samples and the consolidation of silty clay samples. A statistical correlation is presented to illustrate the link between the pores shape from 2D observation and pore shape in 3D space.

Figure 3-12a shows the F distribution obtained from imaging analysis of the soil samples. A clear difference in the total porosity can be seen between the samples experienced different consolidation pressures. The C-0 sample has not experienced the consolidation process, therefore shows the highest pore volume fraction of 0.351 in the pore range from 0.2 μm to 380 μm . As the consolidation pressure increase, the pore structure of the soil is deformed and the pore volume fraction decreases. The pore volume fraction of the C-600 sample decreases to 0.265 and the C-3200 sample that experienced the highest consolidation pressure shows the lowest pore volume fraction of 0.197.

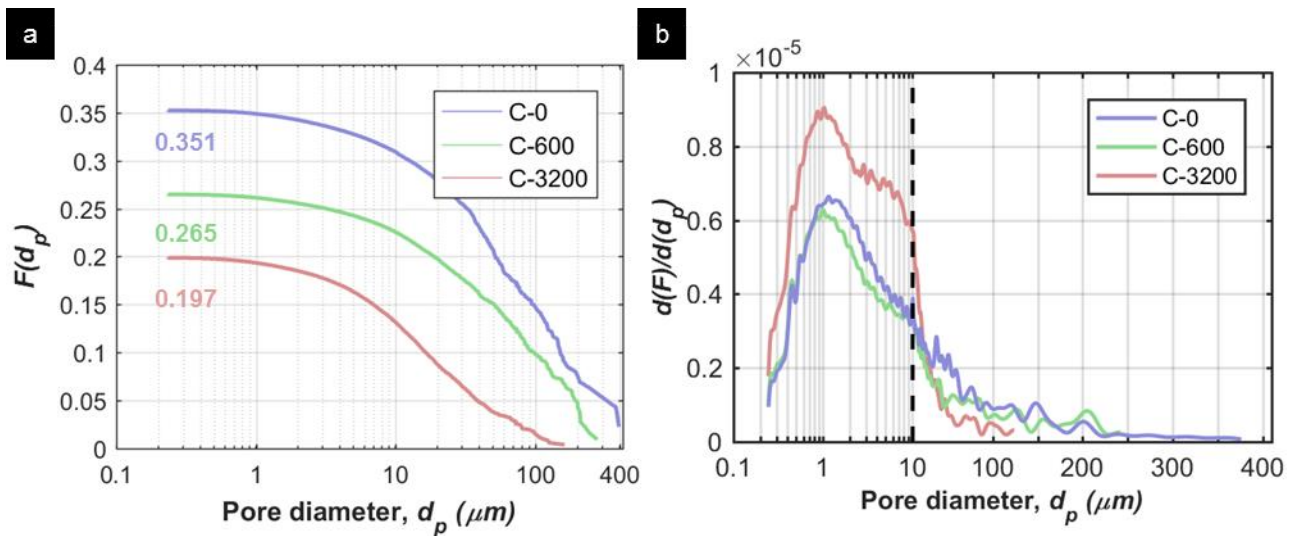


Figure 3-12 (a) Pore volume fraction of soil samples in relation to equivalent pore diameter, (b) PSD of soil samples. The numbers in (a), indicates the corresponding total pore volume of each curve.

PSD is applied to analyze the transformation in the relative abundance of each pore size due to the consolidation [190], which is obtained by the derivative of F distribution by d_p . Figure 3-12b shows the PSD of soil samples. It can be seen that the PSD of the C-0 sample has the widest pore size range of 0.2-380 μm , compared with that of the C-600 (0.2-250 μm) and C-3200 (0.2-150 μm) samples. The densification effect induced by consolidation is the main reason for shrinkage of the range of d_p [96, 191]. In the densification, the larger pores with d_p of several hundred microns collapsed during the consolidation process.

As shown in Figure 3-12b, the PSDs of the C-0 and C-600 samples show a similar pattern. Compared to C-0, the PSD of C-600 has two uniform reductions. The average drop in probability for

d_p ranges of 1-10 μm is 12.3% while for d_p ranges of 10-100 μm the average drop is 28.1%. In contrast, the consolidation pressure of 3200 kPa (C-3200) causes a notable change in the PSD compared with the C-0. When the consolidation pressure reaches 3200MPa, a significant increase of 56.8% in probability for d_p smaller than 10 μm is observed, while the probability of pores with d_p larger than 10 μm is decreased by 50.6 % in average. The significant transformation in the PSD of the C-3200 sample indicates that the consolidation process caused the formation of smaller ($d_p < 10\mu\text{m}$) pores. The collapse of larger pores and the formation of smaller pores in the consolidation leads to the alteration of PSD.

Figure 3-13a shows the F distribution of cement paste sample. The pore size range from 0.1 to 50 μm is observed in cement paste samples. A clear difference can be seen between the two samples, C2 has a higher w/c ratio and shorter hydration time, and therefore shows a much larger pore volume fraction of $F=0.27$ in the pore range compared with that of C1 ($F=0.19$). Figure 3-13b shows the PSD of the two samples, the PSD is smoothed by plotting using a moving average of 20 points. It can be seen that the difference is due to the larger number of pores with $d_p > 10 \mu\text{m}$ in the C2 sample. More detailed information for pores smaller than 10 μm can be shown in the PSD. Figure 3-13b show that C2 has more significant peaks than C1 in the range of 5-8 μm , indicating that C2 has more large pores. In contrast, C1 shows a larger amount of pores in the range 500 nm to 3 μm (small capillary pores) due to the higher degree of hydration [192].

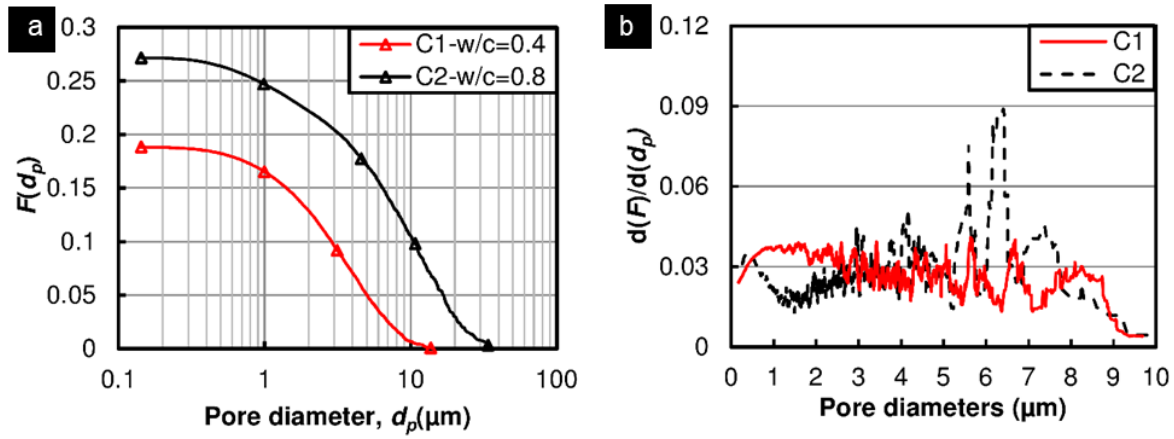


Figure 3-13 (a) Pore volume fraction of cement paste samples in relation to equivalent pore diameter; and (b) PSD of cement paste samples.

In terms of pores in the evolution process of samples, the pore shape transformation needs to be considered to describe the number of features on the pore walls and the elongation of pores. Solidity and aspect ratio are applied to describe these pore properties.

The solidity (S) of a noncircular pore with a certain area is calculated as:

$$S = \frac{\text{area}}{\text{convex area}} \quad (3-10)$$

where the convex area is the area of a convex hull that fully encapsulates the pore. When a pore has no rough features on its wall, the convex area equals the pore area and yields the solidity of one. However, most pores observed in the BSE images have rough features on their wall, as shown in Figure 3-5a.

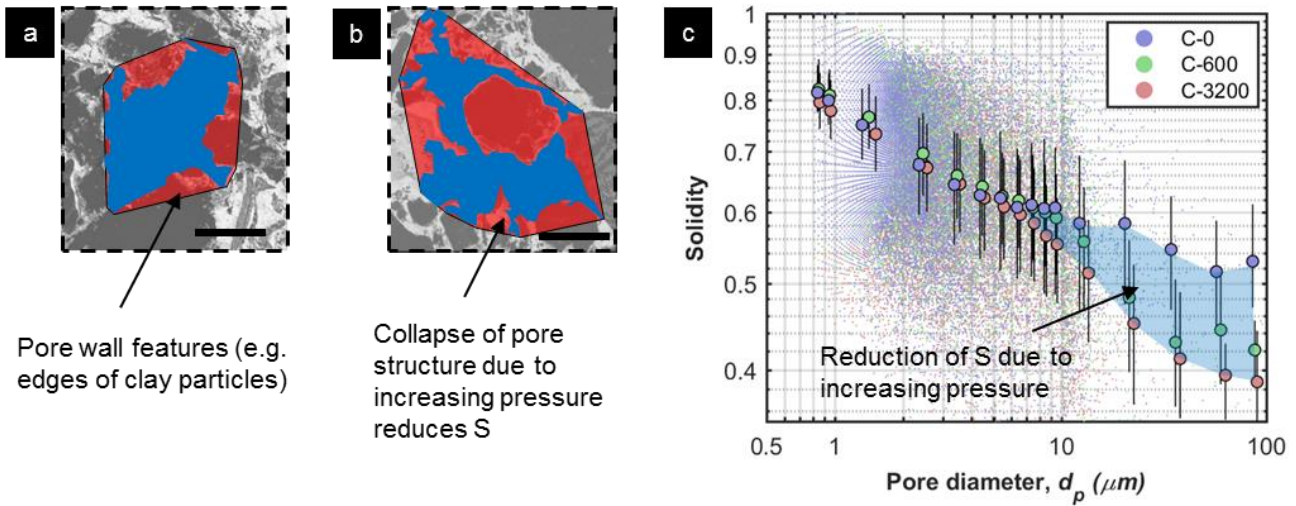


Figure 3-14 Figure 4 (a), (b) Typical pressure-induced transformation on Solidity of undisturbed silty clay from 0kPa (a) to 3200kPa (b). Scale bar: 50μm. Blue: void in pore. Red: features on the wall of a pore. (c) Solidity- d_p relationship.

Figure 3-14a and b show typical transformation of solidity as consolidation pressure increase. These two pores extracted from the BSE images of C-0 and C-3200 samples both have the d_p of 80 μm. Compared with the pore profile shown in Figure 3-14a (C-0), the pore in Figure 3-14b (C-3200) shows a larger number of rough features induced by the consolidation process. Rougher pore features results in a larger convex area and hence lower pore solidity.

Solidity can be used as an indicator of the effect of the consolidation process on the pores. Figure 3-14c shows the S - d_p relation of three samples experienced different consolidation pressure. As the consolidation pressure increase, the S decreases gradually. C-3200 sample displays the lowest S among the three samples for d_p drop into the range of 6–100μm, which is due to the highest degree of structural deformation in the consolidation. As d_p decreases, the difference in S among the three samples gradually decrease and shows a similar pattern when the d_p is smaller than 6μm. Also, the S varies in all samples regarding of d_p . S increases with the decrease in d_p for all samples, the reason is that smaller pores are less likely to have a large number of rough wall features.

In cement paste samples, S can be used as an important indicator for the effects of hydration and packing, as shown in Figure 3-15. In the pores of the cement paste sample, these pore features (yellow in Figure 3-15a) are the cement grain surfaces or hydration products. If a hydration reaction proceeds

within the pore, the newly grown hydration product as shown in Figure 3-15b deposit onto pore wall as features, hence reducing S . As indicated in Figure 3-15c, S for the $w/c=0.4$, 28-day sample is lower than that for the $w/c=0.8$, 7-day sample, especially when $d_p=2$ to $10\ \mu\text{m}$, due to higher degree of hydration and packing. In addition, it can be seen that S decreases as pore diameter increases, this is because that larger pores are more likely to have greater wall features (e.g. hydration products) and thereby lower S value compared to smaller pores.

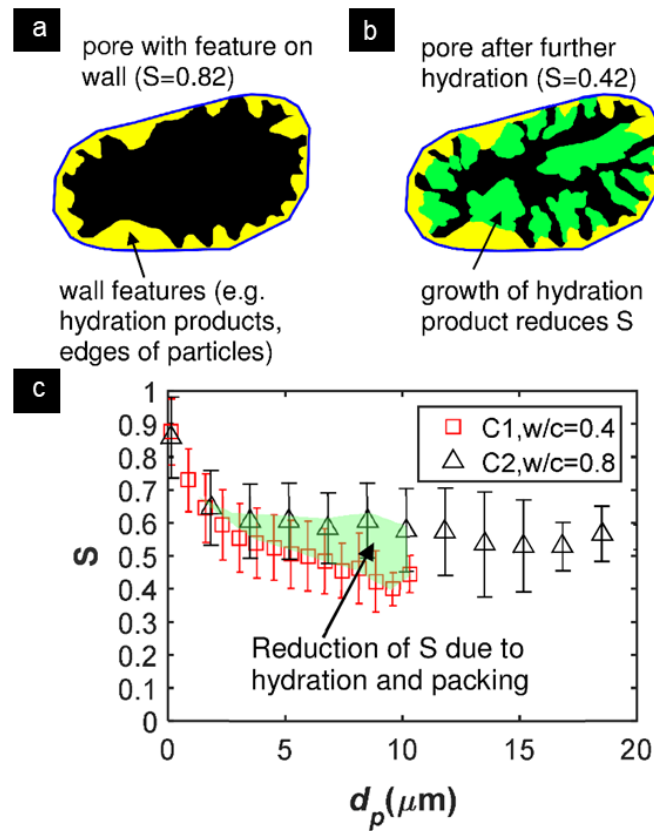


Figure 3-15 (a) ~ (b) Change of solidity due to hydration. Black: void in pore. Yellow: features on the wall of a pore. Green: newly grown hydration products. Blue: convex hull of a pore profile. (c) Average solidity of pores with different pore equivalent diameter

Another pore descriptor is the aspect ratio (A) that can be used to describe the overall pore slenderness. To obtain the aspect ratio of a pore, the pore outline is first fitted with an ellipse, and the A is calculated by dividing the length of the major axis by the minor axis.

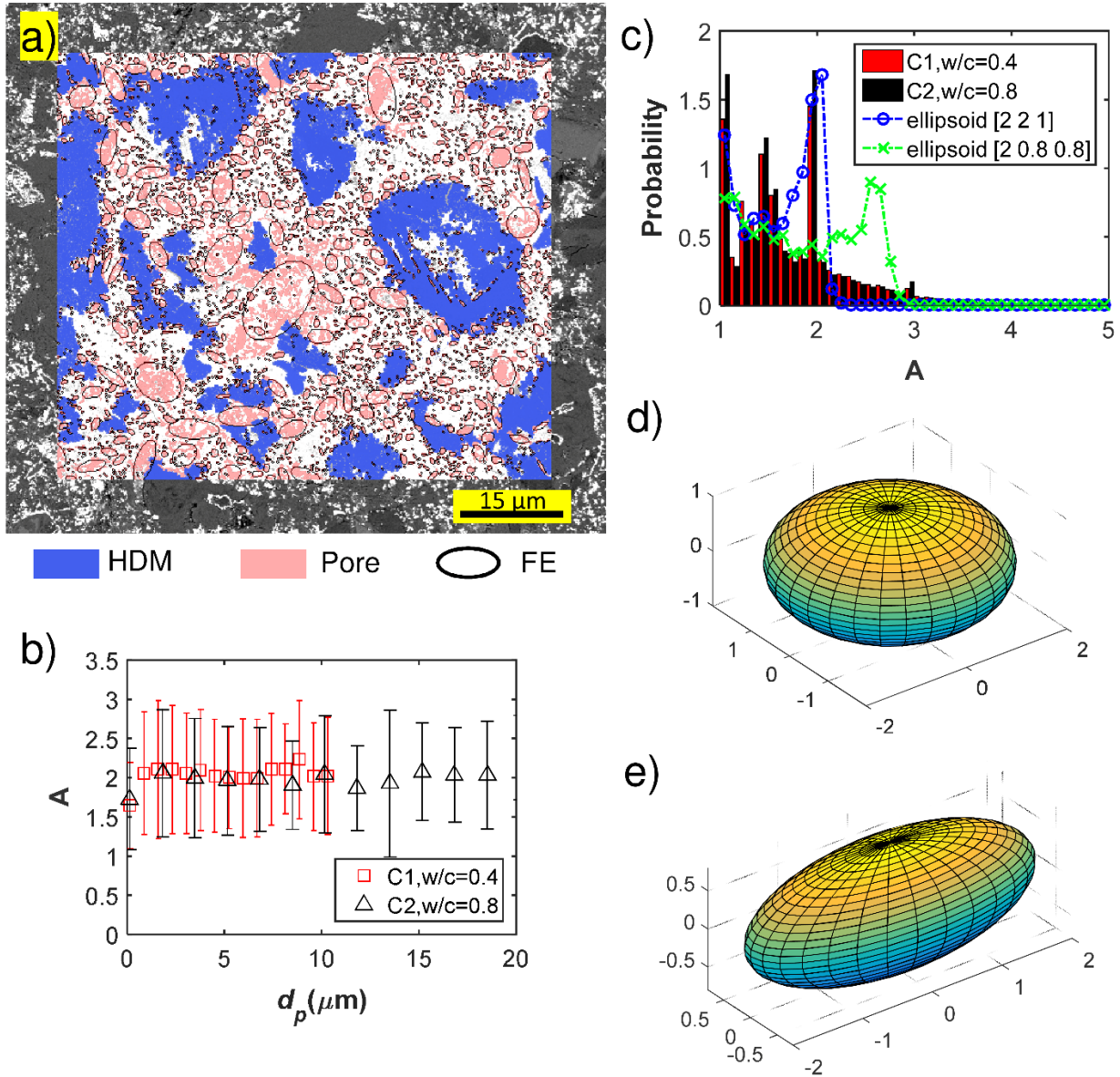


Figure 3-16 (a) Examples of fitted ellipses of pores, average aspect ratio (b) of pores with different pore diameter (d_p), and (c) distribution of aspect ratio and comparison with the probability distribution of A of observed 2D cross sections for d) an oblate ellipsoid (with three radii equal to 2, 2, and 1), and e) a prolate ellipsoid (with three radii equal to 2, 0.8, and 0.8). HDM: high-density material with minimal pores (likely to be unhydrated grains and high-density C-S-H). FE: fitted ellipses.

Figure 3-16a shows the distribution of pores and fitted ellipses around cement grains (indicated by HDM in Figure 3-16a). Figure 3-16b shows that the average aspect ratio of pores in cement paste sample is found to be constant at 2, regardless of the d_p , water to cement ratio, and curing age of the samples. The finding indicates that the hydration product growth and packing of the cement grain demonstrate a preference for a certain aspect ratio. The A - d_p distribution is shown in Figure 3-16c, it

can be seen that the distribution of A is very similar for C1 and C2. This further implies that A is less dependent on the curing age of sample and w/c .

Aspect ratio in 2D BSE images can be linked with 3D pore structures, a characteristic of considerable interest in developing hydration models and the research of pore transport properties [193, 194]. BSE images are 2D observations that record the cross-section information of pores oriented randomly in 3D space. If the overall shape of a pore in 3D is fitted by an ellipsoid, the ellipsoid can have a distribution of aspect ratio for its cross section obtained by slicing the ellipsoid with random planes. In Figure 3-16c, the probability distributions of the aspect ratio calculated from two ellipsoids with different aspect ratio in 3D space are plotted. It can be seen that the ellipsoid with radii 2, 2, and 1 (Figure 3-16d) shows a fair fit with the A distribution when A is smaller than 2. For A larger than 2, a more elongated ellipsoid may need to be introduced, such as that with radii 2, 0.8, and 0.8 shown in Figure 3-16e. These results can be used as an important reference for the development of hydration models [195, 196] in cement science.

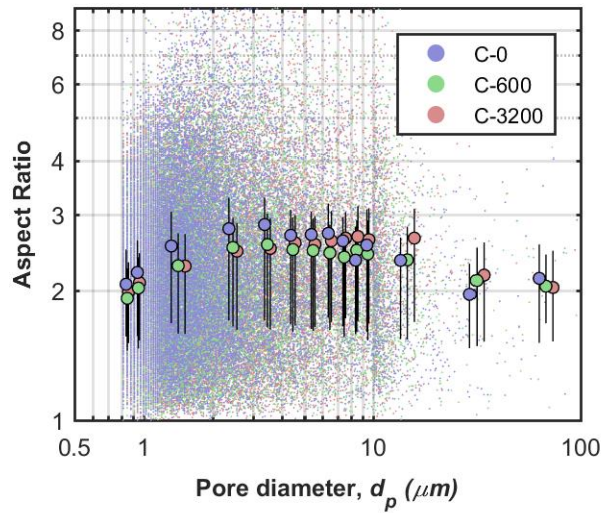


Figure 3-17 A - d_p relationship of soil samples

Figure 3-17 shows the A - d_p distribution of soil samples. A similar pattern displays for the three samples. The aspect ratio of pores with d_p of 1–100 μm ranges from 2.2 to 2.54 and has the average

about 2.4, the difference of A among the three samples being less than 6%. The aspect ratio of pores with d_p small than $1\ \mu\text{m}$ is found to decrease when the pore size decreases. The small difference between the three soil samples indicates that the aspect ratio is minimally dependent on the consolidation pressure.

Because the smaller pores (e.g. $d_p < 10\ \mu\text{m}$) in consolidated silty clay originate from larger pores, by either pore shrinkage in consolidation process or pore collapse, the pressure-independent A - d_p relation of silty clay indicates that the pores in consolidation are likely to be compressed and shrink evenly. The obtained aspect ratio of pores can be used to describe pore slenderness, provide useful information for the engineering properties study of silty clay via e.g. permeability study.

Based on the pore size and pore shape information of soil shown above, Figure 3-18 shows a schematic of the evolution of pore structure in silty clay with increased consolidation pressure. In the consolidation, the aspect ratio of pores is pressure-independent (Figure 3-17). Two stages in the transformation of the consolidation are clearly observed here, namely radial compaction and pore segregation.

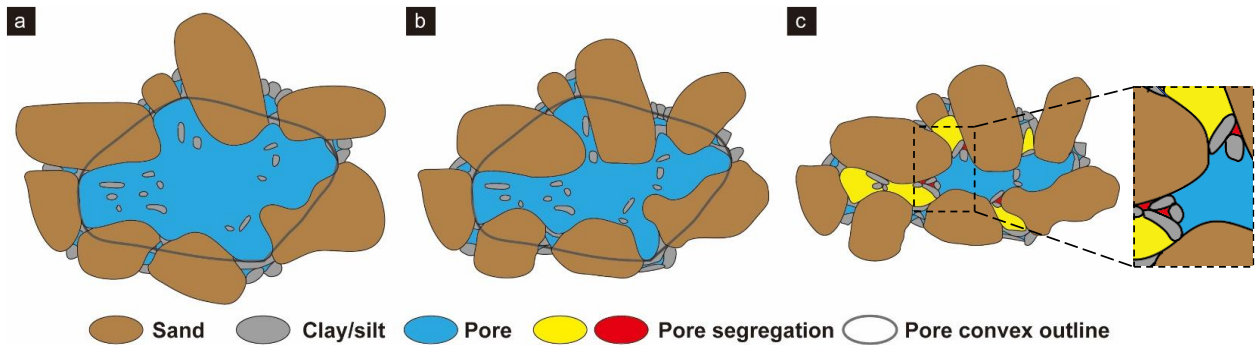


Figure 3-18 Schematics of transform process of pore structure in silty clay under increased consolidation pressure: (a) C-0; (b) C-600; (c) C-3200.

According to the visualized results indicated in Figure 3-6 for silty clay sample does not experience the consolidation, the formation of larger ($d_p > 10\ \mu\text{m}$) pores are dominated by the distribution of sand while smaller ($d_p < 10\ \mu\text{m}$) pores are mainly embedded in clay/silt particles.

When the pressure increases to 600 kPa, the porosity decreases. This is mainly resulted from

shrinkage of larger pores ($d_p > 10 \mu\text{m}$), especially for pore with $d_p > 250 \mu\text{m}$. In this process, the sand particles are mainly compacted radially, in which the pore area is reduced while the pore integrity is preserved. This stage is referred to as “radial compaction”. During this process, the overall shape of the convex area remains less altered as indicated by the similar A - d_p relationship (Figure 3-17) while the solidity is reduced significantly (Figure 3-14). Based on the PSD (Figure 3-12), it can be seen that the PSD for $d_p < 10 \mu\text{m}$ remains close as unconsolidated silty clay sample, indicating the insignificant transformation of the packing of clay/silt particles at this stress level.

As the pressure increased to 3200 kPa, the largest d_p is reduced to be 150 μm . The PSD shows a notable change with a significant increase for smaller pores and decrease for larger pores (Figure 3-12). The transformation of PSD indicates that a portion of larger pores is directly divided into smaller pores ($d_p < 10 \mu\text{m}$), by the separation of agglomerated clay and silt particles. This stage is referred to as “pore segregation”. This is because in the consolidation, lower porosity results in higher effective stress to distribute and agglomerate soil grains including small silt and clay particles. The marginal reduction in pore solidity (Figure 3-14) in pore ranges also indicates that pore-segregation effect is the dominating factor for PSD and volume reduction when pressure increases from 600 to 3200 kPa.

3.6. Conclusion

The pore shape analysis using MI is conducted to correct the biased pore size measurement of MIP by modifying the pore shape assumption of Washburn’s equation. The non-toxic field’s metal is firstly used in metal intrusion technique to address the safety issue of past works.

The MI in combination with BSE imaging was found to be able to produce clear pore images that can effectively be used for computer-based programs while maintain the pore structure integrity of porous silty clay samples. The circularity was used to describe by the area-perimeter relation of pores, which was found to hold a power correlation with d_p . Based on this correlation, the pore shape

assumption of Washburn's equation was modified to give a more accurate reflection of pore size in MIP test. The effectiveness of the modified Washburn's equation was verified experimentally by studying the pore size measurement via MIP.

The solidity and aspect ratio of pores was proposed here to describe the shape information of the pores. The solidity was used to describe the number of features on the pore wall. In cement paste samples, it was found that a low w/c (denser packing of cement particles) and longer hydration time reduced solidity. On the other hand, Solidity in the pores of soil was found to decrease when the consolidation pressure increased, due to the deformation of pores induced by consolidation pressure. Aspect ratio of pores was used to describe the overall pore slenderness or elongation. In 2D observations, it was found that the aspect ratio of pores of cement paste and silty clay has the average value of 2 and 2.4, respectively. The distribution of aspect ratio was used to link the two 2D observation and 3D shape of pores through probability distributions. The ellipsoid with radii 2, 2, and 1 was found to show a fair fit for the pores in the cementitious material. Based on the pore shape information and PSD, a clear two-stage evolution of the pore structure of silty clay in consolidation is proposed.

The study improves the accuracy of the pore size measurement of MIP by incorporating pore shape into the method. The scheme provides a more comprehensive and complete information for the pore analysis of construction materials. In addition to the strong correlation between pore size and properties, the spatial distribution of pores is also a key factor controlling the performance of porous construction materials. Therefore, the analysis of the spatial distribution of pore is the focus of the next chapter (Chapter 4)

CHAPTER 4. DEVIATION FROM WASHBURN'S EQUATION – SPATIAL DISTRIBUTION ANALYSIS OF PORES

4.1. Introduction

Pore structure is a very important characteristic of construction materials because it directly influences the mechanical properties of materials. Although a considerable number of studies have been conducted to predict the strength of porous construction materials using porosity and PSD [197, 198], study of the effect of the spatial distribution of pores on strength is rarely reported. It is known that spatial distribution of pores is one of the key factors that can influence the strength [199] of construction materials. Changes in mechanical properties are observed when the total porosity is held constant and the spatial distribution of pore structure is varied [200].

Spatial distribution of pores is the arrangement of pores in the 3D-space of composites matrix. The ordered or uniform pore structure of synthetic composites at microscale can be processed through templating [201], 3D printing [202], and proper treatment [203, 204] during the composite's processing. However, the pores in most porous construction materials are rarely uniformly distributed. Nonhomogeneously distributed pores can influence the engineering properties of porous construction materials [205-207], especially the possible significant deteriorating effect on the material's mechanical properties. Nonhomogeneously distributed pores in materials reduce the loadbearing area in local regions of the material and can result in lower strength and modulus of elasticity [55]. Clustering of pores, which creates local regions with high pore density, can act as stress concentration sites for fatigue crack initiation and propagation [23, 208].

The spatial distribution of pores is much more difficult to measure and quantify than total porosity. Spatial distribution of pores in construction materials with a wide range of pore sizes cannot be measured by traditional testing methods such as MIP, mainly due to its indirect measurement. On the other hand, the ability of MI to directly measure pores over wide size ranges provides the possibility

of investigating the spatial distribution of pores of construction materials.

Nano-engineered cement composites provide exciting opportunities to improve the performance of cement and have stimulated extensive research interest in the last decade [209, 210]. Among all the nanomaterials applied in cementitious materials, GO has attracted much attention because of its high specific surface area, ultra-high strength and high reinforcing efficiency [211-213]. Studies have investigated the effect of GO on the pore structure and properties of cementitious materials. However, reported studies show large discrepancies in terms of the effect of GO on the porosity of cement paste. Past works have reported different effects of GO on the porosity of cementitious materials, including increasing the porosity [214, 215], significantly reducing the porosity [216, 217], and having no effect on porosity [218]. The large discrepancies in findings could result from the indirect measurement and intrinsic limitation of MIP. Understanding the effect of GO on the porosity of cement composites is key to the study of nano-engineered cement composites. However, no direct measurement based pore analysis of GO-Cement composites, especially the spatial distribution of pores, has been reported.

The foregoing discussion indicates that the spatial distribution of pores could be a primary factor influencing the properties of porous construction materials. There is an emerging need to understand that effect and to further optimize material properties by modifying the spatial distribution of pores. It is necessary to develop a proper analytical method to describe the spatial distribution of pores to address this gap resulting from the indirect measurement of MIP.

This chapter focuses on investigating the spatial distribution of pores in porous construction materials, using the proposed analytical model associated with MI. Two main topics are investigated in this chapter: (1) developing an analytical model based on the radial distribution function (RDF) to study the spatial distribution of pores in construction materials and (2) investigating the spatial distribution of pores and its correlation with mechanical properties of construction materials. The spatial distribution of pores in cementitious materials is observed to follow a clustering pattern and is described using a proposed expression of RDF. The degree of clustering is defined to analyze the

spatial inhomogeneity of pores and its correlation with mechanical properties. To evaluate the effectiveness of the proposed scheme in determining the correlation between the spatial distribution of pores and mechanical properties, a case study is conducted based on the results from reported work.

4.2. Experimental program

4.2.1. MATERIALS AND INSTRUMENTATION

Ordinary Portland cement Type GP (General purpose) conforming to the requirements of Australia Standard AS 3972, was used throughout this study. The GO 4 mg/ml water dispersion was obtained from Graphenea, Inc Spain. The properties of GO are shown in Table 4-1. A polycarboxylic-based superplasticizer (Sika® ViscoCrete® 10) was used to modify the workability of the cement paste. The low-melting-point metal (Field's metal, with melting point 62°C) used for metal intrusion analysis in this study was obtained from Rotometals, Inc.

Table 4-1 Elemental analysis of GO

Element	Carbon	Hydrogen	Nitrogen	Sulphur	Oxygen
%	49-56	0-1	0-1	0-2	41-50

4.2.2. COMPOSITE PROCESSING AND MECHANICAL TESTING

Two mixes of cement paste with the water to cement ratio (w/c) of 0.5 were prepared. One was a plain cement mix as the reference sample (Plain Cement). The other mix incorporated GO with 0.04% by weight of cement powder (GO-Cement). A high-speed shear mixer (CTE Model 7000) was employed for sample mixing. The mixing procedure adopted was similar to ASTM C1738-11 [217].

Immediately after mixing, fresh mixtures were tested by a mini-slump test [219] to determine the workability of the cement pastes. To ensure that different mix batches had similar workability, slightly more superplasticizer was added to the GO-Cement mix to compensate for the loss of workability due to the high surface area of GO. Two cement paste mixes were prepared using this protocol and

their mix design is listed in Table 4-2. In the literature, the dosage of this superplasticizer is in the range of 0.25–1%, for cementitious material [220].

Table 4-2 Mix design

Mix	Water/cement	GO/cement	SP/cement	Mini-slump test
Plain	0.5	0	0	125.5
GO-	0.5	0.04	0.45	123.6

To examine the influence of GO sheets on the mechanical properties of cement paste, compression tests and tensile splitting tests were conducted on cylindrical specimens $\varnothing 23.5 \times 47$ mm. Immediately after mixing, the fresh cement paste were cast into $\varnothing 23.5 \times 47$ mm cylinders and vibrated for approximately 30 s on a vibrating table. The samples were demolded after 24 hours and then cured in saturated lime until mechanical testing. During the preparation process, the room temperature was maintained at 25 ± 1 °C and the humidity was controlled at $50 \pm 5\%$. Mechanical testing was performed using an Instron 4204 50kN loading frame. The loading rate of compression test and tensile splitting test was set to 0.1mm/min and 0.02mm/min, respectively. Three duplicated samples were tested for each mix and the calculated average value was taken as the strength of the cement paste.

4.2.3. SAMPLE PREPARATION AND METAL INTRUSION PROCESS

Cubic samples approximately $5 \text{ mm} \times 5 \text{ mm} \times 5 \text{ mm}$ were taken from the cores of cement paste cylinders. The samples were taken after being cured for 1 day, 7 days, and 28 days, respectively. Ethanol was used to stop hydration after sampling. The cubic samples were reserved in vacuum for one week to remove liquids from the capillary pores. High-pressure (400MPa) MI [33] was used to characterize the microstructure of the cement sample. The detailed procedure was presented in Section 3.2.

4.2.4. BSE IMAGING AND THRESHOLDING

To prevent charging before imaging, each sample's surface was coated with a thin layer (~10nm) of carbon. A Magellan 400 FEGSEM was used to conduct BSE imaging of the samples. For each sample, an area of $\times \mu\text{m}^2$ was scanned with BSE imaging using a low-energy electron (5 keV) and a long electron beam dwell time (10 μs). More than 880,000 pore profiles were observed for each sample.

Intruded pores were identified by thresholding the grey levels of the pores to produce binary images. In the procedure of thresholding, the threshold grey levels used to segregate porosity and solid phases were selected by the technique based on the grey-level histogram of each sample presented in the formal study [33], as described in Section 3.3. The different phases in the BSE images, namely unhydrated grain, hydration products, and pore, in the BSE images were first distinguished by fitting the grey-level histograms with multiple Gaussian distributions. The mean and standard deviation of the Gaussian distributions fitting were obtained by iterations until the R-squared for these fittings was greater than 0.995. The porosity was computed by integration of the Gaussian distributions corresponding to pore over the grey-level domain. An iterative process was then used to obtain the threshold value that produced a consistent volume fraction as the pore phase. The detailed results of Gaussian distribution fitting are shown in Table 4-3.

Table 4-3 Porosity calculated from Gaussian fitting

Sample	Sample	Volume fraction						R square	Porosity
		Cement Matrix			Pore				
1-day Plain cement	Peak BSE intensity	0.178	0.228	0.293	0.491	0.699	0.776	0.9982	0.426
	Percentage (%)	7.53	9.93	15.66	24.23	18.19	24.46		
7-days Plain cement	Peak BSE intensity	0.076	0.169	0.236	0.440	0.734	0.846	0.9964	0.269
	Percentage	2.12	15.99	18.58	36.35	14.79	12.16		
28-days Plain cement	Peak BSE intensity	0.065	0.157	0.225	0.417	0.689	0.817	0.9991	0.217
	Percentage	0.79	24.19	23.02	30.29	15.47	6.24		
1-day GO-Cement	Peak BSE intensity	0.198	0.214	0.282	0.507	0.695	0.760	0.9980	0.351
	Percentage	12.82	11.73	10.17	30.31	21.04	14.30		
7-days GO-Cement	Peak BSE intensity	0.066	0.152	0.209	0.442	0.731	0.834	0.9967	0.222
	Percentage	2.13	15.94	23.63	36.06	13.39	8.85		
28-days GO-Cement	Peak BSE intensity	0.054	0.146	0.239	0.374	0.721	0.843	0.9981	0.187
	Percentage	0.86	33.87	11.56	35.01	17.65	1.05		

The binary images were analyzed using the inbuilt algorithm of the software package, ImageJ. The center of mass of the pore regions was then calculated to derive the coordinate of pores. The coordinate of the pores and the corresponding equivalent pore diameter were used for the analysis of spatial distribution of pores.

4.2.5. MEASUREMENT OF SPATIAL DISTRIBUTION OF PORE

In this study, the spatial distribution of pores was characterized using RDF, which has been widely used in the study of the spatial patterns of objects in many fields [56, 221, 222]. The RDF expressed as $g(r)$ can be interpreted as the ratio of the mean local density determined at the distance r from an arbitrary object to the overall density. In this measurement, there were N pores distributed in a rectangular field of area A . The overall density was given by $\rho = N/A$. The following calculation was adopted to obtain $g(r)$: Calculate the number of all the inter-pore distances and bin them into a histogram. The histogram was then normalized with respect to an ideal gas, where the particle histogram was completed uncorrelated. For two dimensions of the rectangular field, the normalization was the number density (ρ) of pores multiplied by the area of the ring, which was symbolically

expressed as $\rho 2\pi r dr$. The edge effect of the rectangular sampling region was addressed by using the algorithm proposed by Bell [223].

Because the pores obtained by BSE imaging had a wide PSD varying from around $0.1\mu\text{m}$ to several tens of micron meters, pores were categories into different characteristic diameters based on their equivalent pore diameter (d_p) dropped into the region of large capillary pores, which was the pores direct influence on the mechanical properties of cement [224].

4.3. Radial distribution of pores in cementitious materials

The RDF $g(r)$ is defined as “the ratio of the average local number density of a structure at a distance r from a reference structure to the mean density of the structures”, a measurement of spatial pattern commonly used in statistical physics.

The distribution pattern of objects in the system was reflected in different characteristic patterns of $g(r)$. This function has been used in several systems, such as (i) analysis of the pore pattern in porous materials [53, 56]; (ii) spatial distribution of particles and cells in biology [225-228]; (iii) analysis of the distribution of reinforcing particles in composites [229-232].

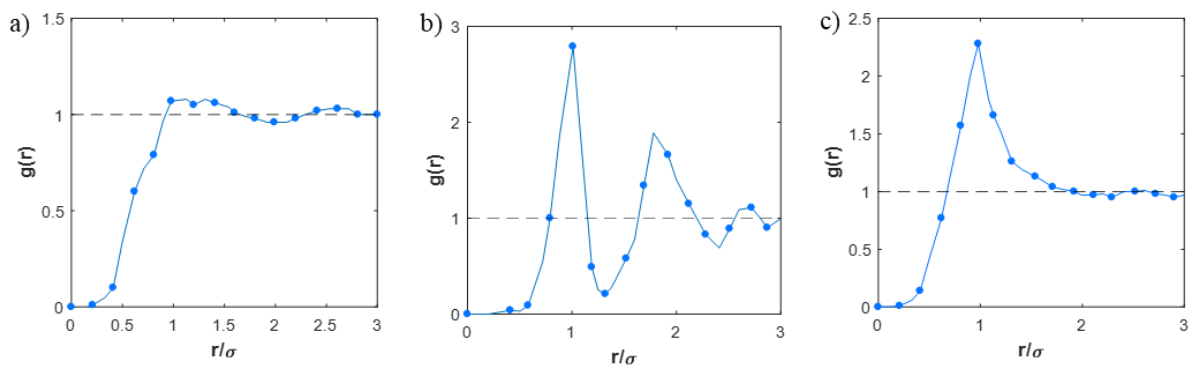


Figure 4-1 Ideal forms of different patterns of $g(r)$: (a) random distribution, (b) substantial order, and (c) clustering distribution.

All patterns of the $g(r)$ had the common feature of rising monotonically from zero at the origin and becoming unity at a large distance. However, three different functional patterns can be obtained

based on the literature [53, 225]. In the first pattern (Figure 4-1 a), the distribution increases monotonically to its asymptotic value equal to the unity. This pattern is distinguished by its relative lack of structure. It represents random distribution of particles where there is no correlation between particles and the particles are uniformly distributed in the system.

The second pattern (Figure 4-1 b) is a substantial order pattern. The distribution of the substantial order pattern shows a strong first maximum and minimum, followed by oscillatory decaying about unity. Such a distribution of $g(r)$ is an indication of order in objects. The degree of ordering of objects is reflected in the amplitude of the maximum and minimum and the rate of decay with the increase in distance to the origin.

The third pattern (Figure 4-1 c) is a clustering pattern, in which there is a strong first peak followed by the damping shape to the unity at a considerable distance. This type of distribution is characteristic of spatial inhomogeneity of particles, in which particles group into clusters that are widely separated. Some clustering distribution [225] produces minor second and third peaks at distances that are roughly multiples of the abscissa of the first peak. However, the amplitudes of these peaks are weak and significantly smaller than that of the first peak. In this type of pattern, the amplitude of the first peak indicates the degree of clustering.

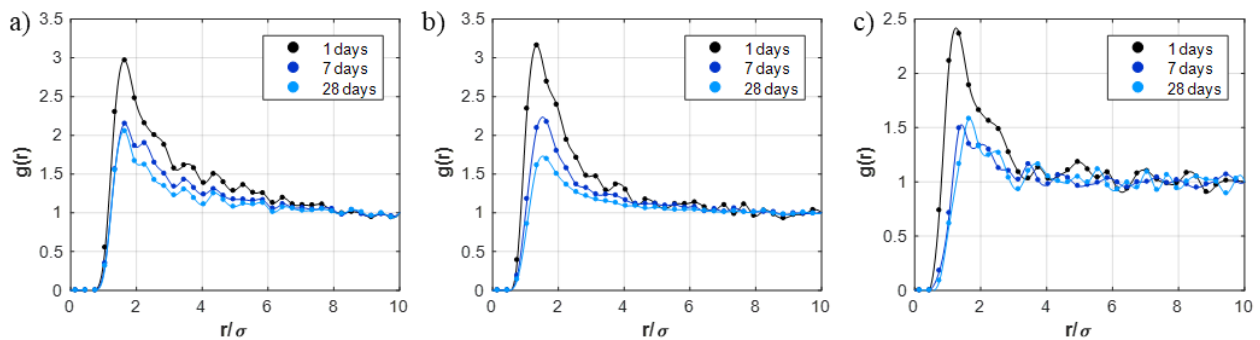


Figure 4-2 RDF of pores with the equivalent diameter of (a) 0.205 μm , (b) 0.815 μm , and (c) 3.246 μm

The typical $g(r)$ of pores in the cement paste is shown in Figure 4-2. The RDF of pores was found to follow a clustering distribution, indicating that spatial inhomogeneity of pores exists in the pore

system of the cement paste. For pores with different characteristic pore diameters (Figure 4-2 a-c), a strong first peak corresponds to the preferable inter-pore distance at the dimensionless distance around 2. All the distribution densities converge to the unity at dimensionless distances less than 8. In pores with a large characteristic size, a weak oscillatory decaying distribution can be observed after the first peak (Figure 4-2 c), where the local maximum is considerably small compared with that of the first strong peak. These features clearly indicate the spatial inhomogeneity of the pores of cement paste.

To describe the RDF $g(r)$ of pores in the cement paste, a mathematical expression is needed to describe the characteristic of the RDF. The radial distribution $g(r)$ of the pores must satisfy the following relations:

At zero inter-pore distance, $g(r)$ must equal zero because the pores cannot overlap.

$$\lim_{r \rightarrow 0} g(r) = 0$$

At large inter-pore distances, $g(r)$ must reduce to unity.

$$\lim_{r \rightarrow \infty} g(r) = 1$$

Furthermore, the equation of the RDF must be continuous over all distances and the first maximum corresponding to the preferable inter-pore distance should occur at the inter-pore distance d , with $d = h \sigma$, where σ is the diameter of the pore, h is the adjustable variable that represents the preferable inter-pore distance in physical space. An oscillatory decaying shape may exist during the decay from the first maximum to the unity.

Considering the features summarized above regarding the general shape of the RDF and the above boundary conditions, the following dimensionless functional form was proposed for the RDF of pores in the cement matrix, through modification of the existing RDF expression in pure fluid study [233]. The expression of the RDF of pores in cementitious materials is shown as:

$$g(x) = g(d) \cdot e^{[\alpha(x-d)]^2}, x < d$$

$$g(x) = 1 + \left[1 - \frac{1}{g(d)}\right] \cdot e^{-\gamma(x-d)} \cdot \mu + (1 - \mu) \cdot \cos[\theta \cdot (x - d)], x \geq d \quad (4-1)$$

where $x = r/\sigma$ is the dimensionless inter-pore distance and $g(d)$, α , d , γ , μ , and θ are adjustable parameters. The term $g(d) \cdot e^{[\alpha(x-d)]^2}$ provides the monotonical increase of the first peak. The term $\left[1 - \frac{1}{g(d)}\right] \cdot g(d) \cdot e^{-\gamma(x-d)}$ provides the decay after the first peak, and the factor $\mu + (1 - \mu) \cdot \cos[\theta \cdot (x - d)]$ gives the oscillatory decaying shape that the RDFs function of pores may display.

By means of a nonlinear least square routine [234], the parameters of Eq. (4-1) were adjusted to produce RDF pores with different characteristic pore diameters over the pore size range of 100nm to 10 μ m, corresponding to the large capillary pores observed in the BSE images. Table 4-4 shows the parameters of self-interaction of pores with different characteristic pore diameters for the 1-day GO-Cement composites. In Table 4-4, pores with sizes varying from 100 nm to 10 μ m are classified into 10 characteristic pores sizes according to their pore diameter range.

Table 4-4 Parameters of the RDF equation of pores for GO-Cement (1 day) determined by nonlinear least square fitting

Pore diameter range classification		g(d)	α	d	γ	μ	θ
Pore diameter range	Characteristic pore diameter (μ m)						
0.100 μ m—0.158 μ m	0.129	3.271	13.289	1.488	0.662	0.863	4.259
0.158 μ m—0.251 μ m	0.205	2.731	4.948	1.573	0.580	0.906	2.205
0.251 μ m—0.398 μ m	0.325	2.913	5.793	1.470	0.616	0.863	2.205
0.398 μ m—0.631 μ m	0.515	2.869	5.009	1.425	0.658	0.919	3.937
0.631 μ m—1.000 μ m	0.815	2.720	4.828	1.425	0.659	0.854	2.205
1.000 μ m—1.585 μ m	1.292	2.631	6.058	1.365	0.871	0.915	2.544
1.585 μ m—2.512 μ m	2.048	2.249	4.007	1.425	0.951	0.907	4.888
2.512 μ m—3.981 μ m	3.246	1.998	7.855	1.309	0.965	1.000	7.194
3.981 μ m—6.310 μ m	5.145	1.839	1.905	1.615	1.675	0.865	5.836
6.310 μ m—10.000 μ m	8.155	1.922	2.073	1.696	0.972	0.636	5.024

As an example, to illustrate the performance of Eq. (4-1), in Figure 4-3 a comparison is shown between experimental RDF points and calculated RDF for two cases.

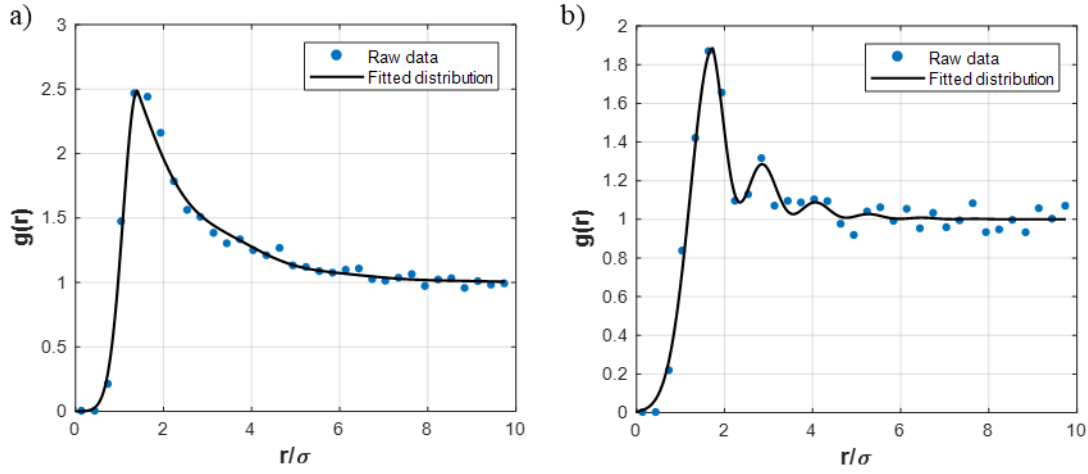


Figure 4-3 Plot of the radial distribution of pores (GO-Cement-1day) and the fitted distribution by the proposed expression with the characteristic diameter of (a) 0.815 μm and (b) 8.155 μm .

To evaluate the goodness of fit of the RDF of pores by the proposed equation, the Kolmogorov-Smirnov test was performed based on the Kolmogorov-Smirnov statistic (d), which is the maximum difference between the cumulative probability functions of the fitted distribution and measured one-dimensional data [235, 236]. The square root of the sample size times the d has a critical value for different levels of significance (from 0.2 to 0.01), above which fitting is rejected [236]. The higher the significance level at which the fitted distribution is not rejected, the better is the fit of the result.

For the 60 RDFs of pores, more than 84% of fitted RDF distributions determined from Eq. (4-1) passed the Kolmogorov-Smirnov test at a 5% significance level. More than 92% of the fitted RDF distributions passed the Kolmogorov-Smirnov test at the significance level of 1%. The Kolmogorov-Smirnov test results showed that the RDF distribution of pores in the cement matrix had a very high likelihood of following the proposed expression [Eq. (4-1)].

4.4. Effect of GO on the spatial distribution of pores in cementitious materials

The RDF of pores presented in previous section shows clearly that the spatial inhomogeneity of pore

exists in the pore system of cement paste. This section investigates the effect of GO on the spatial inhomogeneity of pore and the mechanical properties of cement paste.

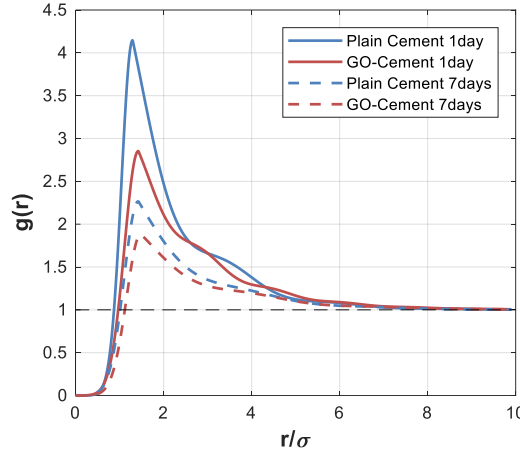


Figure 4-4 Transformation on RDF of pore ($d_p=0.515\mu\text{m}$) with the addition of GO

Figure 4-4 shows the RDF of pore with the characteristic pore diameter of $0.515\mu\text{m}$. At the curing time of 1 day, it can be seen that the $g(r)$ of plain cement shows a sharp peak at the preferable inter-pore peak distance of 1.295. With the addition of GO, the abscissa of the first peak increases to 1.425 and the $g(r)$ corresponding to the first peak decreases from 4.148 to 2.854. The deviation of $g(r)$ from $g(r)=1$ of GO-Cement is reduced, indicating that the addition of GO reduces the degree of clustering of pores in the cement paste. The same situation is also observed for pores at the curing age of 7 days. The $g(r)$ of pores of the GO-Cement shows a pattern closer to that of the random distribution where $g(r)=1$, compared with the RDF of pores of plain cement.

The variation of $g(r)$ describes the spatial inhomogeneity of pore and can be used to quantify the spatial inhomogeneity in the cement matrix. A uniform distribution of pores yields $g(r)=1$ for any dimensionless distance r . On the basis of the fact that the deviation of the $g(r)$ from $g(r)=1$ determines the degree of clustering (δ) of pores [230], δ equals 0 indicates a perfectly uniform distributed pore structure whereas a larger δ indicates a greater spatial inhomogeneity of pores. The δ is given by

$$\delta = \int_d^{\infty} |g(r) - 1| \quad (4-2)$$

where d is the abscissa of the first peak of the RDF, $g(r)$ is the proposed expression of the RDF of pores (Eq. (4-1)). The degree of clustering of pores with different characteristic pore sizes is calculated to produce the relationship of d_p - δ .

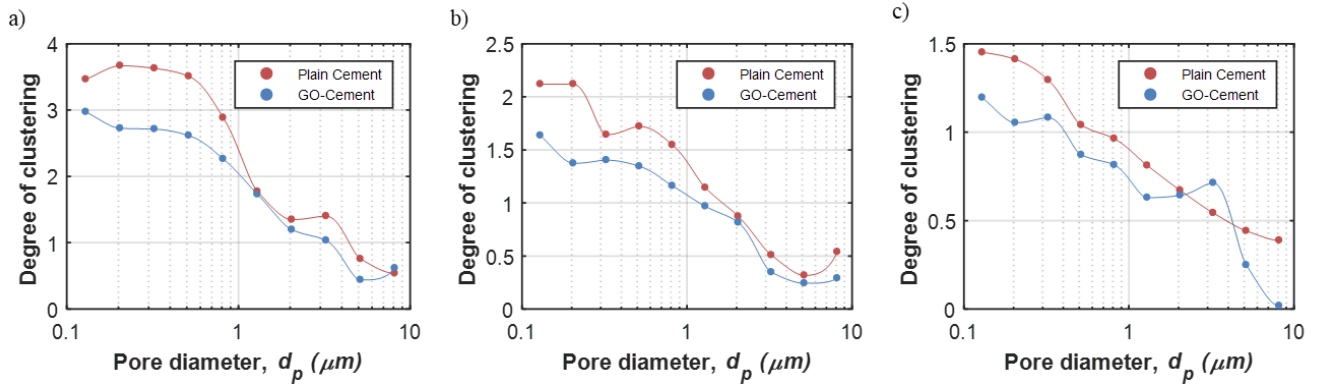


Figure 4-5 Relation of pore diameter and degree of clustering of pores at the curing age of (a) 1 day, (b) 7 days, and (c) 28 days.

Figure 4-5 shows the d_p - δ relationship of pores in cement paste. It can be seen that the addition of GO effectively reduces the overall degree of clustering in samples at all the curing age. Figure 4-6 shows the mean δ of pores at two characteristic size ranges corresponding to the capillary pores observed in the samples. Capillary pores form an interconnected channel resulting from the water-filled spaces present in the hardened paste, the size of such capillary pores ranging from 10nm to 10 μm [10]. Generally, the volume of the capillary pores decreases with time, through the precipitation of hydration products. The large capillary pores ($50\text{nm} < d_p < 10\mu\text{m}$) are important in determining the mechanical properties and permeability of cementitious materials [10, 224]. It can be seen that the GO effectively reduces the degree of clustering of large capillary pores. For the characteristic pore size range of $0.1\mu\text{m} < d_p < 1\mu\text{m}$, GO reduced the δ at 1 day, 7 days, and 28 days by 22.5%, 24.4%, and 18.7% respectively, whereas the δ of the characteristic pore size range from $1\mu\text{m}$ to $10\mu\text{m}$ at 1day, 7 days, and 28 days was reduced by 13.7%, 21.2%, and 21.2%. In general, the δ was reduced

by around 20% for the larger capillary pores. The reduced degree of clustering of pores in the GO-Cement samples indicates that GO could effectively homogenize the spatial distribution of capillary pores in cementitious materials, an effect that is observed for the first time in the pore structure study of the GO-Cement composites.

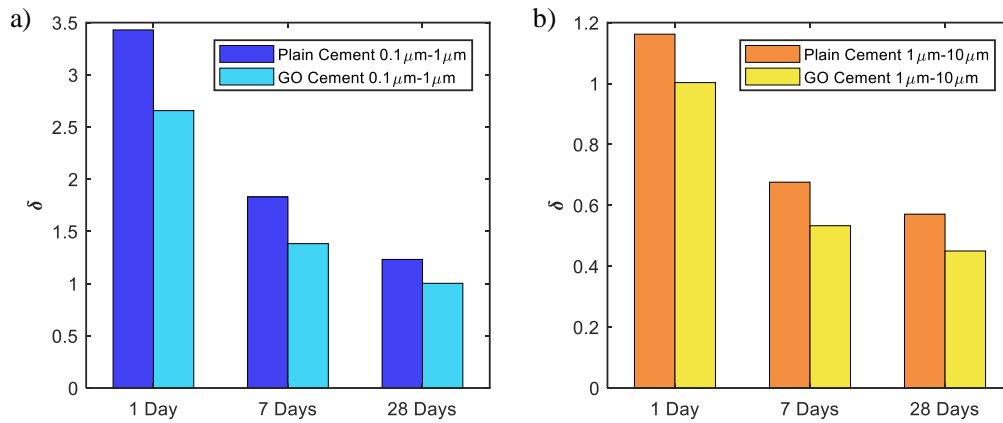


Figure 4-6 Mean degree of clustering of pores with the pore diameter range of (a) 0.1 μm - 1 μm , and (b) 1 μm - 10 μm .

The mechanical properties test was conducted to verify the correlation between the spatial inhomogeneity of pores and the strength of the materials. The compressive strength and splitting tensile strength of cement paste are shown in Figure 4-7. With the addition of GO, the compressive strength at 7 and 28 days is increased by 30.0% and 33.9%, respectively, and the splitting tensile strength is increased by 33.9% and 43.3%, respectively. In contrast, the addition of GO reduced the δ of larger capillary pores at 7 days and 28 days by around 20%. The negative correlation between the compressive/tensile strength and the degree of clustering illustrates that the homogeneous distribution of capillary pores in the matrix is beneficial to the strength of the cementitious materials. The experimental observation and quantitative measurement using the proposed spatial distribution analysis indicate that the spatial homogenization effect of pores achieved by the addition of GO effectively increased the strength performance of the cement composites.

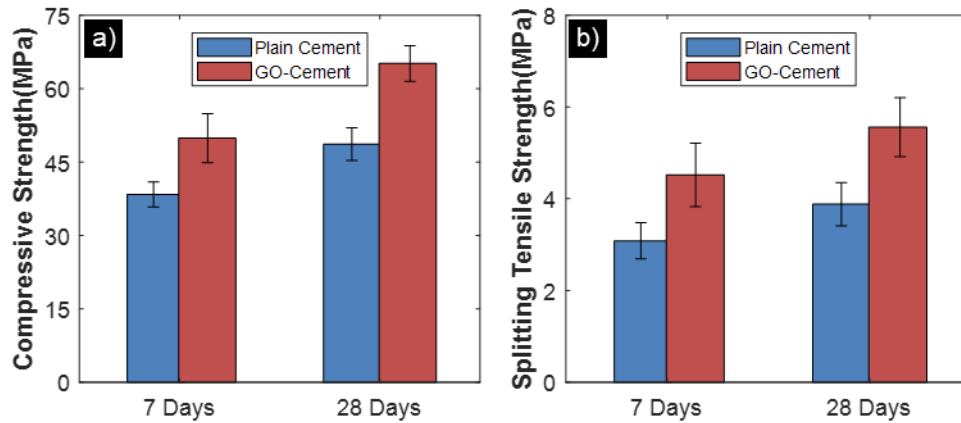


Figure 4-7 (a) Compressive strength and (b) tensile strength of plain cement and GO/cement composites

The experimental observation and quantitative measurement using the spatial distribution analysis proposed here could be used to provide an objective criterion for determining the correlation between the spatial inhomogeneity of pores and the strength of porous construction materials. The effects of reduced spatial inhomogeneity of pores and tensile strength of multi-phase material were studied to verify this correlation, based on relevant literature. All the results presented in this part proceeded using the results presented by Yu et al. [232], who used simulation to investigate the clustering of hollow spheres filled with syntactic foams. Syntactic foams manufactured by filling polymeric matrix with hollow spheres are a kind of lightweight structural materials that have been widely employed in various engineering applications. Hollow spheres made of glass, carbon, ceramics, or polymers can be treated to intentionally induce void space in the polymeric matrix to reduce the density of composites while maintaining moderate mechanical properties [237]. The clustering of hollow spheres is a critical factor in the mechanical performance of syntactic foams [238]. Yu et al studied the tensile properties of constructed microstructures of hollow spheres filled syntactic foams with different clustering patterns, using the finite element method. The degree of clustering of the reinforcing particles was calculated using the RDFs of constructed microstructures presented in the simulation study [232].

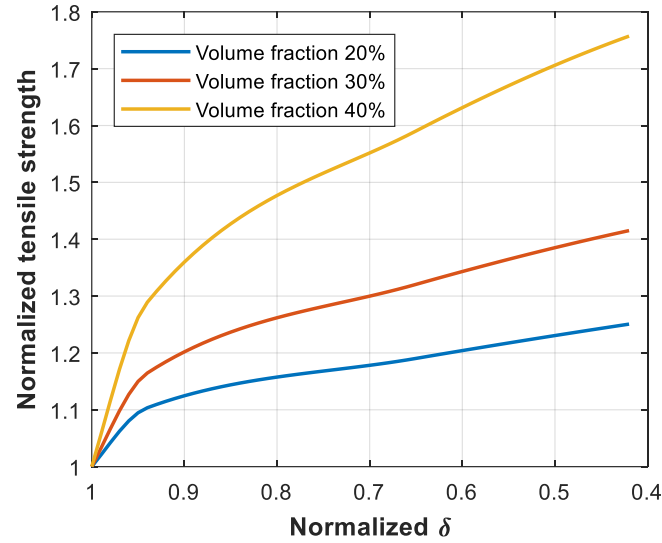


Figure 4-8 Relation between normalized δ and normalized tensile strength (derived from data presented by Yu. et al. [232])

Figure 4-8 shows the relation between the normalized δ and normalized tensile strength of syntactic foam with different volume fractions of hollow spheres, which describe the sensitivity of the tensile strength with respect to the reduced δ . The normalized degree of clustering corresponding to unity equals to 0.9. For all the constructed microstructures with different volume fractions of hollow spheres, the tensile strength shows a negative correlation in relation to the degree of clustering. The result shows that a reduction of δ by 5% leads to a significant improvement of 10% to 25% in tensile strength, depending on the volume fraction of the hollow sphere. When the reduction of δ is greater than 10%, the normalized tensile strength shows an approximately linear relation to the normalized δ . It should be noted that, as the volume fraction of the hollow sphere decreases, the improvement in normalized tensile strength corresponding to the same level of δ reduction is reduced. This observation indicates that the spatial distribution of pores of highly porous materials is one of the dominating factors that control mechanical properties. The proposed spatial analysis method can be used to quantify the inhomogeneity of pores in porous construction materials.

The spatial distribution of pores could be modified to achieve superior performance of porous construction materials. GO was first proved to be able to reduce the spatial inhomogeneity of pores

of cement paste, providing evidence that GO could be used for the future modification of the microstructure of cementitious materials. Other methods, such as use of a surfactant [239] or templating [240, 241], also showed the potential of modifying the spatial distribution of pores of construction materials. The proposed spatial distribution analysis of pores in combination with these methods could improve the engineering properties of cement paste and other construction materials through modification of the spatial distribution of pores. Special attention is needed in this field to develop more reliable structure-properties relationships and to investigate further optimization of porous construction materials.

4.5. Effect of GO on the porosity of cementitious materials

In addition to the spatial distribution of pores, porosity also has an essential link with the properties of materials. The porosity of plain cement matrix and GO-Cement composite at the curing ages of 1, 7, and 28 days is given in Table 4-5. It can be seen that the addition of GO decreases the total porosity of the cement paste. At the curing age of 1 day, the GO-Cement composite has the total porosity of 0.351, which is 17.6% lower than that of its plain cement counterpart. The addition of GO is less effective in reducing the porosity of cement paste at a longer curing age. Compared with the plain cement, the porosity of GO-Cement for the 7- and 28-day samples is reduced by 17.4% and 13.8%, respectively. The reduction in porosity also plays a key role in improving the mechanical properties of cement paste. Reduction in total porosity could be caused by the improved degree of hydration in the GO-Cement samples, as reported in the literature [217].

Table 4-5 Effect of GO on porosity in terms of curing age

	1 day	7 days	28 days
Plain	0.426	0.269	0.217
GO-	0.351	0.222	0.187

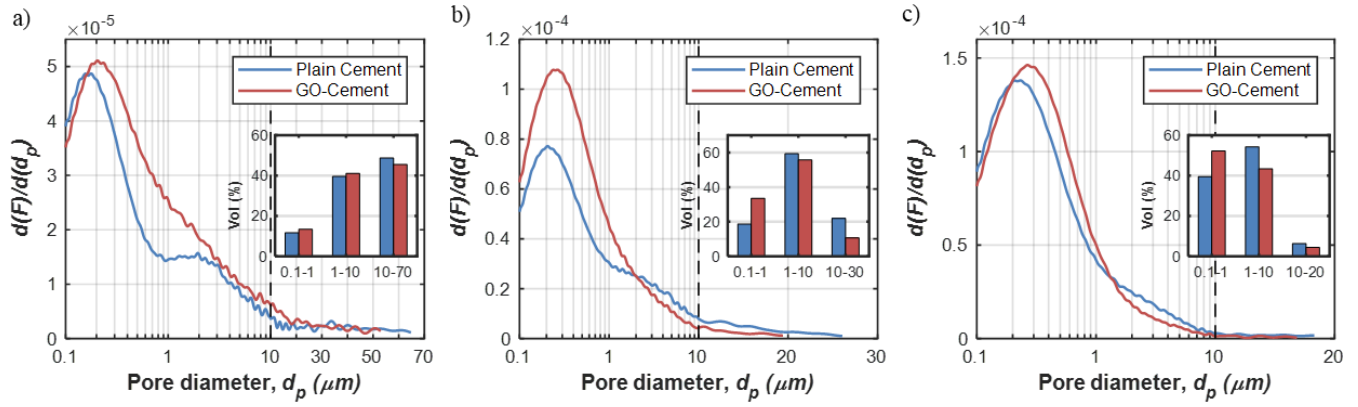


Figure 4-9 PSD for GO-Cement sample cured for (a) 1 day, (b) 7 days, and (c) 28 days.

Figure 4-9 shows the PSDs of the plain cement matrix and GO-Cement composite. The inserted figure shows the pore volume percentage at three characteristic pore diameter ranges. For the 1-day sample (Figure 4-9-a), the PSDs over the pore size range from 2 to 50 μm are similar. However, the addition of GO shows an increased volume percentage of small pores (0.1–1 μm) and reduction of large pores (>10 μm). With the addition of GO, a notable reduction of the maximum pore size can be observed. The maximum pore diameter in the cement matrix is reduced from 65 μm in plain cement to 53 μm in the GO-Cement composite. For the 7-day sample (Figure 4-9-b), it can be seen that the addition of GO significantly increases the number of small pores (0.1 μm –1 μm). Also, with the addition of GO, the volume percentage of pores larger than 10 μm is halved, and the maximum pore diameter is reduced from 27 μm in plain cement to 19 μm . For the 28-day sample (Figure 4-9-b), the PSDs of plain cement and GO-Cement is similar. It is clear, however, that the GO-Cement sample still has the larger volume percentage of small pores and less large pores. The results show that the microstructure refinement effect of GO is clearer with pores greater than 1 μm at the early hydration stage. GO is effective in reducing the size of the largest pore in cement paste. A high volume percentage of small pores is thus an indication that the addition of GO may accelerate the hydration process [215], hence leading to the better strength performance of cement paste.

The evidence presented here that GO could reduce porosity, in combination with the spatial homogenization effect shown in the previous section, indicates that GO can effectively optimize the

pore structure of cementitious material to create a new pore structure with more homogeneously distributed pores and lower porosity. These effects could be key to the process by which GO can significantly improve the engineering properties of cementitious materials.

4.6. Comparison between spatial distribution of pores and Washburn's equation

The MIP test is an indirect method based on Washburn's equation. In the typical procedure of MIP testing, a small dried specimen is evacuated and placed in the porosimeter and mercury is introduced to surround the specimen. Pressure is applied in progressive increments to the non-wetting mercury to force it into the pores, and the intrusion volume of mercury at each pressure step is monitored. The pressure that forces mercury into the pores of the specimen can be converted to pore size using Washburn's equation. The set of pressure steps and corresponding intrusion volumes provides the basic data for calculations of pore size distribution. The pore size distribution obtained from MIP test describes the relative abundance of each pore size. However, the spatial information of pores in the materials cannot be captured by this indirect measurement procedure.

To describe the spatial distribution of pores, the detailed location of individual pores is needed. Metal intrusion techniques produce a direct physical image of the pore structure examined, hence enabling analysis of the spatial distribution of pores. The analytical model proposed can analyze the spatial inhomogeneity of pores in construction materials, thereby extending the limits of Washburn's equation.

The analytical models proposed here provide the possibility for the development of novel and predictive structure-property relationships by intelligent data analysis [242, 243]. Experimental and theoretical evidence shows that the properties of porous construction materials are intrinsically linked to their pore structure [244, 245]. The microstructure of porous construction materials can be conveniently represented by pore structural fingerprints encoding topological and geometrical features. Machine learning algorithms [246] in combination with pore structural fingerprints can be

used to unravel complex structure–property patterns that are too sophisticated to analyze by traditional methods. For example, the traditional models [198, 247, 248] used to predict the strength of porous construction materials focus mainly on porosity. Most of these models break down at zero or high porosities [249]. This limitation could be attributed to the fact that existing models do not consider the spatial distribution of pores.

The RDF has been used to study the structure–properties relationship of many materials. For example, Fernandez et al. [250] used the RDF to predict the gas uptake capacity of a metal-organic framework. The RDF, in combination with machine learning, has been shown to have the ability to recognize the electronic properties of graphene-based materials [251]. The RDF is a suitable structural descriptor in machine learning because it is unambiguous regarding the number of objects and the spatial arrangement of the objects. The low computational cost of using RDF to describe structure also facilitates its application in machine learning. The proposed expression of RDF of pores in cement provides an easy way of describing the spatial distribution of pores, which can be adopted in machine learning. Further study related to this field can increase the accuracy of prediction of the properties of construction materials based on large material databases.

4.7. Conclusion

An analytical model associating MI was proposed to analyze the spatial distribution of pores in construction materials, which can supplement the pore analysis of MIP. The proposed scheme is based on RDF and was applied to investigate the effects of spatial inhomogeneity of pores on the strength of construction materials.

The distribution pattern of large capillary pores in cement paste was found to follow the clustering distribution. A mathematical expression [Eq. (4-1)] was proposed to describe the RDF of pores in cement paste. A descriptor called the degree of clustering [Eq. (4-2)] was defined by calculating the deviation of the RDF from a random distribution in which $g(r)=1$. Based on the proposed analytical model, GO was found to be able to reduce the degree of clustering by around 20% at all curing ages.

The improvement in strength of cement paste with the addition of GO indicated the correlation between the spatial inhomogeneity of pores and mechanical properties. The addition of GO was first proved to improve the pore structure of cement paste by homogenizing the spatial distribution of pores and reducing the porosity, indicating its enormous potential in microstructure modification and strength improvement of cementitious materials.

Because Washburn's equation derived pore information in an indirect way, the arrangement of pores could not be captured. The spatial distribution analysis of pores presented in this study bypasses this limitation of Washburn's equation. It was suggested that the proposed spatial distribution analysis scheme in combination with machine learning could be used for future structure-properties study and prediction in porous construction materials.

The results in this section serve as guidance for analyzing the spatial distribution of pores in construction materials, as well as the supplementary pore analysis for MIP. The experimental results presented up to this point are suited mainly to the analysis of macropores, but the capacity of using metal intrusion to analyze nanopores is still unclear. The next chapter evaluates nanopore analysis of metal intrusion using molecular dynamic simulation.

CHAPTER 5. NANOPORE ANALYSIS VIA METAL INTRUSION USING MOLECULAR DYNAMICS SIMULATION – BEYOND THE LIMITS OF WASHBURN’S EQUATION

5.1. Introduction

Creep and shrinkage behaviors are critical factors in construction engineering because they enable the assessment of the long-term performance of construction materials and the development of life-cycle estimations of the structure [252]. It has been well known that nanopores structure plays a key role in determining the shrinkage [74, 253, 254] and creep [255, 256] behaviors of porous construction materials. Advances in nanoscience and nano-engineered construction materials have also led to an emerging need for nanopore analysis of porous construction materials incorporating nanomaterials [257, 258]. Typical nanomaterials with sizes ranging from 1nm to 20 nm [259, 260] can influence the pore structure at the nanoscale. Analyzing nanopores is essential to study of the long-term behavior of construction materials and further optimization of these materials through nanoengineering.

In recognition of the importance of nanopores, studies have been performed to analyze nanopores in porous construction materials. MIP is the most commonly used technique for pore analysis including nanopores [261-263]. The MIP is based on Washburn’s equation, which describes the force equilibrium of the capillary flow of non-wetting mercury in cylinder pores [264]. According to the inverse relationship between intruded pore size and the pressure applied on mercury, as presented by Washburn’s equation, a pore diameter of 3.6 nm corresponding to the pressure of 400MPa is detectable in the MIP test [265]. However, the MIP is no longer valid in nanopore analysis, because it is the diffusion [162, 266, 267] that dominates the movement of substance in the nanopores rather than the capillary flow [268].

The MI is another pore analysis technique involving the intrusion of non-wetting metal into pores

under high pressure [269]. The metal filled in the pore space can greatly enhance the contrast between pores and solid materials under the microscope, facilitating the direct observation and analysis of pores [270]. Thus it is possible to use MI to detect nanopores or even smaller pores if sufficient pressure can be applied on the liquid metal to force the metal into those pores.

Despite the principle of MI providing the possibility of using this powerful tool to analyze nanopores, the feasibility and interpretation of MI in nanopore analysis are not clear. In particular, past research [12, 15, 16] using MI has mainly used Washburn's equation to estimate the minimum detectable pore size. Hence, investigation of the intrusion of non-wetting metal in nanopores is necessary to promote the future nanopore analysis of construction materials by MI.

This chapter uses molecular dynamics (MD) simulation to evaluate the metal intrusion behavior at the nanoscale and compare the prediction with Washburn's equation. A simulation box consisting of a nanogap structure and mercury atoms located outside the nanogap was established, with the mercury atoms gradually intruding into the nanogap with the increasing pressure in an isothermal process. The relationship between the pressure and intrusion size of metal intrusion in the nanogap is reported. The discrepancy in this pressure-size relationship between simulation and Washburn's equation is studied, based on crystallography. An equation is proposed to predict the extremely high pressure required for the intrusion of non-wetting metal in nanopores.

5.2. Molecular dynamics simulation of nanoporosity

MD simulations were conducted to study the intrusion behavior of mercury in nanogap. The simulation setup is demonstrated in Figure 5-1a. The periodic simulation box (lattice parameter: $a=118$ Å, $b=46.07$ Å, $c=43.0$ Å) consisted of two main components, a graphene-based nanogap structure and the mercury atoms. As pressure is applied to the mercury (Hg) atoms, they were driven into the nanogap. The pressure was achieved by gradually decreasing the length of the simulation box in the z-direction (lattice parameter a). Three layers of graphene (sp^2 hybrid carbon) were used to

form a smooth and naturally curving surface. The graphene layers divided the space into two parts. The first part was accessible to the mercury atoms which acted as the gap for the intrusion, with the gap width varying from 43 Å to 6.5 Å. The second part was enclosed by the graphene sheets and represented non-accessible (closed) pores for the mercury. The existence of these non-accessible pores allowed some deformation of the nanogap structure. In total, 5394 mercury atoms located outside the vacuum nanogap were initially assigned to the lattice to act as the intrusion medium. Geometry optimization and a 10 ps NVT (a constant number of particles, constant volume, and temperature dynamic simulation) ensemble at 300 K were employed to optimize the parameters of the simulation box and relax the system.

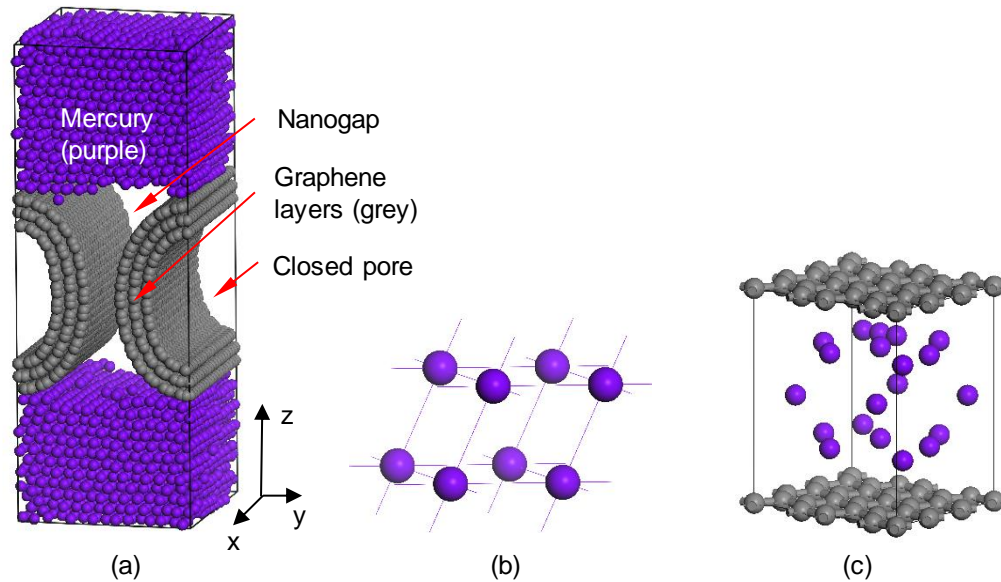


Figure 5-1 (a) Snapshot of the box for intrusion simulation, (b) lattice used for Morse potential parameter calculation of Hg-Hg interaction, (c) system used for Morse potential parameter calculation of Hg-C interaction.

The C-C interaction in the model was described by the Dreiding force field [271] and the Hg-Hg and Hg-C interactions were modeled with Morse potentials [272]. The parameters of Morse potential were determined by fitting the potential energy calculated from first principle calculations using Dmol3 [273]. First principle calculation was performed to compute the relation between systematic energy and size-scaled lattices, PBE functional [274] was used to calculate the force on atoms based

on density functional theory, and DNP [275] was adopted as the basis set. Figure 5-1b and Figure 5-1c show the setup of the first principle calculation. A lattice of mercury (lattice parameters: $a=b=c=3.005\text{\AA}$, $\alpha=\beta=\gamma=70.52^\circ$) at 300K was used to determine the Hg-Hg interaction, and a system ($10.35\text{\AA} \times 8.52\text{\AA} \times 8.52\text{\AA}$) consisting of two layers of graphene (sp²) sandwiching 20 Hg atoms was established for the Hg-C interaction.

Eq. (1) gives the potential energy ($V_{(r)}$) of two atoms separated by a distance R in the form of Morse potential:

$$V_{(r)} = D_0(e^{-2a(R-R_0)} - 2e^{-a(R-R_0)}) \quad (5-1)$$

where R_0 is the equilibrium bond distance of the two atoms, parameters D_0 and a are constants with the dimensions of energy and reciprocal distance, respectively [276]. The potential energy of a lattice composed of multiple atoms is given by the sum Eq. (5-1) over the entire lattice.

To simulate the isothermal (300K) intrusion process, the compression on the simulation box was increased step by step and in each step, the length of the simulation box (Figure 5-1a) in the z -direction (corresponding to lattice parameter a) was reduced by 1\AA , while the dimensions of the simulation box in the other two directions were fixed. After compression in each step, the geometry optimization and twice (timesteps 2 ps and 100 ps respectively) the NVT ensembles at 300 K were employed to optimize the parameters of the lattice and relax the system. For each step, the pressures applied to the atoms were computed by Forcite calculation [277], and the minimum distance between the two surfaces of the nanogap filled with Hg atoms is measured as the intrusion gap width (referred to intrusion size in this study).

Washburn's equation is the classical model used in traditional MIP. The relationship between the pressure and intrusion size was computed by Washburn's equation for comparison with the simulation prediction. To describe this relationship in the form of a gap structure, Washburn's equation was modified and expressed as:

$$D = -\frac{2\gamma\cos\theta}{P} \quad (5-2)$$

where θ is the contact angle of mercury-graphene at room temperature and is taken as 152.5° [278], γ is the surface tension of mercury and is taken as 484mN/m [279], P is the pressure, and D is the size of the intrusion.

5.3. Results and discussion – Nanopores in relation to Washburn's equation

5.3.1. FORCE FIELD PARAMETER

The relationships of systematic energy and size-scaled lattice of Hg-Hg interaction and Hg-C interaction are shown in Figure 5-2. The comparison shows that the first principle and Morse potential calculated results are close. The Morse potential parameters computed from fitting are listed in Table 5-1. To verify the accuracy of the obtained parameters in Morse potential, a Kolmogorov-Smirnov test was performed to determine the goodness of fit using the obtained parameters of the Morse potential. The result shows that the two sets of parameters of Morse potential each pass the test at the significance level of 5%, which means the fitted parameters can accurately present the interatomic potential of Hg-C interaction and Hg-Hg interaction and can be used in the subsequent simulation study of metal intrusion in the nanogap.

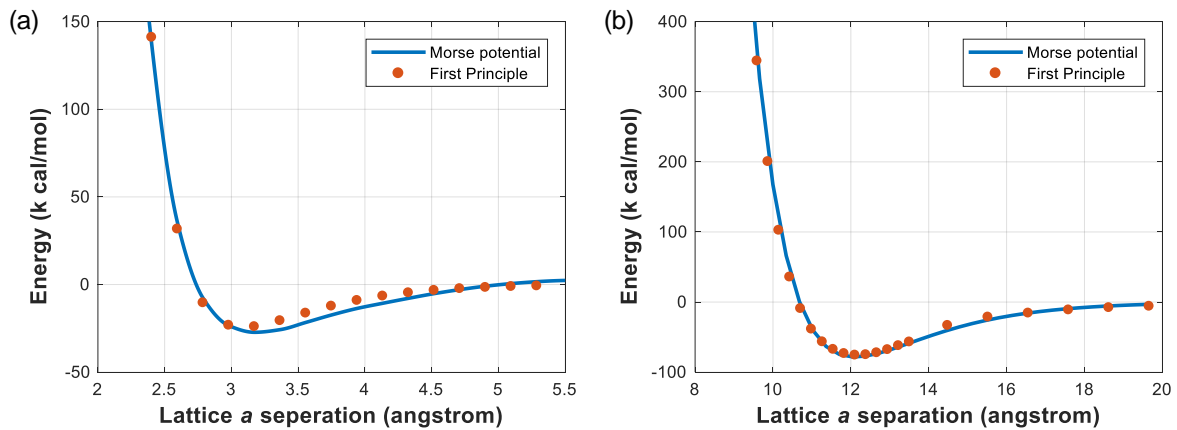


Figure 5-2 Relationship between energy and lattice dimension for: (a) Hg-Hg interaction, (b) Hg-C interaction.

Table 5-1 Morse potential parameters

Category	Functional form	D_0 (kcal/mol)	R_0 (Å)	a
Hg-Hg interaction	Morse	4.6	3.275	11
Hg-C interaction	Morse	0.3	4.15	9.65

5.3.2. PRESSURE AND INTRUSION PROCESS

Figure 5-3 demonstrates the change of atomic structures at different intrusion pressures. As the pressure increases from 308.7 MPa to 6765.8 MPa, the Hg atoms gradually intrude into the narrower gap. Table 5-2 lists the relationship between pressure and intrusion size, where the intrusion size is the minimum distance between two surfaces of the nanogap filled with Hg atoms. As shown in Figure 5-3a, at the pressure of 308.7 MPa, the Hg atoms begin to enter the nanogap following the curve of the graphene surface. When the pressure reaches 6765.8 MPa (Figure 5-3c), the mercury intrudes into the nanogap width of 0.74 nm. It should be noted that when the pressure exceeds 6765.8 MPa (corresponding to the lattice parameter a smaller than 97 Å), significant local buckling of the nanogap structure is observed, as shown in Figure 5-3d. The significant mechanical destruction of the nanogap structure involves alteration of the dimensions of the nanogap as well as extra work done by the pressure due to deformation, which leads to the errors in intrusion size measurement and estimation of pressure. Therefore, the region (lattice length a smaller than 97 Å) in which the significant mechanical destruction of the nanogap structure existed was not considered in this study.

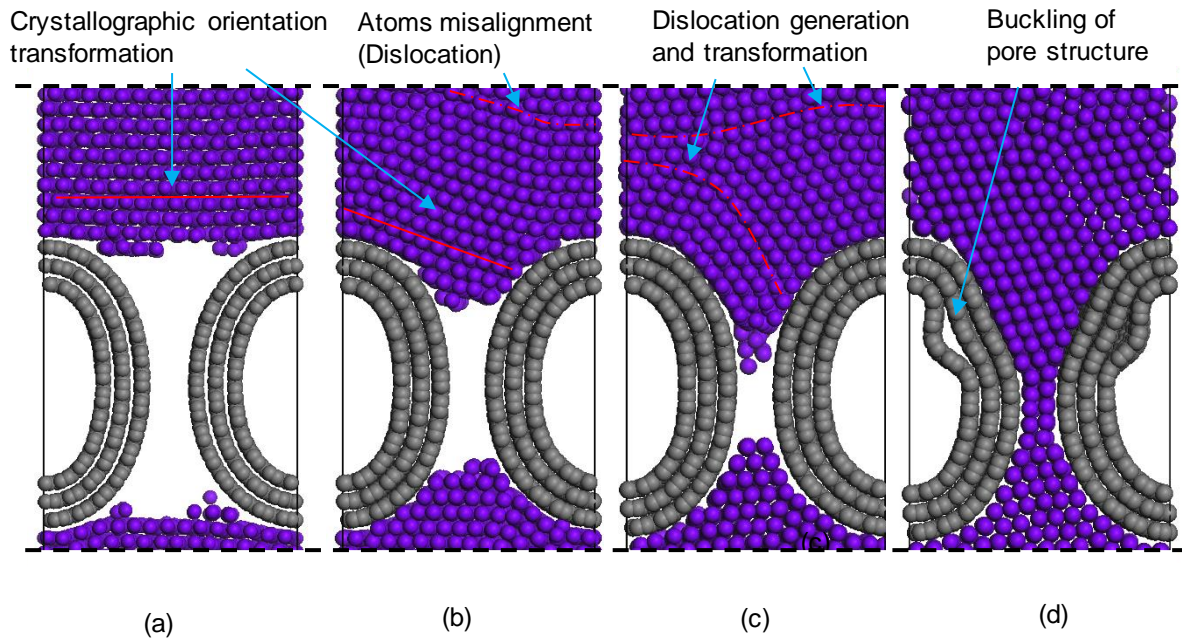


Figure 5-3 Snapshot of metal intrusion at the pressure of: (a) 513.5 MPa, (b) 1776.7 MPa, (c) 6765.8 MPa and (d) Pressure higher than 6765.8 MPa.

Table 5-2 Relationship between pressure and intrusion size

Lattice parameter a (Å)	Pressure (MPa)	Intrusion size (nm)
113	117.0	4.30
112	308.7	3.56
111	513.5	3.19
110	1047.6	2.99
109	1324.7	2.56
108	1092.4	2.35
107	1776.7	2.04
106	2586.8	2.13
105	2373.1	1.68
104	2577.9	1.42
103	2951.5	1.41
102	3119.1	1.11
101	4401.3	1.08
100	4532.0	1.07
99	5606.1	0.91
98	5900.6	0.82
97	6765.8	0.74

In Figure 5-3a, when the pressure equals 308.7 MPa, the mercury atoms align in a certain order that is unlike the disordered packing of mercury atoms under atmospheric pressure [280]. The

densified and ordered atomic packing is likely to be the consequence of pressure [281], where the rhombohedral angle of mercury decreases with increasing hydrostatic compression and continuously distorts towards the face center cubic [282] structure with closer atom packing. When the pressure increases to 1776.7 MPa (Figure 5-3b), it can be seen that the Hg atomic alignment orients at an inclined direction to fit the curvature of the nanogap, which is unlike the packing pattern at lower pressure (308.7 MPa in Figure 5-3a). Densification of atom packing and misalignment of atoms (dislocation) is also observed in Figure 5-3b, possibly indicating the liquid-solid phase transformation of mercury under high pressure. The phase transition for liquid subjected to high pressure is known as Alder transitions [283]. Such transition under high pressure occurs because atoms can only pack closer by transferring from a disordered configuration (liquid) to the ordered (solid) one. The pressure corresponds to the phase transition in the simulation is verified by the experimental result [281], in which the liquid-solid phase transition pressure at 300K equals 1284.5 MPa. More severe misalignment of Hg atoms is observed in Figure 5-3c in which Hg atoms near the gap structure undergo significant distortion to fit the curved boundary of the nanogap. Such generation and transformation of dislocations are also observed in crystals and alloys under extremely high stress [284].

5.3.3. COMPARISON WITH WASHBURN'S EQUATION

Figure 5-4 shows the relationship between pressure and intrusion size obtained from simulation prediction and Washburn's equation. The comparison shows that when the intrusion size is greater than 3 nm, the simulation result manifests the same increasing tendency and generally fits Washburn's equation. When nanogap is smaller than 3nm, however, the relationship between pressure and intrusion size from Washburn's equation begins to deviate from the simulation prediction and the discrepancy between simulation and Washburn's equation increases as the intrusion size decreases.

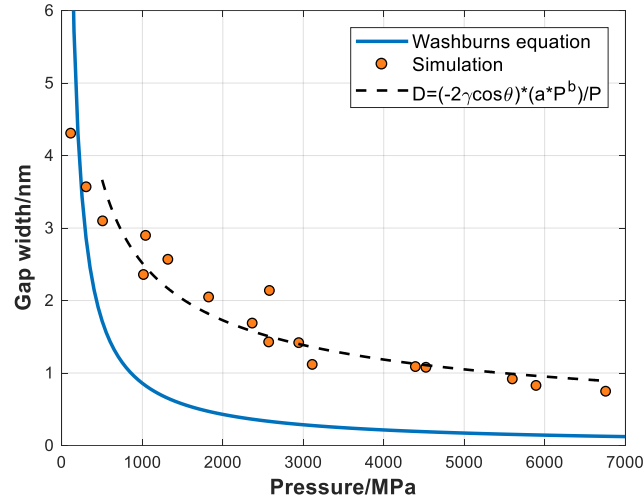


Figure 5-4 Comparison of simulation and Washburn's equation

The generation of internal stresses arising from crystalline deformation and dislocations is considered the reason for the pressure differential between simulation and Washburn's equation. The volume of mercury fluid under high pressure can be greatly compressed. On the basis of a compression experiment of Hg at 295K [285], the volume of mercury could be compressed by 3.1% under the pressure of 1.3GPa. The micro-phenomena corresponding to the volume compression are crystal transformation and densification of atom packing. When the α -mercury is under high pressure, the rhombohedral structure of mercury lattice distorts towards the face center cubic structure, with closer packing (shorter bond length) of atoms [281] and closer packing leads to the increasing repulsive force between mercury atoms. Therefore, the work done by the pressure is partly consumed in the crystalline deformation of Hg. Apart from the pressure consumed by crystalline deformation, Peierls force in the dislocation movement is another reason for this discrepancy. The generation, movement, and transformation of dislocations due to pressure are observed in simulation (Figure 5-3), in which the lattice friction force [286] (Peierls force) that impedes the development and movement of dislocation can compensate for part of the stress induced by pressure. Hence, higher pressure is required to drive Hg atoms into nanoporosity. The discrepancy between the simulation prediction and Washburn's equation indicates that the fluid dynamics model described by Washburn's equation is

no longer valid to be used to describe the movement of substance in nanopores.

To promote future nanopore analysis of metal intrusion, an equation is presented to predict the relationship between pressure and intrusion size in the metal intrusion of nanopores. The equation is expressed as:

$$D = - \frac{2\gamma \cos\theta \cdot a \cdot P^b}{P} \quad (5-3)$$

where θ and γ are the contact angle and surface tension of non-wetting liquid at a certain temperature, P is the pressure, and D is the intruded gap width. The factor $a \cdot P^b$ giving the decaying factor accounts for the higher pressure required to intrude the non-wetting metal into nanopores.

In the model for the use of mercury as the non-wetting liquid to intrude the graphene-based nanogap structure, the parameters a and b in Eq. (5-3) are calculated using the nonlinear least square methods, giving the predicted relation:

$$D = \frac{858.6 \cdot 0.1246 \cdot P^{0.457}}{P} \quad (5-4)$$

the constant 858.6 accounts for the term $-2\gamma \cos\theta$ in Eq. (5-4), which presents the constant contact angle and surface tension of mercury on graphene-based materials at 300K. This modified equation passes the Kolmogorov-Smirnov test at the significance level of 5%, indicating that the equation incorporating simulation prediction can be used to predict the relationship between pressure and intrusion size in the nanopore analysis.

On the basis of that equation, it can be seen that the pressure required for metal intrusion at the nanoscale increases exponentially as the intrusion size decreases. The pressure required for the intrusion size of 1nm predicted by this equation is 5380MPa, which is six times greater than that of Washburn's equation (860MPa), while more than 10 times pressure (19600MPa) is required for the intrusion size of 0.5nm compared with Washburn's equation (1720MPa). This result indicates that

Washburn's equation which describes capillary flow is inapplicable for nanopore analysis. On the other hand, the MI can be used to analyze nanopores, but extremely high pressure is required to intrude a non-wetting metal into nanopores or even smaller pores. Prediction of the pressure required in nanopore analysis by metal intrusion is the key to the future nanopore analysis.

The simulation study of the metal intrusion and the equation presented here serve as guidance for the further nanopore analysis by MI. Special notice needs to be taken to predict the extremely high pressure required for nanopore analysis using MI, especially for nanopores smaller than 3nm.

5.4. Conclusion

The metal intrusion behaviors during the intrusion of mercury into the graphene-based nanogap structure were studied by MD simulations that exceeded the minimum detectable pore size described by the fluid dynamics model of Washburn's equation. The Morse potentials of Hg-Hg and Hg-C interaction were first modeled using first principle calculations.

The relationship between pressure and intrusion size obtained from simulation prediction was compared with the results obtained using Washburn's equation. The comparison showed that Washburn's equation results began to deviate from the simulation prediction when the intrusion size was less than 3nm. The pressure required for metal intrusion at the nanoscale increased exponentially as the intrusion size decreased. These results indicate that Washburn's equation, which is based on capillary flow, is not applicable in nanopore analysis. Crystalline deformation and dislocations were observed in the simulation, which could be the reason for the extremely high pressure required for the intrusion of nanopores.

An equation [Eq. (5-3)] was proposed to predict the extremely high pressure required to force the liquid metal into the nanopores. The scheme presented in this chapter can serve as a starting point for establishing a nanopore analysis method based on MI, which is beneficial to study of the shrinkage and creep of porous construction materials.

CHAPTER 6. CONCLUSIONS AND RECOMMENDATIONS

Although MIP has become the most commonly used pore analysis technique in the construction industry, its assumption and principle restrict its application in analyzing the pore structure of construction materials. Past research studies have reported the significant capabilities and potentials of metal intrusion technique in pore analysis, which shows promise for obtaining more comprehensive pore structure information of construction materials that cannot be achieved by MIP.

In this study, commonly used pore analysis techniques, especially MIP and metal intrusion, are reviewed. The limitations of the use of Washburn's equation in MIP for pore analysis were highlighted. As a further development, the studies presented in this thesis transcend the limitations of MIP using a metal intrusion technique by (i) modifying the theoretical model of the Washburn's equation and (ii) developing and evaluating analytical models for the metal intrusion technique.

6.1. Key research findings

- (1) The pore shape information obtained from MI was used to correct the biased cylindrical pore shape assumption used in Washburn's equation to provide more accurate pore size measurement by MIP. The non-toxic Field's metal was used in the metal intrusion of this work to address the safety issue of past pore analyses using MI. MI in combination with BSE imaging was proved to cause minimal alteration to the pore structure while producing clear pore profile images. Circularity, which describes the area-perimeter relationship of pores in construction materials, was found to have a power correlation with pore size. The noncylindrical pore shape was correlated into Washburn's equation using circularity to yield more accurate pore size measurement by MIP. As an illustration of pore analysis, pore shape data from 2D observations was shown to have a statistical correlation with pore shape in 3D

space. Based on the PSD and pore shape descriptors, the microstructure transformation of cement hydration and consolidation of soil was studied.

(2) Due to the indirect measurement of MIP, there has been very limited research analyzing the spatial information of pores in construction materials. In this study, an analytical model in combination with MI was developed to address this issue. The spatial distribution of pores was analyzed using a proposed analytical model based on RDF. An expression of RDF [Eq. (4-1)] was proposed to describe the spatial distribution of pores in the cement paste. A descriptor called degree of clustering was defined to quantify the spatial inhomogeneity of pores in construction materials. The supporting strength test was conducted to verify the effectiveness of proposed analytical models. GO was first proved able to reduce the spatial inhomogeneity of pores in cement paste, leading to improvement in the mechanical strength of cement paste. The proposed analytical models can be used to establish further study in structure-properties relationships of porous construction materials via machine learning.

(3) Molecular dynamics simulation was conducted to evaluate the feasibility of using metal intrusion to analyze the nanopores, a procedure that is not available for Washburn's equation. The intrusion of mercury atoms into the graphene-based nanogap was studied and compared with Washburn's equation. The pair interaction potential between Hg and C atoms was first determined by first principle calculations for the subsequent simulation. The pressure-gap size relationship observed in the simulation began to deviate from Washburn's equation when the nanogap size was smaller than 3nm. That finding indicated that the fluid dynamics model used in Washburn's equation was inapplicable the nanopore analysis. An equation [Eq. (5-3)] was proposed to predict the high pressure for metal intrusion at the nanoscale, which acts as a starting point for future nanopore analysis by the metal intrusion technique.

6.2. Recommendation for pore analysis of construction materials by MI

Because the capability of MIP to analyze pore structure information is still limited, some of the validated methods associated with MIP and MI presented in this study were recommended and are listed below:

Application of the modified Washburn's equation to provide more accurate pore size measurement based on pore shape:

Washburn's equation can be modified based on the area-perimeter relationship of pores to provide a more accurate measurement of pore size [Eq. (3-9)]. This area-perimeter relationship of different porous construction materials can be determined using the MI.

An analytical model based on MI for analyzing the spatial distribution of pores:

The analytical model using the proposed expression of RDF [Eq. (4-1)] is suggested to quantify the spatial inhomogeneity of pores in construction materials. The details can be found in Chapter 4.

Prediction of the relationship between pressure and intrusion size for metal intrusion at the nanoscale:

A modified equation [Eq. (5-3)] is proposed based on simulation prediction to predict the pressure-size relationship in nanopore analysis by metal intrusion.

6.3. Recommendation for future studies

On the basis of the studies presented in this thesis, some future research direction related to pore analysis and porous construction materials are recommended:

- (1) Using machine learning to develop novel and improved structure-properties relationships of construction materials incorporating spatial information of pores.

- (2) Analyzing the nanopores in porous construction materials by the MI. Using numerical simulation to study and predict the behavior of the intrusion of Field's metal in nanopores to provide the foundation for experimentation.

Based on the limitations of MIP, the future research direction related to the modification of Washburn's equation and MIP is recommended:

- (3) Developing a pore analysis method to address the 'ink-bottle' effect and correct the distorted pore size distribution measurement of MIP.
- (4) Considering changes in the contact angle in MIP to improve the accuracy of test results. Factors that need to be taken into consideration include the composition of the specimen, pore size, drying techniques, surface roughness, and temperature.

REFERENCES

1. Narayanan, N. and K. Ramamurthy, *Structure and properties of aerated concrete: a review*. Cement and Concrete composites, 2000. **22**(5): p. 321-329.
2. Topçu, İ.B. and B. Işıkdag, *Manufacture of high heat conductivity resistant clay bricks containing perlite*. Building and Environment, 2007. **42**(10): p. 3540-3546.
3. Kingery, W.D., *Factors affecting thermal stress resistance of ceramic materials*. Journal of the American Ceramic Society, 1955. **38**(1): p. 3-15.
4. Wang, L., et al., *Heat resistance, crystallization behavior, and mechanical properties of polylactide/nucleating agent composites*. Materials & Design (1980-2015), 2015. **66**: p. 7-15.
5. Tennis, P.D., M.L. Leming, and D.J. Akers, *Pervious concrete pavements*. 2004: Portland Cement Association Skokie, IL.
6. Haselbach, L.M. and R.M. Freeman, *Vertical porosity distributions in pervious concrete pavement*. ACI materials journal, 2006. **103**(6): p. 452.
7. Ferguson, B.K., *Porous pavements*. 2005: CRC Press.
8. Zhang, Z., et al., *Geopolymer foam concrete: An emerging material for sustainable construction*. Construction and Building Materials, 2014. **56**: p. 113-127.
9. Nambiar, E.K. and K. Ramamurthy, *Sorption characteristics of foam concrete*. Cement and concrete research, 2007. **37**(9): p. 1341-1347.
10. Aligizaki, K.K., *Pore structure of cement-based materials: testing, interpretation and requirements*. 2005: CRC Press.
11. Scrivener, K.L. and K.M. Nemati, *The percolation of pore space in the cement paste/aggregate interfacial zone of concrete*. Cement and concrete research, 1996. **26**(1): p. 35-40.
12. Kaufmann, J., *Characterization of Pore Space of Cement-Based Materials by Combined Mercury and Wood's Metal Intrusion*. Journal of the American Ceramic Society, 2009. **92**(1): p. 209-216.
13. Klaver, J., et al., *The connectivity of pore space in mudstones: insights from high-pressure Wood's metal injection, BIB-SEM imaging, and mercury intrusion porosimetry*. Geofluids, 2015. **15**(4): p. 577-591.
14. Lloyd, R.R., et al., *Spatial distribution of pores in fly ash-based inorganic polymer gels visualised by Wood's metal intrusion*. Microporous and Mesoporous Materials, 2009. **126**(1-2): p. 32-39.
15. Willis, K.L., A.B. Abell, and D.A. Lange, *Image-based characterization of cement pore structure using wood's metal intrusion*. Cement and concrete research, 1998. **28**(12): p. 1695-1705.
16. Kaufmann, J., *Pore space analysis of cement-based materials by combined Nitrogen sorption–Wood's metal impregnation and multi-cycle mercury intrusion*. Cement and Concrete Composites, 2010. **32**(7): p. 514-522.
17. Neimark, A.V., P.I. Ravikovitch, and A. Vishnyakov, *Adsorption hysteresis in nanopores*. Physical Review E, 2000. **62**(2): p. R1493.
18. Webb, P.A., *An introduction to the physical characterization of materials by mercury intrusion porosimetry with emphasis on reduction and presentation of experimental data*. Micromeritics Instrument Corp, Norcross, Georgia, 2001.
19. Doyen, P.M., *Permeability, conductivity, and pore geometry of sandstone*. Journal of Geophysical Research: Solid Earth, 1988. **93**(B7): p. 7729-7740.
20. Ninjarav, E., et al., *Pore size distribution of Pusan clay measured by mercury intrusion porosimetry*. KSCE Journal of Civil Engineering, 2007. **11**(3): p. 133-139.
21. Durner, W., *Hydraulic conductivity estimation for soils with heterogeneous pore structure*. Water Resources Research, 1994. **30**(2): p. 211-223.
22. Tang, X., et al., *The effect of the variation in material composition on the heterogeneous pore structure of high-maturity shale of the Silurian Longmaxi formation in the southeastern Sichuan Basin, China*. Journal of Natural Gas Science and Engineering, 2015. **23**: p. 464-473.
23. Xu, Z., W. Wen, and T. Zhai, *Effects of pore position in depth on stress/strain concentration and fatigue crack initiation*. Metallurgical and Materials Transactions A, 2012. **43**(8): p. 2763-2770.
24. Gajewicz, A., et al., *A ¹H NMR relaxometry investigation of gel-pore drying shrinkage in cement pastes*. Cement and Concrete Research, 2016. **86**: p. 12-19.
25. Bažant, Z., et al., *Interaction of concrete creep, shrinkage and swelling with water, hydration, and damage: Nano-Macro-Chemo*, in *CONCREEP 10*. 2015. p. 1-12.
26. Fisher, L.R. and P.D. Lark, *An experimental study of the Washburn equation for liquid flow in very fine capillaries*. Journal of Colloid and Interface Science, 1979. **69**(3): p. 486-492.
27. Shaikh, K.A. and C. Liu, *A bi-stable latchable pdms valve employing low melting temperature metal alloys*. in *Solid-State Sensors, Actuators and Microsystems Conference, 2007. TRANSDUCERS 2007. International*. 2007. IEEE.

28. Rootare, H. and A. Nyce, *Use of porosimetry in the measurement of pore size distribution in porous materials*. Int. J. Powder Met, 1971. **7**.
29. Jenkins, R. and M. Rao, *The effect of elliptical pores on mercury porosimetry results*. Powder technology, 1984. **38**(2): p. 177-180.
30. Cook, R.A. and K.C. Hover, *Mercury porosimetry of cement-based materials and associated correction factors*. Construction and Building Materials, 1993. **7**(4): p. 231-240.
31. Rice, R.W., *Porosity of ceramics: Properties and applications*. 1998: CRC Press.
32. Chen, S.J., et al., *Pore shape analysis using centrifuge driven metal intrusion: Indication on porosimetry equations, hydration and packing*. Construction and Building Materials, 2017. **154**: p. 95-104.
33. Hu, Y., et al., *Transformation of pore structure in consolidated silty clay: New insights from quantitative pore profile analysis*. Construction and Building Materials, 2018. **186**: p. 615-625.
34. Duggal, S.K., *Building materials*. 2017: Routledge.
35. Neithalath, N., M.S. Sumanasooriya, and O. Deo, *Characterizing pore volume, sizes, and connectivity in pervious concretes for permeability prediction*. Materials characterization, 2010. **61**(8): p. 802-813.
36. Green, K., et al., *A high pressure permeameter for the measurement of liquid conductivity of porous construction materials*. Review of scientific instruments, 1999. **70**(8): p. 3397-3401.
37. Al-Raoush, R., *Microstructure characterization of granular materials*. Physica A: Statistical mechanics and its Applications, 2007. **377**(2): p. 545-558.
38. Cnudde, V., et al., *Porosity and microstructure characterization of building stones and concretes*. Engineering geology, 2009. **103**(3-4): p. 76-83.
39. Schmitt, M., et al., *Characterization of pore systems in seal rocks using nitrogen gas adsorption combined with mercury injection capillary pressure techniques*. Marine and Petroleum Geology, 2013. **39**(1): p. 138-149.
40. Ait-Mokhtar, A., et al., *Porous Construction Materials: Characterizations and Modeling*. Structure Design and Degradation Mechanisms in Coastal Environments, 2015: p. 1-39.
41. Giesche, H., *Mercury porosimetry: a general (practical) overview*. Particle & particle systems characterization, 2006. **23**(1): p. 9-19.
42. Groen, J.C., L.A. Peffer, and J. Pérez-Ramírez, *Pore size determination in modified micro-and mesoporous materials. Pitfalls and limitations in gas adsorption data analysis*. Microporous and mesoporous materials, 2003. **60**(1-3): p. 1-17.
43. Diamond, S., *Mercury porosimetry: an inappropriate method for the measurement of pore size distributions in cement-based materials*. Cement and concrete research, 2000. **30**(10): p. 1517-1525.
44. Hellmuth, K.H., M. Siitari-Kauppi, and A. Lindberg, *Study of porosity and migration pathways in crystalline rock by impregnation with 14C-polymethylmethacrylate*. Journal of Contaminant Hydrology, 1993. **13**(1): p. 403-418.
45. Chen, J., D. Zampini, and A. Walliser, *High-pressure epoxy-impregnated cementitious materials for microstructure characterization*. Cement and concrete research, 2002. **32**(1): p. 1-7.
46. Brace, W., *Permeability from resistivity and pore shape*. Journal of Geophysical Research, 1977. **82**(23): p. 3343-3349.
47. Chen, W.T., *Stress concentration around spheroidal inclusions and cavities in a transversely isotropic material under pure shear*. Journal of Applied Mechanics, 1970. **37**(1): p. 85-92.
48. Savin, G.N., *Stress concentration around holes*. 1961.
49. Moro, F. and H. Böhni, *Ink-bottle effect in mercury intrusion porosimetry of cement-based materials*. Journal of Colloid and Interface Science, 2002. **246**(1): p. 135-149.
50. Stone, I. and P. Tsakirooulos, *Characterisation of spatial distribution of reinforcement in powder metallurgy route Al/SiCp metal matrix composites*. Materials science and technology, 1995. **11**(3): p. 213-221.
51. Aligizaki, K.K., *Pore structure of cement-based materials: testing, interpretation and requirements*. 2014: CRC Press.
52. Johnson, S.A., P.J. Ollivier, and T.E. Mallouk, *Ordered Mesoporous Polymers of Tunable Pore Size from Colloidal Silica Templates*. Science, 1999. **283**(5404): p. 963-965.
53. Markovics, J., L. Glass, and G.G. Maul, *Pore patterns on nuclear membranes*. Experimental cell research, 1974. **85**(2): p. 443-451.
54. Schoof, H., et al., *Control of pore structure and size in freeze-dried collagen sponges*. Journal of Biomedical Materials Research, 2001. **58**(4): p. 352-357.
55. Dorey, R.A., J.A. Yeomans, and P.A. Smith, *Effect of pore clustering on the mechanical properties of ceramics*. Journal of the European Ceramic Society, 2002. **22**(4): p. 403-409.
56. Imhof, A. and D. Pine, *Ordered macroporous materials by emulsion templating*. Nature, 1997. **389**(6654): p. 948.
57. Tanjidi, E. and A. Simchi, *Fabrication of a highly ordered hierarchically designed porous nanocomposite via indirect 3D printing: Mechanical properties and in vitro cell responses*. Materials & Design, 2015. **88**: p. 924-931.
58. Staiger, M.P., et al., *Synthesis of topologically-ordered open-cell porous magnesium*. Materials Letters, 2010. **64**(23): p. 2572-2574.

59. Bindumadhavan, P.N., et al., *Effect of particle-porosity clusters on tribological behavior of cast aluminum alloy A356-SiCp metal matrix composites*. Materials Science and Engineering: A, 2001. **315**(1): p. 217-226.
60. Knackstedt, M.A., A.P. Sheppard, and M. Sahimi, *Pore network modelling of two-phase flow in porous rock: the effect of correlated heterogeneity*. Advances in Water Resources, 2001. **24**(3): p. 257-277.
61. Bilger, N., et al., *Effect of a nonuniform distribution of voids on the plastic response of voided materials: a computational and statistical analysis*. International Journal of Solids and Structures, 2005. **42**(2): p. 517-538.
62. Shang-lin, Y., et al. *Multi-fractal Fractal Characteristics of the Heterogeneous Pore Distribution of Cores*. in *2012 International Conference on Computer Distributed Control and Intelligent Environmental Monitoring*. 2012.
63. Gibson, R.E., G.L. England, and M.J.L. Hussey, *The Theory of One-Dimensional Consolidation of Saturated Clays*. Géotechnique, 1967. **17**(3): p. 261-273.
64. Choi, S.-W., Y. Zhang, and Y. Xia, *Three-Dimensional Scaffolds for Tissue Engineering: The Importance of Uniformity in Pore Size and Structure*. Langmuir, 2010. **26**(24): p. 19001-19006.
65. Danninger, H., et al., *Microstructure and mechanical properties of sintered iron. Pt. 1; Basic considerations and review of literature*. 1993.
66. Fan, J., et al., *Cyclic plasticity at pores and inclusions in cast Al-Si alloys*. Engineering Fracture Mechanics, 2003. **70**(10): p. 1281-1302.
67. Bird, N., et al., *Fractal and multifractal analysis of pore-scale images of soil*. Journal of hydrology, 2006. **322**(1): p. 211-219.
68. Dathe, A., et al., *The surface fractal dimension of the soil-pore interface as measured by image analysis*. Geoderma, 2001. **103**(1): p. 203-229.
69. Lipiec, J., R. Hatano, and A. Słowińska-Jurkiewicz, *The fractal dimension of pore distribution patterns in variously-compacted soil*. Soil and Tillage Research, 1998. **47**(1): p. 61-66.
70. Romm, F., *Microporous media: synthesis, properties, and modeling*. Vol. 120. 2004: CRC Press.
71. Everett, D., *Manual of symbols and terminology for physicochemical quantities and units, appendix II: Definitions, terminology and symbols in colloid and surface chemistry*. Pure and Applied Chemistry, 1972. **31**(4): p. 577-638.
72. Lamond, J.F. and J.H. Pielert. *Significance of tests and properties of concrete and concrete-making materials*. 2006. ASTM West Conshohocken, PA.
73. Shimomura, T. and K. Maekawa, *Analysis of the drying shrinkage behaviour of concrete using a micromechanical model based on the micropore structure of concrete*. Magazine of Concrete Research, 1997. **49**(181): p. 303-322.
74. Ziembicka, H., *Effect of micropore structure on cellular concrete shrinkage*. cement and concrete research, 1977. **7**(3): p. 323-332.
75. Bažant, Z.P., et al., *Microprestress-solidification theory for concrete creep. I: Aging and drying effects*. Journal of Engineering Mechanics, 1997. **123**(11): p. 1188-1194.
76. Aligizaki, K.K., *Determination of pore structure parameters in hardened cementitious materials*. MS Thesis. The Pennsylvania State University, 1995.
77. Taylor, H.F., *Proposed structure for calcium silicate hydrate gel*. Journal of the American Ceramic Society, 1986. **69**(6): p. 464-467.
78. Dubinin, M., *The potential theory of adsorption of gases and vapors for adsorbents with energetically nonuniform surfaces*. Chemical Reviews, 1960. **60**(2): p. 235-241.
79. Haynes, J., *Determination of pore properties of constructional and other materials*. Matériaux et Construction, 1973. **6**(3): p. 169-174.
80. Vafai, K., *Handbook of porous media*. 2015: Crc Press.
81. Ma, H., *Mercury intrusion porosimetry in concrete technology: tips in measurement, pore structure parameter acquisition and application*. Journal of porous materials, 2014. **21**(2): p. 207-215.
82. Kaufmann, J., R. Loser, and A. Leemann, *Analysis of cement-bonded materials by multi-cycle mercury intrusion and nitrogen sorption*. Journal of Colloid and Interface Science, 2009. **336**(2): p. 730-737.
83. Van Brakel, J., S. Modrý, and M. Svata, *Mercury porosimetry: state of the art*. Powder technology, 1981. **29**(1): p. 1-12.
84. Zhou, J., G. Ye, and K. Van Breugel, *Characterization of pore structure in cement-based materials using pressurization-depressurization cycling mercury intrusion porosimetry (PDC-MIP)*. Cement and Concrete Research, 2010. **40**(7): p. 1120-1128.
85. De With, G. and H. Glass, *Reliability and reproducibility of mercury intrusion porosimetry*. Journal of the European Ceramic Society, 1997. **17**(6): p. 753-757.
86. Gao, Z. and Q. Hu, *Estimating permeability using median pore-throat radius obtained from mercury intrusion porosimetry*. Journal of Geophysics and Engineering, 2013. **10**(2): p. 025014.
87. Romero, E. and P.H. Simms, *Microstructure investigation in unsaturated soils: a review with special attention to contribution of mercury intrusion porosimetry and environmental scanning electron microscopy*. Geotechnical and Geological Engineering, 2008. **26**(6): p. 705-727.

88. Simms, P.H. and E.K. Yanful, *A discussion of the application of mercury intrusion porosimetry for the investigation of soils, including an evaluation of its use to estimate volume change in compacted clayey soils*. Géotechnique, 2004. **54**(6): p. 421-426.
89. Lapierre, C., S. Leroueil, and J. Locat, *Mercury intrusion and permeability of Louiseville clay*. Canadian Geotechnical Journal, 1990. **27**(6): p. 761-773.
90. Sasanian, S. and T. Newson, *Use of mercury intrusion porosimetry for microstructural investigation of reconstituted clays at high water contents*. Engineering Geology, 2013. **158**: p. 15-22.
91. Yao, Y. and D. Liu, *Comparison of low-field NMR and mercury intrusion porosimetry in characterizing pore size distributions of coals*. Fuel, 2012. **95**: p. 152-158.
92. Rice, R.W., *Comparison of stress concentration versus minimum solid area based mechanical property-porosity relations*. Journal of Materials Science, 1993. **28**(8): p. 2187-2190.
93. Rice, R., *Limitations of pore-stress concentrations on the mechanical properties of porous materials*. Journal of Materials Science, 1997. **32**(17): p. 4731-4736.
94. Kumar, M. and D.-h. Han, *Pore shape effect on elastic properties of carbonate rocks*, in *SEG Technical Program Expanded Abstracts 2005*. 2005, Society of Exploration Geophysicists. p. 1477-1480.
95. Zeng, Q., et al., *Analysis of pore structure, contact angle and pore entrapment of blended cement pastes from mercury porosimetry data*. Cement and Concrete Composites, 2012. **34**(9): p. 1053-1060.
96. Penumadu, D. and J. Dean, *Compressibility effect in evaluating the pore-size distribution of kaolin clay using mercury intrusion porosimetry*. Canadian Geotechnical Journal, 2000. **37**(2): p. 393-405.
97. Adolphs, J., M. Setzer, and P. Heine, *Changes in pore structure and mercury contact angle of hardened cement paste depending on relative humidity*. Materials and Structures, 2002. **35**(8): p. 477-486.
98. Good, R.J. and R.S. Mikhail, *The contact angle in mercury intrusion porosimetry*. Powder Technology, 1981. **29**(1): p. 53-62.
99. Shi, D. and D.N. Winslow, *Contact angle and damage during mercury intrusion into cement paste*. Cement and Concrete Research, 1985. **15**(4): p. 645-654.
100. Randall, P. and S. Chattopadhyay, *Advances in encapsulation technologies for the management of mercury-contaminated hazardous wastes*. Journal of hazardous materials, 2004. **114**(1-3): p. 211-223.
101. Sing, K., *The use of nitrogen adsorption for the characterisation of porous materials*. Colloids and Surfaces A: Physicochemical and Engineering Aspects, 2001. **187**: p. 3-9.
102. Kruk, M. and M. Jaroniec, *Gas adsorption characterization of ordered organic-inorganic nanocomposite materials*. Chemistry of materials, 2001. **13**(10): p. 3169-3183.
103. Rouquerol, J., et al., *Adsorption by powders and porous solids: principles, methodology and applications*. 2013: Academic press.
104. Barrett, E.P., L.G. Joyner, and P.P. Halenda, *The determination of pore volume and area distributions in porous substances. I. Computations from nitrogen isotherms*. Journal of the American Chemical society, 1951. **73**(1): p. 373-380.
105. Walton, K.S. and R.Q. Snurr, *Applicability of the BET method for determining surface areas of microporous metal-organic frameworks*. Journal of the American Chemical Society, 2007. **129**(27): p. 8552-8556.
106. Clarkson, C.R., et al., *Pore structure characterization of North American shale gas reservoirs using USANS/SANS, gas adsorption, and mercury intrusion*. Fuel, 2013. **103**: p. 606-616.
107. Okolo, G.N., et al., *Comparing the porosity and surface areas of coal as measured by gas adsorption, mercury intrusion and SAXS techniques*. Fuel, 2015. **141**: p. 293-304.
108. Mastalerz, M., et al., *Porosity of Devonian and Mississippian New Albany Shale across a maturation gradient: Insights from organic petrology, gas adsorption, and mercury intrusion*. AAPG bulletin, 2013. **97**(10): p. 1621-1643.
109. Jaroniec, M., M. Kruk, and J.P. Olivier, *Standard nitrogen adsorption data for characterization of nanoporous silicas*. Langmuir, 1999. **15**(16): p. 5410-5413.
110. Jaroniec, M. and R. Madey, *Physical adsorption on heterogeneous solids*. Vol. 59. 1988: Elsevier Amsterdam.
111. Jaroniec, M. and J. Choma, *Theory of gas adsorption on structurally heterogeneous solids and its application for characterizing activated carbons*. Chemistry and physics of carbon: New York, Marcel Dekker, Inc, 1989. **22**: p. 197-243.
112. Iassonov, P., T. Gebrenegus, and M. Tuller, *Segmentation of X-ray computed tomography images of porous materials: A crucial step for characterization and quantitative analysis of pore structures*. Water Resources Research, 2009. **45**(9).
113. Alaoui, A., J. Lipiec, and H. Gerke, *A review of the changes in the soil pore system due to soil deformation: A hydrodynamic perspective*. Soil and Tillage Research, 2011. **115**: p. 1-15.
114. Wang, Y.-S. and J.-G. Dai, *X-ray computed tomography for pore-related characterization and simulation of cement mortar matrix*. NDT & E International, 2017. **86**: p. 28-35.
115. Cnudde, V. and M.N. Boone, *High-resolution X-ray computed tomography in geosciences: A review of the current technology and applications*. Earth-Science Reviews, 2013. **123**: p. 1-17.
116. Peng, S., et al., *Using X-ray computed tomography in pore structure characterization for a Berea sandstone: Resolution effect*. Journal of Hydrology, 2012. **472**: p. 254-261.

117. Steppe, K., et al., *Use of X-ray computed microtomography for non-invasive determination of wood anatomical characteristics*. Journal of structural biology, 2004. **148**(1): p. 11-21.
118. Taina, I., R. Heck, and T. Elliot, *Application of X-ray computed tomography to soil science: A literature review*. Canadian Journal of Soil Science, 2008. **88**(1): p. 1-19.
119. Gallé, C., *Effect of drying on cement-based materials pore structure as identified by mercury intrusion porosimetry: a comparative study between oven-, vacuum-, and freeze-drying*. Cement and Concrete Research, 2001. **31**(10): p. 1467-1477.
120. Dewanckele, J., et al., *4D imaging and quantification of pore structure modifications inside natural building stones by means of high resolution X-ray CT*. Science of The Total Environment, 2012. **416**: p. 436-448.
121. Noiriél, C., *Resolving time-dependent evolution of pore-scale structure, permeability and reactivity using X-ray microtomography*. Reviews in Mineralogy and Geochemistry, 2015. **80**(1): p. 247-285.
122. Wildenschild, D., et al., *Using X-ray computed tomography in hydrology: systems, resolutions, and limitations*. Journal of Hydrology, 2002. **267**(3-4): p. 285-297.
123. Sijbers, J. and A. Postnov, *Reduction of ring artefacts in high resolution micro-CT reconstructions*. Physics in Medicine & Biology, 2004. **49**(14): p. N247.
124. Mees, F., et al., *Applications of X-ray computed tomography in the geosciences*. Geological Society, London, Special Publications, 2003. **215**(1): p. 1-6.
125. Cnudde, V., et al., *Recent progress in X-ray CT as a geosciences tool*. Applied Geochemistry, 2006. **21**(5): p. 826-832.
126. Abell, A., K. Willis, and D. Lange, *Mercury intrusion porosimetry and image analysis of cement-based materials*. Journal of colloid and interface science, 1999. **211**(1): p. 39-44.
127. Wong, H., M. Head, and N. Buenfeld, *Pore segmentation of cement-based materials from backscattered electron images*. Cement and Concrete Research, 2006. **36**(6): p. 1083-1090.
128. Petrov, I. and E. Schlegel, *Application of automatic image analysis for the investigation of autoclaved aerated concrete structure*. Cement and concrete research, 1994. **24**(5): p. 830-840.
129. Ziel, R., A. Haus, and A. Tulke, *Quantification of the pore size distribution (porosity profiles) in microfiltration membranes by SEM, TEM and computer image analysis*. Journal of membrane science, 2008. **323**(2): p. 241-246.
130. Diamond, S. and M.E. Leeman, *Pore size distributions in hardened cement paste by SEM image analysis*. MRS Online Proceedings Library Archive, 1994. **370**.
131. Lange, D.A., H.M. Jennings, and S.P. Shah, *Image analysis techniques for characterization of pore structure of cement-based materials*. Cement and Concrete Research, 1994. **24**(5): p. 841-853.
132. Dathe, A., et al., *The surface fractal dimension of the soil-pore interface as measured by image analysis*. Geoderma, 2001. **103**(1-2): p. 203-229.
133. Berryman, J.G. and S.C. Blair, *Use of digital image analysis to estimate fluid permeability of porous materials: Application of two-point correlation functions*. Journal of applied Physics, 1986. **60**(6): p. 1930-1938.
134. Ruzyla, K., *Characterization of pore space by quantitative image analysis*. SPE Formation Evaluation, 1986. **1**(04): p. 389-398.
135. Scrivener, K.L., *Backscattered electron imaging of cementitious microstructures: understanding and quantification*. Cement and Concrete Composites, 2004. **26**(8): p. 935-945.
136. Kurumisawa, K. and K. Tanaka, *Three-dimensional visualization of pore structure in hardened cement paste by the gallium intrusion technique*. Cement and Concrete Research, 2006. **36**(2): p. 330-336.
137. Remondino, F. and S. El-Hakim, *Image-based 3D modelling: a review*. The photogrammetric record, 2006. **21**(115): p. 269-291.
138. Markelj, P., et al., *A review of 3D/2D registration methods for image-guided interventions*. Medical image analysis, 2012. **16**(3): p. 642-661.
139. Kaufmann, J., *Pore space analysis of cement-based materials by combined Nitrogen sorption – Wood's metal impregnation and multi-cycle mercury intrusion*. Cement and Concrete Composites, 2010. **32**(7): p. 514-522.
140. Münch, B. and L. Holzer, *Contradicting geometrical concepts in pore size analysis attained with electron microscopy and mercury intrusion*. Journal of the American Ceramic Society, 2008. **91**(12): p. 4059-4067.
141. Yot, P.G., et al., *Mechanical energy storage performance of an aluminum fumarate metal-organic framework*. Chemical science, 2016. **7**(1): p. 446-450.
142. Chen, Y., et al., *The effect of analytical particle size on gas adsorption porosimetry of shale*. International Journal of Coal Geology, 2015. **138**: p. 103-112.
143. Maciá-Agulló, J.A., et al., *Activation of coal tar pitch carbon fibres: Physical activation vs. chemical activation*. Carbon, 2004. **42**(7): p. 1367-1370.
144. Young, P., et al., *An efficient approach to converting three-dimensional image data into highly accurate computational models*. Philosophical Transactions of the Royal Society of London A: Mathematical, Physical and Engineering Sciences, 2008. **366**(1878): p. 3155-3173.
145. Kerckhofs, G., et al., *Validation of x-ray microfocus computed tomography as an imaging tool for porous structures*. Review of Scientific Instruments, 2008. **79**(1): p. 013711.

146. Hu, J. and P. Stroeven. *Proper characterisation of pore size distribution in cementitious materials*. in *Key Engineering Materials*. 2006. Trans Tech Publ.
147. Westermarck, S., et al., *Mercury porosimetry of pharmaceutical powders and granules*. Journal of Porous Materials, 1998. **5**(1): p. 77-86.
148. Weitkamp, J., K.S.W. Sing, and F. Schüth, *Handbook of porous solids*. 2002: Wiley-Vch.
149. BENTUR, A., *The pore structure of hydrated cementitious compounds of different chemical composition*. Journal of the American Ceramic Society, 1980. **63**(7-8): p. 381-386.
150. Midgley, H. and J. Illston, *Some comments on the microstructure of hardened cement pastes*. Cement and Concrete Research, 1983. **13**(2): p. 197-206.
151. Beaudoin, J.J., *Porosity measurement of some hydrated cementitious systems by high pressure mercury intrusion-microstructural limitations*. Cement and Concrete Research, 1979. **9**(6): p. 771-781.
152. Sing, K.S., *Characterization of porous materials: past, present and future*. Colloids and Surfaces A: Physicochemical and Engineering Aspects, 2004. **241**(1-3): p. 3-7.
153. Good, R.J., *The Contact Angle of Mercury on the Internal Surfaces of Porous Bodies A Footnote to DN Winslow's Review of Porosimetry*, in *Surface and Colloid Science*. 1984, Springer. p. 283-287.
154. Cultrone, G. and E. Sebastián, *Laboratory simulation showing the influence of salt efflorescence on the weathering of composite building materials*. Environmental geology, 2008. **56**(3-4): p. 729-740.
155. Nagy, V. and L.M. Vas, *Pore characteristic determination with mercury porosimetry in polyester staple yarns*. Fibres and Textiles in Eastern Europe, 2005. **13**(3): p. 21.
156. Volfkovich, Y.M. and V. Bagotzky, *The method of standard porosimetry: 1. Principles and possibilities*. Journal of power sources, 1994. **48**(3): p. 327-338.
157. Klobes, P., et al., *Rock porosity determination by combination of X-ray computerized tomography with mercury porosimetry*. Fresenius' journal of analytical chemistry, 1997. **357**(5): p. 543-547.
158. Klobes, P., et al., *Investigation of rock samples using X-ray-microcomputer-tomography before and after mercury intrusion porosimetry*. MRS Online Proceedings Library Archive, 1996. **465**.
159. Lubda, D., et al., *Comprehensive pore structure characterization of silica monoliths with controlled mesopore size and macropore size by nitrogen sorption, mercury porosimetry, transmission electron microscopy and inverse size exclusion chromatography*. Journal of Chromatography A, 2005. **1083**(1-2): p. 14-22.
160. Parrott, L., *Measurement and modeling of porosity in drying cement paste*. MRS Online Proceedings Library Archive, 1986. **85**.
161. Patel, R., et al., *Influence of curing at different relative humidities upon compound reactions and porosity in Portland cement paste*. Materials and Structures, 1988. **21**(3): p. 192-197.
162. Kärger, J., D.M. Ruthven, and D.N. Theodorou, *Diffusion in nanoporous materials*. 2012: John Wiley & Sons.
163. Bhatia, S.K. and D. Nicholson, *Hydrodynamic origin of diffusion in nanopores*. Physical review letters, 2003. **90**(1): p. 016105.
164. Wark, D.A., et al., *Reassessment of pore shapes in microstructurally equilibrated rocks, with implications for permeability of the upper mantle*. Journal of Geophysical Research: Solid Earth, 2003. **108**(B1).
165. Patzek, T. and D. Silin, *Shape factor and hydraulic conductance in noncircular capillaries: I. One-phase creeping flow*. Journal of colloid and interface science, 2001. **236**(2): p. 295-304.
166. Sisavath, S., X. Jing, and R.W. Zimmerman, *Laminar flow through irregularly-shaped pores in sedimentary rocks*. Transport in Porous Media, 2001. **45**(1): p. 41-62.
167. Ilavsky, J., C. Berndt, and J. Karthikeyan, *Mercury intrusion porosimetry of plasma-sprayed ceramic*. Journal of materials science, 1997. **32**(15): p. 3925-3932.
168. Khan, M., *Factors affecting the thermal properties of concrete and applicability of its prediction models*. Building and Environment, 2002. **37**(6): p. 607-614.
169. Pagliai, M. and N. Vignozzi, *The soil pore system as an indicator of soil quality*. Advances in GeoEcology, 2002. **35**: p. 69-80.
170. Lim, S., H.-S. Lee, and S. Kawashima, *Pore structure refinement of cement paste incorporating nanosilica: Study with dual beam scanning electron microscopy/focused ion beam (SEM/FIB)*. Materials Characterization, 2018. **145**: p. 323-328.
171. Geremew, A.M. and E.K. Yanful, *Dynamic properties and influence of clay mineralogy types on the cyclic strength of mine tailings*. International Journal of Geomechanics, 2012. **13**(4): p. 441-453.
172. MatWeb, L., *Bi50-Pb26.7-Sn13.3-Cd10 Bismuth-Lead-Tin-Cadmium Fusible Alloy*, M.m.p. database, Editor. 2015.
173. Johannes, W., et al., *An interlaboratory comparison of piston-cylinder pressure calibration using the albite-breakdown reaction*. Contributions to Mineralogy and Petrology, 1971. **32**(1): p. 24-38.
174. Construction, P.s.R.o.C.M.o., *GB/T50123-1999 soil test method*. Beijing: China Planning Press., 1999.
175. Jang, D.-J., J.D. Frost, and J.-Y. Park, *Preparation of epoxy impregnated sand coupons for image analysis*. 1999.
176. Zhao, H. and D. Darwin, *Quantitative backscattered electron analysis of cement paste*. Cement and concrete research, 1992. **22**(4): p. 695-706.
177. Ridler, T. and S. Calvard, *Picture thresholding using an iterative selection method*. IEEE trans syst Man Cybern, 1978. **8**(8): p. 630-632.

178. Roschger, P., et al., *Validation of quantitative backscattered electron imaging for the measurement of mineral density distribution in human bone biopsies*. Bone, 1998. **23**(4): p. 319-326.
179. Shimizu, R. and K. Murata, *Monte Carlo Calculations of the Electron-Sample Interactions in the Scanning Electron Microscope*. Journal of Applied Physics, 1971. **42**(1): p. 387-394.
180. Sezgin, M. and B. Sankur, *Survey over image thresholding techniques and quantitative performance evaluation*. Journal of Electronic imaging, 2004. **13**(1): p. 146-166.
181. Jang, D.-J., J.D. Frost, and J.-Y. Park, *Preparation of epoxy impregnated sand coupons for image analysis*. Geotechnical Testing Journal, 1999. **22**(2): p. 153-164.
182. Scrivener, K.L., et al., *Analysis of phases in cement paste using backscattered electron images, methanol adsorption and thermogravimetric analysis*. MRS Online Proceedings Library Archive, 1986. **85**.
183. Amari, S.-i. and H. Nagaoka, *Methods of information geometry*. Vol. 191. 2007: American Mathematical Soc.
184. Sridharan, A., A. Altschaeffl, and S. Diamond, *Pore size distribution studies*. Journal of the soil mechanics and foundations division, 1971. **97**(5): p. 771-787.
185. Lawrence, G., *Stability of soil pores during mercury intrusion porosimetry*. Journal of Soil Science, 1978. **29**(3): p. 299-304.
186. Sills, I., L. Aylmore, and J. Quirk, *A Comparison Between Mercury Injection and Nitrogen Sorption as Methods of Determining Pore Size Distributions I*. Soil Science Society of America Journal, 1973. **37**(4): p. 535-537.
187. Vogel, H. and A. Kretschmar, *Topological characterization of pore space in soil—Sample preparation and digital image-processing*. Geoderma, 1996. **73**(1-2): p. 23-38.
188. Fiès, J. and A. Bruand, *Textural porosity analysis of a silty clay soil using pore volume balance estimation, mercury porosimetry and quantified backscattered electron scanning image (BESI)*. Geoderma, 1990. **47**(3-4): p. 209-219.
189. Haynes, J., *Pore size analysis according to the Kelvin equation*. Matériaux et Construction, 1973. **6**(3): p. 209-213.
190. Nimmo, J.R., *Porosity and pore size distribution*. Encyclopedia of Soils in the Environment, 2004. **3**: p. 295-303.
191. Griffiths, F. and R. Joshi, *Change in pore size distribution due to consolidation of clays*. Technical note. Geotechnique, 1989. **39**(1).
192. Frías, M. and J. Cabrera, *Pore size distribution and degree of hydration of metakaolin–cement pastes*. Cement and Concrete Research, 2000. **30**(4): p. 561-569.
193. Promentilla, M.A.B., et al., *Quantification of tortuosity in hardened cement pastes using synchrotron-based X-ray computed microtomography*. Cement and Concrete Research, 2009. **39**(6): p. 548-557.
194. Zhang, M., G. Ye, and K. Van Breugel, *Microstructure-based modeling of water diffusivity in cement paste*. Construction and Building Materials, 2011. **25**(4): p. 2046-2052.
195. Collins, F. and J. Sanjayan, *Prediction of capillary transport of alkali activated slag cementitious binders under unsaturated conditions by elliptical pore shape modeling*. Journal of Porous Materials, 2010. **17**(4): p. 435-442.
196. Wang, H. and Q. Li, *Prediction of elastic modulus and Poisson's ratio for unsaturated concrete*. International Journal of Solids and Structures, 2007. **44**(5): p. 1370-1379.
197. Rößler, M. and I. Odler, *Investigations on the relationship between porosity, structure and strength of hydrated portland cement pastes I. Effect of porosity*. Cement and Concrete Research, 1985. **15**(2): p. 320-330.
198. Luping, T., *A study of the quantitative relationship between strength and pore-size distribution of porous materials*. Cement and concrete research, 1986. **16**(1): p. 87-96.
199. Dormieux, L. and F.-J. Ulm, *Applied micromechanics of porous materials*. Vol. 480. 2007: Springer Science & Business Media.
200. Segurado, J. and J. Llorca, *Computational micromechanics of composites: the effect of particle spatial distribution*. Mechanics of materials, 2006. **38**(8-10): p. 873-883.
201. Walcarius, A., *Mesoporous materials and electrochemistry*. Chemical Society Reviews, 2013. **42**(9): p. 4098-4140.
202. Hollister, S.J., *Porous scaffold design for tissue engineering*. Nature materials, 2005. **4**(7): p. 518.
203. Wan, Y. and D. Zhao, *On the controllable soft-templating approach to mesoporous silicates*. Chemical reviews, 2007. **107**(7): p. 2821-2860.
204. Lee, J., J. Kim, and T. Hyeon, *Recent progress in the synthesis of porous carbon materials*. Advanced Materials, 2006. **18**(16): p. 2073-2094.
205. Deng, X., et al., *Effect of Pore Clustering on the Mechanical Behavior of Powder Metallurgy (P/M) Steels*. P/M Science & Technology Briefs, 2004. **6**(2): p. 5-9.
206. Arns, J.-Y., et al., *Relative permeability from tomographic images; effect of correlated heterogeneity*. Journal of Petroleum Science and Engineering, 2003. **39**(3-4): p. 247-259.
207. Sevostianov, I. and V. Kushch, *Effect of pore distribution on the statistics of peak stress and overall properties of porous material*. International Journal of Solids and Structures, 2009. **46**(25-26): p. 4419-4429.
208. Chan, K.S., *Roles of microstructure in fatigue crack initiation*. International Journal of Fatigue, 2010. **32**(9): p. 1428-1447.

209. Li, H., et al., *Microstructure of cement mortar with nano-particles*. Composites Part B: Engineering, 2004. **35**(2): p. 185-189.
210. Sobolev, K., et al., *Engineering of SiO₂ nanoparticles for optimal performance in nano cement-based materials*, in *Nanotechnology in construction 3*. 2009, Springer. p. 139-148.
211. Chuah, S., et al., *Nano reinforced cement and concrete composites and new perspective from graphene oxide*. Construction and Building Materials, 2014. **73**: p. 113-124.
212. Gao, W., *The chemistry of graphene oxide*, in *Graphene oxide*. 2015, Springer. p. 61-95.
213. Dikin, D.A., et al., *Preparation and characterization of graphene oxide paper*. Nature, 2007. **448**(7152): p. 457.
214. Mohammed, A., et al., *Incorporating graphene oxide in cement composites: A study of transport properties*. Construction and Building Materials, 2015. **84**: p. 341-347.
215. Pan, Z., et al., *Mechanical properties and microstructure of a graphene oxide–cement composite*. Cement and Concrete Composites, 2015. **58**: p. 140-147.
216. Wang, Q., et al., *Influence of graphene oxide additions on the microstructure and mechanical strength of cement*. New Carbon Materials, 2015. **30**(4): p. 349-356.
217. Gong, K., et al., *Reinforcing effects of graphene oxide on portland cement paste*. Journal of Materials in Civil Engineering, 2014. **27**(2): p. A4014010.
218. Li, X., et al., *Effects of graphene oxide agglomerates on workability, hydration, microstructure and compressive strength of cement paste*. Construction and Building Materials, 2017. **145**: p. 402-410.
219. Collins, F., J. Lambert, and W.H. Duan, *The influences of admixtures on the dispersion, workability, and strength of carbon nanotube–OPC paste mixtures*. Cement and Concrete Composites, 2012. **34**(2): p. 201-207.
220. Hannesson, G., et al., *The influence of high volume of fly ash and slag on the compressive strength of self-consolidating concrete*. Construction and Building Materials, 2012. **30**: p. 161-168.
221. Soper, A., *The radial distribution functions of water and ice from 220 to 673 K and at pressures up to 400 MPa*. Chemical Physics, 2000. **258**(2-3): p. 121-137.
222. von Lilienfeld, O.A., et al., *Fourier series of atomic radial distribution functions: A molecular fingerprint for machine learning models of quantum chemical properties*. International Journal of Quantum Chemistry, 2015. **115**(16): p. 1084-1093.
223. Bell, R., *Pair distribution function for particles in a box*. Nature, 1968. **218**(5145): p. 985.
224. Igarashi, S.-i., A. Watanabe, and M. Kawamura, *Evaluation of capillary pore size characteristics in high-strength concrete at early ages*. Cement and Concrete Research, 2005. **35**(3): p. 513-519.
225. Perelson, A.S., *Spatial distribution of surface immunoglobulin on B lymphocytes: Local ordering*. Experimental cell research, 1978. **112**(2): p. 309-321.
226. Renau-Piqueras, J., et al., *Chronic Ethanol Consumption Affects Filipin-Cholesterol Complexes and Intramembranous Particles of Synaptosomes of Rat Brain Cortex*. Alcoholism: Clinical and Experimental Research, 1987. **11**(5): p. 486-493.
227. Baumann, G., et al., *Non-random spatial distribution of intermembrane particles in red blood cell membrane*. Pathology-Research and Practice, 1990. **186**(1): p. 159-166.
228. Younge, K., et al., *The use of radial distribution and pair-correlation functions to analyze and describe biological aggregations*. Limnology and Oceanography: Methods, 2006. **4**(10): p. 382-391.
229. Olszówka-Myalska, A., J. Szala, and J. Cwajna, *Characterization of reinforcement distribution in Al/(Al₂O₃)_p composites obtained from composite powder*. Materials characterization, 2001. **46**(2-3): p. 189-195.
230. Karnezis, P., G. Durrant, and B. Cantor, *Characterization of reinforcement distribution in cast Al-alloy/SiC_p composites*. Materials Characterization, 1998. **40**(2): p. 97-109.
231. Segurado, J., C. Gonzalez, and J. Llorca, *A numerical investigation of the effect of particle clustering on the mechanical properties of composites*. Acta materialia, 2003. **51**(8): p. 2355-2369.
232. Yu, M., P. Zhu, and Y. Ma, *Effects of particle clustering on the tensile properties and failure mechanisms of hollow spheres filled syntactic foams: A numerical investigation by microstructure based modeling*. Materials & Design, 2013. **47**: p. 80-89.
233. Matteoli, E. and G.A. Mansoori, *A simple expression for radial distribution functions of pure fluids and mixtures*. The Journal of chemical physics, 1995. **103**(11): p. 4672-4677.
234. Wolberg, J., *Data analysis using the method of least squares: extracting the most information from experiments*. 2006: Springer Science & Business Media.
235. Lopes, R.H., *Kolmogorov-smirnov test*, in *International encyclopedia of statistical science*. 2011, Springer. p. 718-720.
236. Massey Jr, F.J., *The Kolmogorov-Smirnov test for goodness of fit*. Journal of the American statistical Association, 1951. **46**(253): p. 68-78.
237. Luong, D.D., et al., *Development of high performance lightweight aluminum alloy/SiC hollow sphere syntactic foams and compressive characterization at quasi-static and high strain rates*. Journal of Alloys and Compounds, 2013. **550**: p. 412-422.
238. LU, Z., et al., *Mechanical properties of polyurethane foams filled by micro-spheres [J]*. Acta Materiae Compositae Sinica, 2008. **6**: p. 034.

239. Kruk, M., et al., *Determination and tailoring the pore entrance size in ordered silicas with cage-like mesoporous structures*. Journal of the American Chemical Society, 2002. **124**(5): p. 768-769.
240. Stachowiak, A.N., et al., *Bioactive hydrogels with an ordered cellular structure combine interconnected macroporosity and robust mechanical properties*. Advanced Materials, 2005. **17**(4): p. 399-403.
241. Zhang, H., et al., *Uniform emulsion-templated silica beads with high pore volume and hierarchical porosity*. Advanced Materials, 2003. **15**(1): p. 78-81.
242. Montavon, G., et al., *Machine learning of molecular electronic properties in chemical compound space*. New Journal of Physics, 2013. **15**(9): p. 095003.
243. Zhang, S.-W., et al., *Classification of protein quaternary structure with support vector machine*. Bioinformatics, 2003. **19**(18): p. 2390-2396.
244. Ulm, F.-J., G. Constantinides, and F.H. Heukamp, *Is concrete a poromechanics materials?—A multiscale investigation of poroelastic properties*. Materials and structures, 2004. **37**(1): p. 43-58.
245. Guéguen, Y., L. Dormieux, and M. Boutéca, *Fundamentals of poromechanics*. Mechanics of Fluid-Saturated Porous Materials (International Geophysics Series, Vol. 89), Y. Guéguen and M. Boutéca, eds., Elsevier Academic Press, Burlington, MA, 2004.
246. Chou, J.-S., et al., *Machine learning in concrete strength simulations: Multi-nation data analytics*. Construction and Building Materials, 2014. **73**: p. 771-780.
247. Bal'shin, M.Y. *Variation of the mechanical properties of P/M metals with porosity and limiting properties of porous sintered materials*. in Dokl. Akad. Nauk SSSR. 1949.
248. Ryshkewitch, E., *Compression strength of porous sintered alumina and zirconia: 9th communication to ceramography*. Journal of the American Ceramic Society, 1953. **36**(2): p. 65-68.
249. Taylor, H.F., *Cement chemistry*. 1997: Thomas Telford.
250. Fernandez, M., N.R. Trefiak, and T.K. Woo, *Atomic property weighted radial distribution functions descriptors of metal–organic frameworks for the prediction of gas uptake capacity*. The Journal of Physical Chemistry C, 2013. **117**(27): p. 14095-14105.
251. Fernandez, M., H. Shi, and A.S. Barnard, *Quantitative Structure–Property Relationship Modeling of Electronic Properties of Graphene Using Atomic Radial Distribution Function Scores*. Journal of chemical information and modeling, 2015. **55**(12): p. 2500-2506.
252. Huynh, T.-P., C.-L. Hwang, and A.H. Limongan, *The long-term creep and shrinkage behaviors of green concrete designed for bridge girder using a densified mixture design algorithm*. Cement and Concrete Composites, 2018. **87**: p. 79-88.
253. Georgiades, A., C. Ftikos, and J. Marinos, *Effect of micropore structure on autoclaved aerated concrete shrinkage*. Cement and concrete research, 1991. **21**(4): p. 655-662.
254. Boivin, P., P. Garnier, and D. Tessier, *Relationship between clay content, clay type, and shrinkage properties of soil samples*. Soil Science Society of America Journal, 2004. **68**(4): p. 1145-1153.
255. ZHANG, X.-w., W. Chang-ming, and L. Jun-xia, *Variation characteristics of soft clay micro-pore in the creep condition*. Rock and Soil Mechanics, 2010. **31**(4): p. 1061-1067.
256. Bazant, Z.P. and J. Chern, *Concrete creep at variable humidity: constitutive law and mechanism*. Materials and structures, 1985. **18**(1): p. 1.
257. Li, W., et al., *Effects of Nanoalumina and Graphene Oxide on Early-Age Hydration and Mechanical Properties of Cement Paste*. Journal of Materials in Civil Engineering, 2017. **29**(9): p. 04017087.
258. Gao, F., G. Beyer, and Q. Yuan, *A mechanistic study of fire retardancy of carbon nanotube/ethylene vinyl acetate copolymers and their clay composites*. Polymer Degradation and Stability, 2005. **89**(3): p. 559-564.
259. Saito, R., G. Dresselhaus, and M.S. Dresselhaus, *Physical properties of carbon nanotubes*. 1998: World Scientific.
260. Elias, L., et al., *Immiscible polymer blends stabilized with nano-silica particles: Rheology and effective interfacial tension*. Polymer, 2008. **49**(20): p. 4378-4385.
261. Zhang, R., et al., *Impacts of nanopore structure and elastic properties on stress-dependent permeability of gas shales*. Journal of Natural Gas Science and Engineering, 2015. **26**: p. 1663-1672.
262. Hu, Q., et al., *Characterization of micro-nano pore networks in shale oil reservoirs of Paleogene Shahejie Formation in Dongying Sag of Bohai Bay Basin, East China*. Petroleum Exploration and Development, 2017. **44**(5): p. 720-730.
263. Clarkson, C.R., et al., *Nanopore-structure analysis and permeability predictions for a tight gas siltstone reservoir by use of low-pressure adsorption and mercury-intrusion techniques*. SPE Reservoir Evaluation & Engineering, 2012. **15**(06): p. 648-661.
264. Winslow, D.N., *The validity of high pressure mercury intrusion porosimetry*. Journal of Colloid and Interface Science, 1978. **67**(1): p. 42-47.
265. Bergins, C., et al., *Mechanical/thermal dewatering of lignite. Part 3: Physical properties and pore structure of MTE product coals*. Fuel, 2007. **86**(1): p. 3-16.
266. Roque-Malherbe, R.M., *Adsorption and diffusion in nanoporous materials*. 2018: CRC press.
267. Dubbeldam, D. and R.Q. Snurr, *Recent developments in the molecular modeling of diffusion in nanoporous materials*. Molecular Simulation, 2007. **33**(4-5): p. 305-325.
268. Washburn, E.W., *The dynamics of capillary flow*. Physical review, 1921. **17**(3): p. 273.

269. Dullien, F.A.L., *Wood's metal porosimetry and its relation to mercury porosimetry*. Powder technology, 1981. **29**(1): p. 109-116.
270. Chen, S.J., et al., *A new scheme for analysis of pore characteristics using centrifuge driven non-toxic metal intrusion*. Geomechanics and Geophysics for Geo-Energy and Geo-Resources, 2016. **2**(3): p. 173-182.
271. Mayo, S.L., B.D. Olafson, and W.A. Goddard, *DREIDING: a generic force field for molecular simulations*. Journal of Physical chemistry, 1990. **94**(26): p. 8897-8909.
272. Girifalco, L.A. and V.G. Weizer, *Application of the Morse potential function to cubic metals*. Physical Review, 1959. **114**(3): p. 687.
273. Delley, B., *From molecules to solids with the DMol 3 approach*. The Journal of chemical physics, 2000. **113**(18): p. 7756-7764.
274. Ernzerhof, M. and G.E. Scuseria, *Assessment of the Perdew–Burke–Ernzerhof exchange–correlation functional*. The Journal of chemical physics, 1999. **110**(11): p. 5029-5036.
275. Inada, Y. and H. Orita, *Efficiency of numerical basis sets for predicting the binding energies of hydrogen bonded complexes: evidence of small basis set superposition error compared to Gaussian basis sets*. Journal of computational chemistry, 2008. **29**(2): p. 225-232.
276. Schulz, M.J., A.D. Kelkar, and M.J. Sundaresan, *Nanoengineering of structural, functional and smart materials*. 2005: CRC Press.
277. Module, F., *Material Studio 6.0*. Accelrys Inc., San Diego, CA, 2011.
278. Awasthi, A., Y. Bhatt, and S. Garg, *Measurement of contact angle in systems involving liquid metals*. Measurement Science and Technology, 1996. **7**(5): p. 753.
279. Kemball, C., *On the surface tension of mercury*. Transactions of the Faraday Society, 1946. **42**: p. 526-537.
280. Kutana, A. and K. Giapis, *Contact angles, ordering, and solidification of liquid mercury in carbon nanotube cavities*. Physical Review B, 2007. **76**(19): p. 195444.
281. Klement Jr, W., A. Jayaraman, and G. Kennedy, *Transformations in mercury at high pressures*. Physical Review, 1963. **131**(1): p. 1.
282. Thompson, A.W. and M.I. Baskes, *The influence of grain size on the work hardening of face-center cubic polycrystals*. Philosophical magazine, 1973. **28**(2): p. 301-308.
283. Adler, D., *Mechanisms for metal-nonmetal transitions in transition-metal oxides and sulfides*. Reviews of Modern Physics, 1968. **40**(4): p. 714.
284. Jung, J., *A note on the influence of hydrostatic pressure on dislocations*. Philosophical Magazine A, 1981. **43**(4): p. 1057-1061.
285. Davis, L.A. and R.B. Gordon, *Compression of mercury at high pressure*. The journal of chemical physics, 1967. **46**(7): p. 2650-2660.
286. Joos, B. and M. Duesbery, *The Peierls stress of dislocations: an analytic formula*. Physical Review Letters, 1997. **78**(2): p. 266.